GEOCHEMISTRY OF THE BAIE CHARRIER BASALTIC SECTION, COURBET PENINSULA, KERGUELEN ARCHIPELAGO: IMPLICATIONS FOR THE COMPOSITION OF THE KERGUELEN MANTLE PLUME

By

DIANE W. HANANO

A THESIS SUBMITTED IN PARTIAL FUFILLMENT OF

THE REQUIREMENTS FOR THE DEGREE OF

BACHELOR OF SCIENCE (HONOURS)

In

THE FACULTY OF SCIENCE
Department of Earth and Ocean Sciences

This thesis conforms to the required standard

……..……. ……..……

Supervisor Supervisor

THE UNIVERSITY OF BRITISH COLUMBIA

MARCH 2004

ABSTRACT

The Baie Charrier basaltic section is located on the northern Courbet Peninsula on the Kerguelen Archipelago. The archipelago represents the emergent part of the Northern Kerguelen Plateau, part of the Kerguelen large igneous province in the southern Indian Ocean. The archipelago formed through volcanism (40 Ma to recent) related to the Kerguelen mantle plume. This study presents a detailed petrographic and geochemical analysis of basalts from the Baie Charrier section. The results of this study will compliment the 1000 m Mt. Crozier section located in the center of the Courbet Peninsula. Mineral compositions of olivine and clinopyroxene phenocrysts by electron microprobe analysis were obtained for phenocryst zoning profiles and mineral-melt equilibria. Major and trace element concentrations by XRF and high-resolution ICP-MS, as well as Sr, Nd, and Pb isotopic compositions by TIMS and multi-collector ICP-MS define the chemical and isotopic characteristics of the Baie Charrier section.

Based on petrographic and geochemical criteria, the Baie Charrier section is subdivided into four distinct units. The Baie Charrier basalts are primarily olivine-phyric, and sometimes contain phenocrysts of plagioclase or clinopyroxene. Mineral chemistry reveals normally zoned phenocrysts, with olivine core compositions ranging from $Fo_{86\text{-}70}$ and clinopyroxene core Mg# ranging from 0.88 to 0.79. The Baie Charrier basalts are mildly alkalic and possess relatively high MgO contents; Units A and C are comprised of high-MgO (8-10 wt.%) basalts, and sample 240 of unit D is a picrite (>16 wt.%). CaO depletion at ~6 wt.% MgO, coupled with a continuously increasing Al_2O_3 content, reflect fractionation driven by significant clinopyroxene crystallization. Trace element depletion in Ni, Cr, and Sc with decreasing MgO reflect the relative compatibility of these elements in olivine and clinopyroxene phenocrysts. Incompatible element abundance relationships are used to define a relative incompatibility index in order of increasing compatibility: Th<Ce, Nb, Rb<Ba<Zr<Sr. The Baie Charrier basalts are enriched in highly incompatible elements and light rare earth elements. The units of the Baie Charrier section are also isotopically distinct; Unit C possesses some of the highest $^{143}Nd/^{144}Nd$, lowest $^{87}Sr/^{86}Sr$, and lowest Pb isotopic ratios, while Unit D has the highest Pb isotopic ratios of the section.

The small-scale petrographic and geochemical variation observed in the Baie Charrier section is interpreted to reflect temporal changes in volcanism derived from a heterogeneous source region. Mineral-melt equilibria constrain the maximum MgO content for magmas without accumulated phenocrysts to be between 8-10 wt.% MgO. The similarities between the trace element and isotopic compositions of the Baie Charrier section and the Mt. Crozier section suggests that both are derived from the same source, which supports the interpretation of the Courbet Peninsula as a single volcanic unit. However, the abundance of olivine-phyric basalts at Baie Charrier, and their absence at Mt. Crozier, suggest that the eruptive center of this volcano may not coincide with the present geographic center of the Courbet Peninsula. Lastly, the Baie Charrier basalts, with their highly radiogenic Pb compositions, contain a strong signature of an enriched plume-derived component, and provide additional constraints on the source composition of the Kerguelen mantle plume.

TABLE OF CONTENTS

LIST OF FIGURES

LIST OF TABLES

ACKNOWLEDGEMENTS

First and foremost, I must thank my thesis supervisors James Scoates and Dominique Weis for giving me the opportunity to work on this project. Their advice, support and encouragement during the past year have been greatly appreciated. I am grateful for all of their time and effort spent editing this paper, looking at my data and graphs, and answering my questions.

I would like to thank Bruno Kieffer for his assistance with sample leaching, digestion and column chemistry procedures, as well as Sr and Nd analysis by TIMS. Many thanks to Wilma Pretorius for her assistance with sample digestion and dilution procedures, as well as trace element analysis by HR-ICP-MS. I must also thank Jane Barling for her assistance with Pb analysis by MC-ICP-MS. I would also like to thank Heidi Annell and Mati Rausdepp for their help with electron microprobe analysis, and Christa Sluggett and Richard Friedman for general lab assistance.

A portion of this research was funded by an NSERC Undergraduate Student Research Award. As well, I would like to thank Dimitri Damasceno at the Université Libre de Bruxelles for whole rock sample preparation and Mike Rhodes at the University of Massachusetts for major and trace element XRF data.

I must acknowledge my fellow P.O.T.'s Gwen Williams, Melissa Zack, Elizabeth Castle, and Julia Davison for their company, moral support, and reviews of this paper. Lastly, thank-you to my family, friends, and especially Ryan for their unconditional love, support and patience.

1.1 Geochemistry of Basalts

Geochemistry is an extremely useful tool for studying the Earth, as it can be used to describe and interpret the chemical information recorded in rocks and minerals. The chemical composition of a given rock varies greatly depending on its source region and history, and is controlled by the behaviour of elements with different chemical properties. For example, highly incompatible elements such as the large ion lithophiles, which have large ionic radii and/or high charges, are not readily incorporated into crystal structures. During partial melting of the mantle, these elements become concentrated in the residual melt, resulting in chemical fractionation. Consequently, the source and the magma will have different chemical compositions. Rocks formed by such processes will have distinctive geochemical characteristics that can be used to reveal critical information regarding its source and history. For example, rocks formed by mid-ocean ridge, oceanic island, or island arc volcanism possess distinctive geochemical signatures that can be revealed through geochemical analyses. By contrast, radiogenic isotopes (e.g. Pb, Sr, Nd, Hf) are not fractionated by processes such as partial melting or crystallization. As a result, the isotopic composition of the magma is equivalent to the isotopic composition of the source. Therefore, isotope geochemistry of mantle-derived rocks such as basalts can provide insight into the chemistry of their source regions, as well as into the role of the various components involved in their genesis.

The study of compositional variability in the mantle must rely on rocks brought up from the interior of the earth, such as mantle xenoliths, or on rocks that have crystallized from melts originating deep in the mantle. Flood basalts and ocean island basalts (OIB) that comprise large igneous provinces are thought to have sources deep in

the mantle (e.g. Griffiths & Campbell, 1990; Coffin & Edholm, 1994). Thus, large igneous provinces are of great interest from a geochemical perspective.

1.2 Large Igneous Provinces and Mantle Plumes

Large igneous provinces (LIPs) are areas of emplacement of massive volumes of mafic magma, which are considered to have been brought to the surface by mantle plumes. Mantle plumes are columns of hot material that rise buoyantly through the mantle towards the surface of the earth (Griffiths & Campbell, 1990). There has been considerable debate regarding the origin of these plumes. The lower mantle, the upper mantle, and the core-mantle boundary are locations that have been proposed (e.g. Shen *et al*., 1998; Helmberger *et al*., 1998; Ritsema *et al*., 1999). However, it is now generally accepted that mantle plumes originate from deep in the mantle. Evidence includes the high $^{3}He/^{4}He$ ratios in OIB, suggesting that these plumes are tapping parts of the mantle that have never been degassed (Kurz *et al*., 1982). As well, OIB are enriched in incompatible elements relative to the primitive mantle, while mid-ocean ridge basalts (MORB) are depleted in these elements (Hofmann, 1997). MORB are derived from partial melting of the upper mantle, which becomes progressively depleted in these elements upon repeated melting to form the continental crust. Therefore OIB, with their 'enriched' character, must come from below this 'depleted' upper mantle region. Lastly, the estimated volumes of source material required to produce some LIPs, such as Kerguelen or Ontong-Java, extend well into the lower mantle (Coffin & Edholm, 1994). Thus, mantle plume-derived rocks have the ability to provide information about their source region, the lower mantle. Study of these rocks may also provide additional insight into the origins and dynamics of mantle plumes (e.g. Albarede & van der Hilst, 1999).

1.3 Scope of the Study

This study involves a detailed investigation into the geochemistry of the Baie Charrier basaltic section located on the Kerguelen Archipelago, which is part of the Kerguelen large igneous province located in the southern Indian Ocean. The geochemical analyses presented include the mineral chemistry of olivine and clinopyroxene phenocrysts, and the major and trace element concentrations and isotopic compositions of whole rocks from the section. The variation observed in the petrographic and geochemical properties of the basaltic rocks from the Baie Charrier section are used to subdivide the section into four distinct units, which are interpreted to reflect temporal changes in volcanism. The scale over which this variability is observed will be discussed in terms of the implications for magmatic processes and source region heterogeneity.

Importantly, this study presents new petrographic and geochemical data from the northern flanks of the Courbet Peninsula of the Kerguelen Archipelago. Mt. Crozier, a 1000 m basaltic section in the middle of the peninsula has been sampled extensively for petrographic and geochemical analysis (Scoates *et al*., in preparation). The Mt. Crozier section has been interpreted as representative of the enriched component of the Kerguelen plume (e.g. Weis *et al*., 2002) on the basis of its isotopic characteristics; more specifically its very radiogenic Pb isotopic compositions. The Baie Charrier section will complement the findings at Mt. Crozier, and provide further insight into the geologic history of the Courbet Peninsula. In particular, this study will address the proposed theory that the Courbet Peninsula is a single volcanic unit (Nougier, 1970). Finally, the isotopic compositions of the Baie Charrier basalts presented in this study yield information about the isotopic composition of their plume source. This study therefore provides additional

constraints on the source composition of the Kerguelen mantle plume and the various components that generate its enriched features.

2.1 Geologic History of the Kerguelen Mantle Plume

The formation of the Kerguelen Plateau, in the southern Indian Ocean, has been attributed to hotspot volcanism from the Kerguelen mantle plume. Volcanic activity associated with this plume began approximately 130 million years ago, following the break-up of Gondwana, when seafloor spreading was initiated between India, Australia and Antarctica (Frey *et al*., 2000; Coffin *et al*., 2002). During this time, the plume produced ~2.5 x 10^7 km^3 of basaltic magma (Coffin *et al.*, 2002), creating the world's second largest oceanic plateau and significantly altering the physiographic character of the Indian Ocean (Fig. 2.1).

The Southern Kerguelen Plateau formed between ~120 and ~110 Ma, followed by the formation of the Central Kerguelen Plateau between ~105 and ~100 Ma and Broken Ridge at ~95 Ma (Duncan, 2002; Coffin *et al*., 2002). This initial pulse of voluminous magmatism is interpreted to represent the arrival of the plume head at the base of the Indian Ocean lithosphere (Frey *et al*., 2000). Subsequently, the plume was associated with a mid-ocean ridge, resulting in the formation of the Ninetyeast Ridge (Weis *et al*., 1991). At a length of over 5000 km, this ridge is the longest linear feature on Earth. The ages of the basalts that comprise the ridge progressively increase in age from 38 Ma in the south to 82 Ma in the north (Duncan, 1991). Thus, the ridge is inferred to represent the trace of the Kerguelen hotspot, created as the Indian Plate moved northwards over the plume stem (Weis *et al*., 1992). At ~40 Ma, the Southeast Indian Ridge began to migrate towards the northwest, presumably caused by relatively rapid motion between the Australian and Antarctic plates (Mutter & Cande, 1983). This event was followed by the formation of the Northern Kerguelen Plateau and Kerguelen Archipelago and the separation of Broken Ridge from the Central Kerguelen Plateau (Frey *et al*., 2000; Coffin

et al., 2002). Thus, the Kerguelen Archipelago initially formed in a ridge-centered setting and later adopted an intraplate setting on the relatively stationary Antarctic Plate, where it has remained.

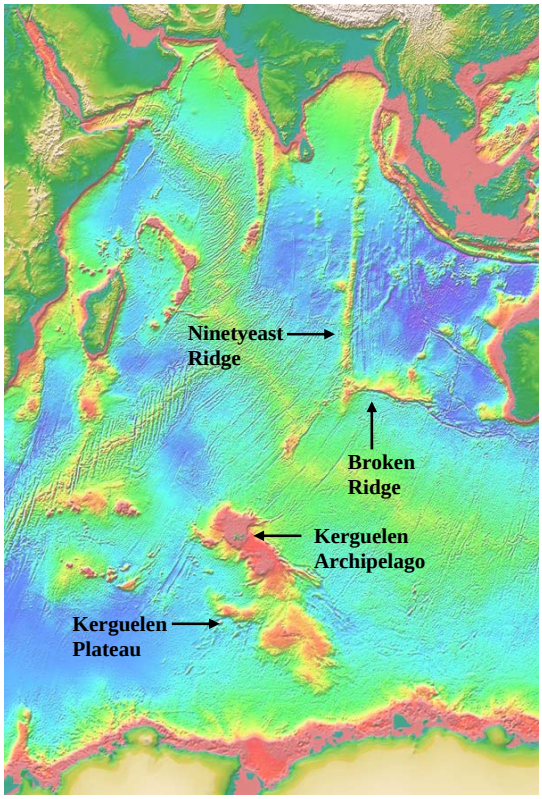

Fig. 2.1. Indian Ocean bathymetric map (Smith & Sandwell, 1997). Shown are features produced by volcanism from the Kerguelen mantle plume, including the Ninetyeast Ridge, Broken Ridge, Kerguelen Plateau, and Kerguelen Archipelago.

The recent volcanic history of the Kerguelen mantle plume has been varied and diffuse. There have been historic eruptions at Heard and McDonald Islands, located ~440 km southeast of the archipelago, and there is current volcanism at McDonald Island. However, Eocene and younger lavas have been found on both Heard Island and the Kerguelen Archipelago. This record of volcanism has raised considerable uncertainty over the current location of the hotspot. Plate reconstruction models have placed the hotspot to the west of the archipelago in order to match the Ninetyeast Ridge (Duncan &

Storey, 1992; Steinberger, 2000). However, drilling at ODP Site 1139 revealed the basalts to be 68 Ma (Duncan, 2002), thus ruling out this area as the location of the current hotspot. The record of recent volcanism, including 18-21 Ma seamounts between the Kerguelen Archipelago and Heard Island (Weis *et al*., 2002), suggests that the hotspot is located beneath Heard Island. A recent study involving paleomagnetics and numerical modelling has proposed that the Kerguelen hotspot has migrated southwards between 3º and 10º during the last 100 Myr (Antretter *et al*., 2002).

2.2 Geology of the Kerguelen Archipelago

The Kerguelen Archipelago is a 6500 km^2 assemblage of islands that represent the emergent part of the Northern Kerguelen Plateau (Fig. 2.2). Seismic studies have determined that the crust beneath the archipelago is 15-20 km thick, anomalously thicker than normal oceanic crust (Recq *et al*., 1994; Charvis *et al*., 1995). This crust does not possess any low-velocity zones, which result from the presence of continental material, suggesting that the crust underlying the archipelago is entirely oceanic (Recq *et al*., 1994; Charvis *et al*., 1995).

Over ~85% of the archipelago is covered by transitional-tholeiitic and mildly alkalic flood basalts (e.g. Nougier, 1970; Weis *et al*., 1993; Frey *et al*., 2000). These basalt flows are generally 1-5 m thick and dip gently to the southeast at an angle of 2-3º. The archipelago was heavily glaciated during the Quaternary, eroding 1-2 km of basalt and incising deep glacial valleys that now expose basaltic sequences up to 1000 m thick. The archipelago also contains isolated silicic and gabbroic plutonic complexes, ranging in age from 25 Ma to <1 Ma (Weis & Giret, 1994).

The basalts on the archipelago can be broadly divided into three groups based on their age and composition. The Loranchet Peninsula in the northwest and the Plateau Central are comprised of tholeiitic-transitional basalts with ages ranging from 26-29 Ma (Yang *et al*., 1998; Nicolaysen *et al*., 2000; Doucet *et al*., 2002; Frey *et al*., 2002). The Southeast Province is younger, with 25 Ma basalts of mildly alkalic composition (Weis *et al*., 1993; Frey *et al*., 2000). The basalts of the Courbet Peninsula are also mildly alkalic, but are slightly younger, with ages of 24 Ma (Nicolaysen *et al*., 2000). The transition to more alkaline volcanism is thought to reflect a decrease in partial melting and magma supply, possibly due to the anomalously thick lithosphere that underlies the archipelago (Weis *et al*., 1998; Frey *et al*., 2000; Damasceno *et al*., 2002).

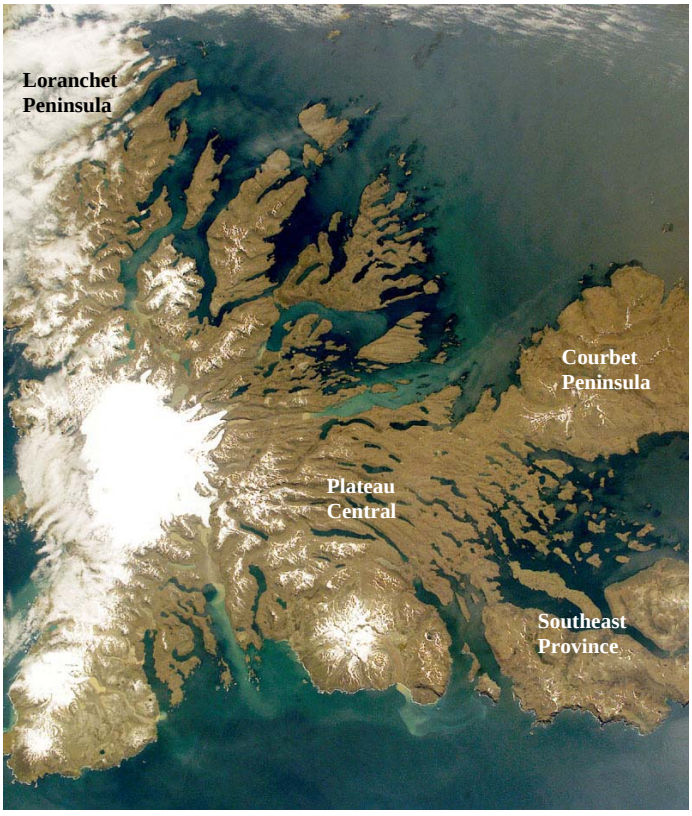

Fig. 2.2. Satellite photo of the Kerguelen Archipelago. Shown are the 26-29 Ma transitional-tholeiitic Loranchet Peninsula and Plateau Central to the west and the 24-25 Ma mildly alkalic Courbet Peninsula and the Southeast Province to the east.

2.3 Geology of the Courbet Peninsula

The Courbet Peninsula is located in the northeast part of the Kerguelen Archipelago (Fig. 2.2). The peninsula comprises approximately 1/5 of the overall area of the archipelago, with an area of ~1300 km^2 (Fig. 2.3). The peninsula can be divided into three distinct regions (Nougier, 1970). To the west is a 450 km^2 mountainous region that has experienced intense glacial erosion, resulting in the formation of deep glacial valleys. This region is predominantly comprised of volcanic rocks, and includes the 1000 m Mt. Crozier basaltic section. To the east is a 780 km^2 low-lying swampy region composed of glacial moraine deposits, which overlie the basaltic basement. To the southeast is a small 40 km^2 peninsula composed of alkalic basalts, basanites, and phonolites.

The volcanic region of the Courbet Peninsula is composed primarily of near-horizontal layers of basaltic lava flows and pyroclastic deposits. A 1000 m high stratigraphic section on the northeast flank of Mt. Crozier, from Val Studer to the summit, was sampled for detailed petrographic and geochemical studies in 1993 (Scoates *et al*., in preparation). The Crozier section consists of variably porphyritic flows dominated by plagioclase, with minor clinopyroxene, olivine and Fe-Ti oxides (Damasceno *et al*., 2002). Clinopyroxene-liquid thermobarometry and clinopyroxene structural barometry indicate that the Crozier magmas crystallized at pressures ranging from 1 to 12 kbar (Damasceno *et al*., 2002). Mt. Crozier is one of the most important sections on the archipelago, as it is interpreted to be representative of the enriched component of the Kerguelen plume (Weis *et al*., 2002).

Large plutons, as well as thin dikes and sills, locally intrude the volcanic region of the Courbet Peninsula. Montagnes Vertes and Monts des Mamelles are two of the largest intrusions. They are located in the center of the volcanic region (Fig. 2.3), having been

exposed by glacial erosion. Nougier (1970) suggested that the Courbet Peninsula is a single volcanic unit and that these intrusions represent its sub-volcanic conduit system. A considerable region of volcanic breccia can be found in the northwest part of the peninsula. Seismic studies have revealed the existence of high-density material underlying this breccia, which may be due to the presence of a large, shallow intrusive body in the subsurface (Charvis *et al*., 1995).

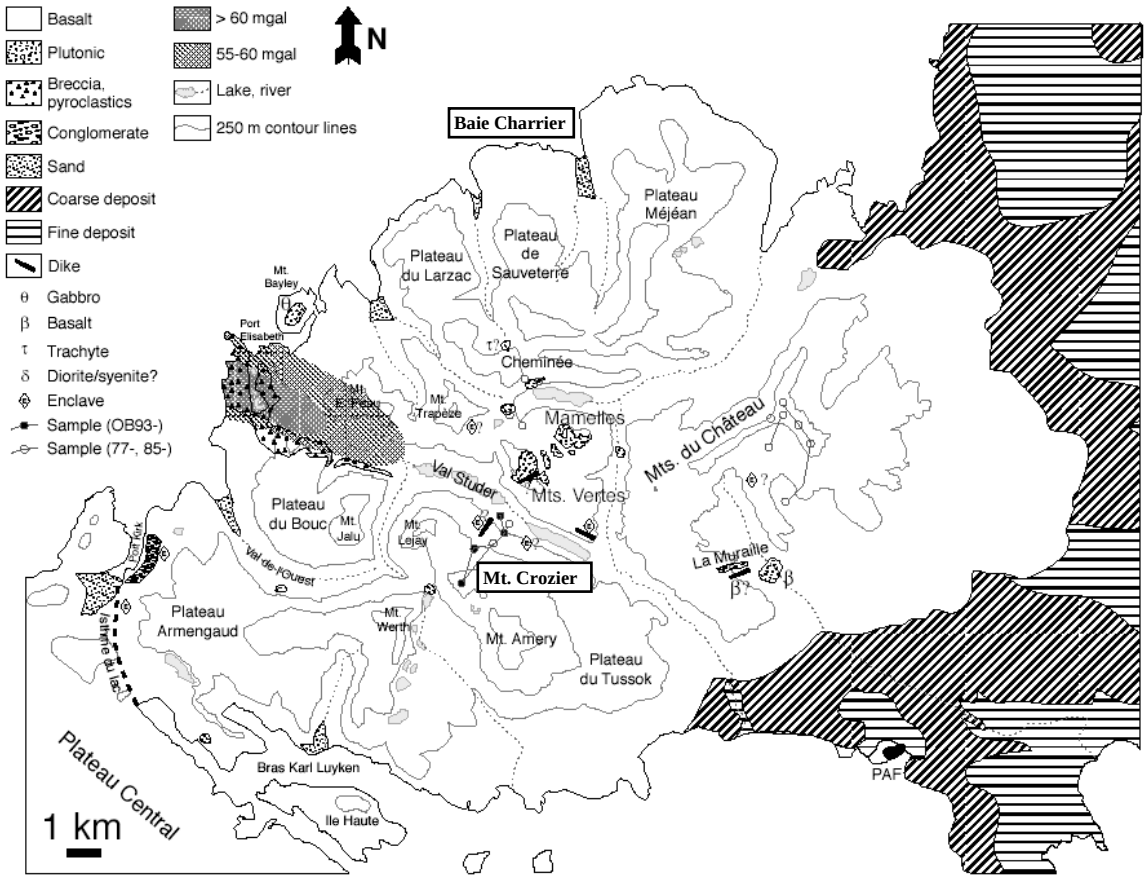

Fig. 2.3. Simplified geologic map of the Courbet Peninsula. Note the mountainous volcanic region to the west and the region covered by glacial deposits to the east. Note also the intrusive complexes in the center, the high-density zone in the northwest, and the location of the Mt. Crozier and Baie Charrier stratigraphic sections.

2.4 The Baie Charrier Stratigraphic Section

Baie Charrier is located on the northern part of the Courbet Peninsula (Fig. 2.3). Basalt flows in this area are typical of those found in other parts of the archipelago, as they are relatively thin and approximately horizontal. The distinctive phenocryst content of the Baie Charrier basalts is of particular interest, and one of the main motivations for studying this section. Olivine and clinopyroxene-phyric basalts are abundant in this section, yet absent in the 1000 m Mt. Crozier section.

Samples were collected as part of the CartoKer Mapping Program in 1994. In total, 33 samples (MM94-228 to MM94-260) were collected from a 325 m high section of basaltic flows. The lowest sample was obtained from an elevation of 85 metres above sea level and the highest was obtained from 410 m. These flows ranged in thickness from 2-15 m, with an average of approximately 5.5 m. The samples collected were identified in the field as either aphyric or containing combinations of olivine, plagioclase or pyroxene phenocrysts. The presence of local zeolite alteration was also noted in some samples.

Of the 33 samples from the Baie Charrier section, 15 were selected for detailed geochemical analyses based on freshness, stratigraphic position and phenocryst content. These samples encompass a range of elevations, including the stratigraphically highest and lowest samples. Of these 15 samples, 10 polished thin sections were prepared, 8 were selected for mineral chemistry, and 11 were selected for isotopic analysis (see Chapter 3: Analytical Techniques).

3.1 Mineral Chemistry

Eight samples were selected for electronprobe microanalysis of olivine and clinopyroxene phenocryst compositions. The other two samples, MM94-230 and MM94-244, were not analysed as they do not contain clinopyroxene phenocrysts and the olivines are completely replaced by iddingsite, a common low temperature alteration product. Between 3 and 6 phenocrysts of olivine from each thin section were selected. Clinopyroxene phenocrysts were also chosen when present. Selection of a particular crystal was based mainly on degree of alteration; the crystals chosen showed minimal alteration and were isolated (i.e. not bordering other crystals). Core, mid, and rim positions on the crystal were carefully chosen. A clear spot, free of inclusions and fractures was required for analysis of mineral composition. Probe traverses were mapped onto the thin sections, which were subsequently carbon-coated prior to analysis.

The phenocrysts were analyzed on a Cameca SX-50 electron microprobe at the University of British Columbia with an accelerating voltage of 15 kV, a beam current of 15 nA, a peak count time of 20 s, and a background count time of 10 s. Calibration was made with natural olivine and clinopyroxene standards. Data reduction was made with a PAP $\varphi(\rho z)$ correction procedure. In total, 102 olivine analyses (34 phenocrysts) and 15 clinopyroxene analyses (5 phenocrysts) were completed. Mineral compositions for olivine and clinopyroxene are reported in Appendix A and Appendix B, respectively.

3.2 Previous Whole Rock Sample Preparation

Initial sample preparation was carried out at the Université Libre de Bruxelles in Belgium. The samples were cut using a diamond-embedded saw to remove surface alteration. The cut surface was then abraded with sandpaper to eliminate any saw traces

or residual alteration. The samples were coarse-crushed in a hydraulic piston crusher between WC-plates using the percussion method (no grinding). The samples were subsequently reduced to powder in an agate planetary mill.

3.3 Major Element Compositions

All 15 samples were analysed for major element compositions and some trace elements (Rb, Sr, Ba, V, Cr, Ni, Zn, Ga, Y, Zr, Nb, Ce and La) by X-ray fluorescence (XRF) at the University of Massachusetts, Amherst (see Rhodes, 1996 for analytical procedure). Major and trace element compositions by XRF are the mean of duplicate analyses and are reported in Table 3.1.

3.4 Trace Element Concentrations

Samples were prepared and analysed at the Pacific Centre for Isotopic and Geochemical Research (PCIGR) of the University of British Columbia. The procedure involved loading, digesting, and diluting the samples in preparation for analysis by High-Resolution Inductively Coupled Mass Spectrometry (HR-ICP-MS). Trace element abundances by HR-ICP-MS are reported in Table 3.1.

3.4.1 Loading

Approximately 0.1 g of each sample were weighed into clean 15 ml Savillex® vials using a Mettler Toledo balance. Fifteen samples were loaded plus the U.S.G.S. reference materials BCR-1 (Basalt, Columbia River) and BHVO-1 (Basalt, Hawaiian Volcanic Observatory). Replicates of both reference materials and two samples chosen at random were loaded to monitor the accuracy and reproducibility of the analytical

techniques. Two procedural blanks were also included to detect any contamination during the sample preparation.

3.4.2 Digestion

To dissolve the powders, 2 ml of concentrated sub-boiled HF and 500 µl of concentrated Seastar® HNO_3 were added. The samples were sealed and placed on a hotplate for 48 hours at a temperature of approximately 120 ºC. Twice during this time interval, the samples were placed in an ultra-sonic bath for 15 minutes to ensure complete dissolution of the powder. The samples were then uncapped and placed on a hotplate to dry down. Once dry, 2 ml of Seastar® concentrated HNO_3 were added. After 24 hours on the hotplate, the samples were again allowed to dry down. Approximately 4 g of 1% HNO_3 with 1 ppb Indium (In) were added using the Mettler Toledo balance. The samples were placed on a hotplate for 24 hours. Twice during this time interval, the samples were placed in an ultra-sonic bath for 15 minutes to ensure complete redissolution.

3.4.3 Dilution

The samples were then transferred to clean 125 ml HDPE sample bottles. Two separate dilutions were carried out. Samples were diluted to 1000x for the rare earth elements, and to 2000x for the high field strength elements. They were first diluted to 1000 times their initial weight with 1% HNO_3 with 1 ppb In using the Mettler Toledo balance. A portion of this diluted mixture was transferred to clean 60 ml HDPE sample bottles and subsequently diluted to 2000x. Various amounts of concentrated HCl were added to each of the 2000x dilutions so that the resulting solutions would have a concentration of 1% HCl.

3.4.4 Trace Element Analysis by High-Resolution Inductively Coupled Plasma Mass Spectrometry (HR-ICP-MS)

The samples were analysed on the Element2 (Finnigan MAT) HR-ICP-MS at the PCIGR at the University of British Columbia. The rare earth elements were measured in high resolution, while Pb and U were measured in low resolution. The majority of the high field strength elements were measured in medium resolution, with the exception of Cd, Sn, Sb, Cs, Ta, W, and Bi, which were also measured in low resolution. Using higher resolution enables potential interferences to be resolved, while using lower resolution enables the measurement of less abundant elements through increased instrument sensitivity. A series of 6 standards, obtained by series dilution from 1000 ppm High Purity® stock standard solutions using 1% HNO3 with 1 ppb In, were used for external calibration and concentration calculation. Procedural blank values were in the parts-per-trillion (ppt) range, and are considered negligible in comparison to the sample concentrations, which are in the parts-per-million (ppm) range.

When performing analyses by HR-ICP-MS, memory effects, sensitivity drift, and mass drift must be monitored and, if present, corrected for. A solution of 4% Aqua regia + 0.05% HF was used to rinse the instrument between each sample to minimize memory effects from the previously analysed sample. Background values were checked periodically during the course of analysis, especially after high abundance samples or standards, to detect and correct for memory effects. Indium, which is spiked at 1 ppb in all blank, standard, and sample solutions, was used as an internal standard to monitor and correct for sensitivity drift. Low level (5 ppb) REE standard solutions were run after every fifth or sixth sample to detect and correct for instrumental mass drift.

3.5 Pb-Sr-Nd Isotopic Compositions

3.5.1 Sample Selection

The amount of weight loss on ignition (LOI), coupled with petrographic observation, were significant factors in determining which samples would be selected for isotopic analysis. LOI was used as an indication of alteration, and a maximum value of 2.75 wt.% LOI was decided upon. Samples with LOI above this value were dismissed as possible candidates for isotopic work due to their greater degree of alteration. The choice of this value also took into consideration the need to encompass the observed variation in MgO and Zr/Nb (see Chapter 4: Results). Samples from the stratigraphic top and bottom of the section were also selected.

3.5.2 Loading

Samples for isotopic compositions were prepared and analysed at the PCIGR at the University of British Columbia. The procedure involved loading, leaching and digesting the samples followed by column chemistry and analysis by Thermal Ionization Mass Spectrometry (TIMS) and Multi-Collector Inductively Coupled Plasma Mass Spectrometry (MC-ICP-MS). In total, 11 samples were loaded, plus two replicates, and one procedural blank. For samples with greater than 2 ppm Pb, approximately 400 mg of powder was added to a clean 15 ml Savillex® vial using a Mettler Toledo balance. For samples with less than 2 ppm Pb, approximately 800 mg of powder was added to ensure enough Pb would remain for analysis after leaching and column chemistry.

3.5.3 Leaching

The samples were acid-leached (Weis & Frey, 1991) to remove any secondary

alteration products such as zeolites and carbonates, which are typically found in basalts from the Kerguelen Archipelago. Approximately 10 ml of 6N quartz-distilled HCl were added to each vial. The samples were placed in an ultra-sonic bath for 15 minutes. The supernatant fluid was then discarded. This procedure was repeated until the supernatant fluid was clear. A few of the samples were finished after 9 repetitions, but most required 11 repetitions. Approximately 10 ml of doubly-deionized water (DDW) were then added to each vial. After 10 minutes in an ultra-sonic bath, the supernatant fluid was discarded and the samples were placed on a hotplate to dry down. Once dry, the samples were weighed to determine how much powder remained after the leaching process. To ensure the samples were completely dry, they were placed back on the hotplate for 30 minutes and then re-weighed. The samples were considered dry when the weight of the sample remained constant. On average, 215 mg of sample was lost during the leaching process, corresponding to between 25% and 50% of the initial weight.

3.5.4 Digestion

Approximately 1-2 ml of sub-boiled concentrated HNO_3 and 8-9 ml of sub-boiled concentrated HF were added to each of the leached samples. The Savillex® vials were sealed and placed on a hotplate for 48 hours at a temperature of approximately 110 ºC. Once during this time interval, the samples were placed in an ultra-sonic bath for 15 minutes. After the samples had dried down on the hotplate, approximately 10 ml of quartz-distilled 6N HCl were added, and they were placed back on the hotplate for 48 hours. Twice during this time interval, the samples were placed in an ultra-sonic bath for 15 minutes. The vials were once again uncapped and allowed to dry down on the hotplate.

3.5.5 Pb Column Chemistry

Pb separation chemistry was carried out using six 1.5 cm Pb anion exchange columns containing Biorad® AG1-X8 100-200 mesh chloride-form resin and Frits filters. This procedure involves adding either acid or doubly-deionized water (DDW) to the columns by pipette and allowing the liquids to drain through into waste trays or Savillex® vials. It should be noted that each solution was allowed to drain though completely before the next solution was added. As well, when adding the solutions, care was taken to minimize the disturbance of the resin.

To properly condition the columns, 1 ml each of the following were added: DDW, 0.5N HBr, 6N HCl, DDW, 0.5N HBr, 6N HCl, DDW, 0.5N HBr (Table 3.2). These solutions were allowed to drain through and were collected in waste trays. To prepare the samples, 2 ml of HBr were added to each. The vials were placed on a hotplate for about 5 minutes, and then placed in an ultra-sonic bath for 5 minutes. After ensuring complete re-dissolution, the acid mixture was carefully transferred to 5 ml centrifuge tubes and placed in a centrifuge for 6 minutes. The samples, in 2 ml HBr, were then transferred to the columns by pipette, ensuring that any material that had settled was not incorporated. To each column, 1 ml 0.5N HBr was added followed by 0.5 ml 0.5N HBr. The liquid that drained through the columns following the addition of these last two acids was collected in 15 ml Savillex® vials. This liquid contained the Sr and rare earth elements (REE), and was thus retained for future Sr and Nd isotope chemistry. The Pb was collected in 7 ml Savillex® vials after the addition of 1 ml of 6N HCl. All vials were then placed on a hotplate to dry down.

3.5.6 Sr Column Chemistry

Sr and REE separation chemistry was carried out using six 15 cm Sr cation exchange columns containing Biorad® AG-50W-X8 100-200 mesh hydrogen-form resin. To each sample collected from the Pb columns containing the Sr and REE that were subsequently dried, 5 ml of 1.5N HCL were added. The vials were placed on a hotplate for about 5 minutes, and then placed in an ultra-sonic bath for 5 minutes. After ensuring complete re-dissolution, the acid mixture was carefully transferred to 5 ml centrifuge tubes and placed in a centrifuge for 6 minutes. The samples, in 5 ml 1.5N HCl, were then transferred to the columns by pipette (Table 3.3). Subsequently, 1 ml of 1.5N HCl was added, followed by 50 ml of 2.5N HCl. The liquid that drained through was collected in waste trays. The Sr was collected in plastic beakers following the addition of 35 ml 2.5N HCl and 10 ml 4N HCl. Next, 13 ml 4N HCl were added and collected in the waste trays. The REE were collected in plastic beakers following the addition of 40 ml 4N HCl. The columns were then cleaned with one full reservoir (100ml) of 6N HCl and another of 1.5N HCl. The beakers containing the Sr and REE were placed on a hotplate to dry down.

3.5.7 Nd Column Chemistry

Nd separation chemistry was carried out using six quartz columns containing Teflon (PTFE) beads coated with di-2 ethylhexylorthophosphoric acid (HDEHP). These beads, when coated with this particular organic compound, can be used as an ion exchange medium (Cheatham, 1996). To each sample collected from the Sr columns, containing the REE, 0.5 ml 0.16N HCl was added. The samples were then placed in an ultra-sonic bath for 5 minutes, and then transferred to the columns by pipette (Table 3.4).

Subsequently, 0.5 ml 0.16N HCl was added to the columns. This step was repeated three times, followed by 2 ml of 0.16N HCl, with the resulting liquids that drained through collected in waste trays. The Nd was collected in Savillex® vials following the addition of 4 ml 0.16N HCl. The columns were then cleaned three times with 10 ml 6N HCl and twice with 10 ml 0.16N HCl. The vials containing the Nd were placed on a hotplate to dry down.

3.5.8 Pb Isotopic Analysis by Multi-Collector Inductively Coupled Plasma Mass Spectrometry (MC-ICP-MS)

Each sample was dissolved in 1 ml of 0.05M HNO_3. A 100 µl aliquot was taken from this solution and diluted by adding 1.9 ml of 1% HNO_3 with 1 ppb In. These samples were analysed on the Element2 ICP-MS to determine the content of Pb in each sample. Depending on the amount of Pb in each sample, aliquots of between 25% and 100 % were taken from the remaining 0.9 ml solutions and diluted to 2 ml with 0.05M HNO_3. This was to ensure that a minimum 2V ^{208}Pb signal would be exceeded in all the samples during analysis. The samples were spiked with a solution of 5 ppm Thallium (Tl) obtained by dilution from a concentrated Tl Specpure® atomic absorption spectroscopy standard solution. For every ng of Pb present in the samples, 0.25 ng of Tl was added to achieve a Pb/Tl ratio of 4, which is critical for proper correction for mass fractionation.

The samples were analysed on the Nu Instruments Nu Plasma MC-ICP-MS at the PCIGR at the University of British Columbia. The Nu Plasma offers high precision and high sensitivity Pb isotopic analyses. A desolvation nebulizer (DSN) was used with a nebulizer pressure of 37 psi, hot gas flow of 0.23 L/min, and membrane gas flow of 3.01

L/min. Membrane and spray temperatures were 110 ºC. The uptake rate of the Glass Expansion Micromist nebulizer was between 150-160 µl/min.

Before any samples were analysed, a batch of 5 NBS 981 (50 ppb) Pb standards were run. This standard was subsequently analysed after every 2 samples and twice at the end. This standard-sample bracketing was used to monitor and correct for instrumental drift during the course of analyses. After each sample or standard, the uptake tube was rinsed in doubly-deionized water and placed in 3% HNO_3. After each standard, the tube was additionally placed in 10% HNO_3. During the washing, the background intensity of ^{208}Pb was monitored for a period of ~5 minutes. When an acceptable background intensity was reached (<2 mV) and no further decrease observed, the uptake tube was placed in 0.05M HNO_3 to equilibrate the system prior to analysis.

Pb isotopic compositions were measured in the static mode with an interference correction for ^{204}Hg. Pb compositions in each sample are derived from the mean of 60 analyses (3 blocks of 20 cycles) and are reported in Table 3.5. Pb isotopic data was corrected for mass fractionation using $^{205}Tl/^{203}Tl = 2.3885$. Average triple spike values for NBS 981 were $^{206}Pb/^{204}Pb = 16.9423 \pm 0.0017$ (2sd), $^{207}Pb/^{204}Pb = 15.4980 \pm 0.0015$ (2sd), and $^{208}Pb/^{204}Pb = 36.7188 \pm .0.0041$ (2sd). These values fall within 2σ error of the accepted triple spike values ($^{206}Pb/^{204}Pb = 16.9405$, $^{207}Pb/^{204}Pb = 15.4963$, and $^{208}Pb/^{204}Pb = 36.7219$) (Galer & Abouchami, 1998). The procedural blank contained 150 $\pm$ 1 pg Pb, which is negligible in comparison to the Pb content of the samples.

3.5.9 Sr and Nd Isotopic Analysis by Thermal Ionization Mass Spectrometry (TIMS)

The Sr samples were dissolved in 1M H_3PO_4, and 2 µl of this solution was loaded onto single Ta filaments. The Nd samples were dissolved in 0.1M H_3PO_4, and 2 µl were

loaded onto double Re-Ta filaments. To load ~400 ng Sr and ~150 ng Nd onto the filaments, every 200 ng of Sr required dilution by 1 µl of 1M H_3PO_4, while every 75 ng of Nd required 1 µl of 0.1M H_3PO_4. Therefore, to determine how much 1M or 0.1M H_3PO_4 to add, the amount of Sr and Nd in the sample had to be calculated. The initial amount of Sr and Nd prior to column chemistry was calculated by knowing the weight of the sample and the concentration of Sr and Nd in the sample, measured previously by HR-ICP-MS. The amount of Sr and Nd lost through column chemistry was then subtracted from this initial value. Sample loss is assumed to be 15% for each set of columns (Doucet *et al*., 2002). Thus, 72.3% of the initial Sr remained after passing through Pb and Sr columns, and 61.4% Nd remained after Pb, Sr, and Nd columns.

The samples were analysed on the Thermo Finnigan Triton-TI TIMS at the PCIGR at the University of British Columbia. Sr and Nd isotopic compositions were measured in the static mode with relay matrix rotation. Sr and Nd compositions in each sample are the mean of 135 analyses (9 blocks of 15 cycles) and are reported in Table 3.6. During the course of analyses, 10 analyses of the NBS 987 Sr standard and 10 analyses of the La Jolla Nd standard were made, with mean values of $^{87}Sr/^{86}Sr$ = 0.710252 $\pm$ 0.000007 (2sd) and $^{143}Nd/^{144}Nd$ = 0.511853 $\pm$ 0.000004 (2sd), respectively. These are within the range of accepted values. Sr isotopic data were corrected for mass fractionation using $^{86}Sr/^{88}Sr$ = 0.1194, while Nd isotopic data were corrected using $^{146}Nd/^{144}Nd$ = 0.7219. Procedural blanks contained 427 pg Sr and 69 pg Nd, which are negligible in comparison to the Sr and Nd content of the samples.

Table 3.1: Major and trace element abundances in basaltic lavas from the Baie Charrier section (major element oxides in wt.%; trace elements in ppm)

Elevation (m):	85	95	100	135	165	175	190	250
Sample:	MM94-238	MM94-237	MM94-236	MM94-233	MM94-231	MM94-230	MM94-229 †	MM94-258
SiO_2	47.83	48.13	46.93	48.08	48.35	47.26	51.34	48.49
TiO_2	2.73	2.31	2.46	2.74	3.14	2.75	2.47	3.11
Al_2O_3	14.57	14.86	14.79	14.70	16.48	17.65	15.97	16.62
Fe_2O_3	12.42	12.61	13.01	12.46	13.58	12.99	12.98	12.48
MnO	0.17	0.17	0.18	0.18	0.17	0.17	0.20	0.17
MgO	8.41	8.70	9.26	8.26	3.95	5.41	3.12	4.58
CaO	8.97	8.43	8.61	9.08	7.63	9.17	6.60	8.79
Na_2O	2.56	2.52	2.27	2.52	3.64	3.11	4.28	3.58
K_2O	1.61	1.54	1.52	1.66	2.01	1.14	2.26	1.47
P_2O_5	0.53	0.53	0.55	0.53	1.06	0.35	1.04	0.46
Total	99.80	99.80	99.58	100.21	100.01	100.00	100.26	99.75
LOI ‡	2.65	3.26	3.10	2.25	2.95	-0.08	1.67	1.89
Sc^{ICP}	24.7	18.5	18.8	24.7	16.9	21.5	16.8	20.2
V^{XRF}	196	151	169	199	140	225	83	243
Cr^{XRF}	235	306	321	238	2	99	1	33
Co^{ICP}	50.9	50.0	54.5	50.4	36.9	51.4	26.7	38.1
Ni^{XRF}	179	180	206	163	19	69	1	32
Zn^{XRF}	117	105	115	116	124	101	148	111
Ga^{XRF}	20	19	21	21	22	20	25	24
Rb^{ICP}	34.5	29.5	27.9	35.4	43.8	20.4	48.4	29.4
Sr^{XRF}	518	655	709	559	625	600	466	533
Ba^{ICP}	343	369	405	351	459	271	499	337
Y^{XRF}	25.4	20.9	19.8	25.5	32.2	19.6	42.9	23.5
Zr^{XRF}	282	229	225	286	308	164	377	230
Hf^{ICP}	5.52	4.44	4.48	5.73	5.87	3.60	7.64	4.90
Nb^{ICP}	44.0	34.0	35.4	43.4	47.7	23.7	57.2	34.3
Ta^{ICP}	2.41	1.78	1.88	2.44	2.56	1.31	3.21	2.00
La^{ICP}	36.6	30.8	32.2	37.1	46.2	19.4	51.4	29.3
Ce^{ICP}	77.8	65.6	72.0	79.8	99.4	42.3	112.7	66.7
Pr^{ICP}	8.71	7.47	8.66	9.27	12.13	4.79	13.36	7.73
Nd^{ICP}	34.6	31.3	34.6	36.0	49.8	21.2	54.1	31.7
Sm^{ICP}	7.23	6.40	6.98	7.34	10.14	4.81	11.19	6.86
Eu^{ICP}	2.46	2.23	2.35	2.43	3.40	1.67	3.61	2.40
Tb^{ICP}	1.06	0.91	0.94	1.05	1.30	0.77	1.53	1.03
Gd^{ICP}	7.10	6.15	6.50	6.95	9.26	5.01	10.50	6.88
Dy^{ICP}	5.15	4.16	4.26	5.14	6.38	3.89	7.92	4.73
Ho^{ICP}	0.96	0.82	0.79	0.98	1.23	0.71	1.51	0.93
Er^{ICP}	2.47	1.94	1.83	2.43	3.03	1.78	3.94	2.35
Yb^{ICP}	2.25	1.80	1.74	2.30	2.64	1.65	3.44	2.13
Lu^{ICP}	0.27	0.21	0.19	0.27	0.32	0.25	0.46	0.26
Pb^{ICP}	3.80	3.15	3.00	3.71	3.75	2.26	4.46	3.14
Th^{ICP}	4.99	3.49	3.42	5.01	4.75	2.26	6.02	3.91
U^{ICP}	2.54	2.26	2.21	2.54	2.22	2.20	2.61	2.20

Table 3.1: continued

Elevation (m):	275	283	290	310	355	375	410
Sample:	MM94-256	MM94-255	MM94-253	MM94-250	MM94-244 †	MM94-242	MM94-240
SiO_2	47.80	47.54	47.75	48.20	49.44	48.99	46.83
TiO_2	2.11	1.90	2.07	3.03	3.54	2.57	1.61
Al_2O_3	14.41	14.40	14.41	17.43	16.27	15.62	9.83
Fe_2O_3	12.78	12.69	12.65	11.78	11.94	12.32	12.29
MnO	0.18	0.18	0.18	0.17	0.17	0.17	0.18
MgO	9.34	10.02	9.73	4.38	4.32	6.33	16.69
CaO	9.91	9.93	9.64	7.92	8.72	9.61	10.22
Na_2O	2.59	2.49	2.18	3.68	3.20	2.64	1.20
K_2O	0.74	0.58	0.68	2.35	1.99	1.25	0.62
P_2O_5	0.26	0.21	0.24	0.79	0.55	0.38	0.19
Total	100.12	99.94	99.53	99.73	100.14	99.88	99.66
LOI ‡	1.48	0.07	2.74	0.83	3.74	2.28	0.82
Sc^{ICP}	27.2	29.4	28.3	12.2	22.3	26.7	32.0
V^{XRF}	229	219	220	154	238	231	190
Cr^{XRF}	455	511	453	8	33	149	925
Co^{ICP}	54.5	61.2	57.0	32.8	33.1	42.7	79.1
Ni^{XRF}	186	214	191	11	36	77	482
Zn^{XRF}	102	95	98	122	115	105	96
Ga^{XRF}	20	19	20	24	24	22	13
Rb^{ICP}	13.0	11.1	10.9	48.2	37.5	22.8	12.6
Sr^{XRF}	355	321	323	870	513	468	441
Ba^{ICP}	176	134	156	539	379	265	144
Y^{XRF}	19.1	17.5	18.1	25.2	28.4	25.9	15.2
Zr^{XRF}	129	112	122	362	279	210	105
Hf^{ICP}	3.00	2.43	2.64	6.56	5.69	4.43	2.28
Nb^{ICP}	15.7	13.6	15.2	62.0	43.9	29.3	17.1
Ta^{ICP}	0.91	0.68	0.79	3.46	2.43	1.66	0.89
La^{ICP}	13.7	10.8	11.5	52.9	38.6	26.0	13.7
Ce^{ICP}	31.5	25.6	28.4	114.4	83.7	59.6	29.0
Pr^{ICP}	3.85	3.12	3.38	12.54	9.83	7.12	3.35
Nd^{ICP}	17.6	14.6	16.1	47.6	39.5	29.3	15.7
Sm^{ICP}	4.12	3.41	3.66	8.98	8.16	6.24	3.41
Eu^{ICP}	1.44	1.22	1.28	2.96	2.70	2.14	1.15
Tb^{ICP}	0.70	0.62	0.64	1.10	1.16	1.01	0.62
Gd^{ICP}	4.53	3.83	4.03	7.78	7.75	6.45	4.03
Dy^{ICP}	3.66	3.28	3.27	5.34	5.80	5.05	2.89
Ho^{ICP}	0.72	0.64	0.64	0.94	1.08	1.00	0.61
Er^{ICP}	1.78	1.59	1.53	2.30	2.72	2.59	1.43
Yb^{ICP}	1.59	1.46	1.44	2.09	2.52	2.41	1.38
Lu^{ICP}	0.18	0.16	0.14	0.24	0.31	0.31	0.14
Pb^{ICP}	1.65	1.31	1.50	5.26	3.75	2.69	1.38
Th^{ICP}	1.44	1.07	1.23	6.63	4.59	3.08	1.55
U^{ICP}	1.45	1.47	1.37	3.07	2.04	2.16	1.69

† Compositions are the mean of replicate analyses.

‡ LOI is the weight loss on ignition after 30 minutes at 1020 °C.

Table 3.2: Pb isotopic compositions in basaltic lavas from the Baie Charrier section

Elevation	Sample	$^{206}Pb/^{204}Pb$	2sd	$^{207}Pb/^{204}Pb$	2sd	$^{208}Pb/^{204}Pb$	2sd
85	MM94-238	18.4888	0.0016	15.5554	0.0013	39.1310	0.0035
135	MM94-233	18.4905	0.0009	15.5553	0.0008	39.1363	0.0022
175	MM94-230 †	18.386502	0.0011	15.5551	0.0011	38.9512	0.0027
190	MM94-229	18.5168	0.0010	15.5637	0.0014	39.1392	0.0046
250	MM94-258	18.4508	0.0008	15.5559	0.0008	39.0529	0.0024
275	MM94-256	18.2011	0.0010	15.5340	0.0010	38.6643	0.0043
283	MM94-255	18.3499	0.0010	15.5379	0.0009	38.7624	0.0023
290	MM94-253 †	18.1923	0.0017	15.5370	0.0017	38.6762	0.0046
310	MM94-250	18.5861	0.0009	15.5797	0.0008	39.2252	0.0021
375	MM94-242	18.5942	0.0013	15.5704	0.0011	39.2464	0.0032
410	MM94-240	18.6419	0.0011	15.5769	0.0010	39.2493	0.0026

† Compositions are the mean of replicate analyses.

Table 3.3: Sr and Nd isotopic compositions in basaltic lavas from the Baie Charrier section

Elevation	Sample	$^{87}Sr/^{86}Sr$	2sd	$^{143}Nd/^{144}Nd$	2sd
85	MM94-238	0.705237	0.000008	0.512625	0.000005
135	MM94-233	0.705237	0.000007	0.512623	0.000007
175	MM94-230 †	0.7050815	0.000008	0.512632	0.000008
190	MM94-229	0.705239	0.000007	0.512624	0.000007
250	MM94-258	0.705114	0.000008	0.512649	0.000006
275	MM94-256	0.704860	0.000007	0.512664	0.000006
283	MM94-255	0.704965	0.000008	0.512685	0.000010
290	MM94-253 †	0.7051885	0.000008	0.5126665	0.000010
310	MM94-250	0.705178	0.000007	0.512590	0.000007
375	MM94-242	0.705163	0.000007	0.512635	0.000005
410	MM94-240	0.705150	0.000006	0.512621	0.000007

† Compositions are the mean of replicate analyses.

4.1 Stratigraphic Relationships in the Baie Charrier Section

The stratigraphy of the Baie Charrier section will be discussed to provide a context for the remainder of the study. This will be followed by a detailed description of the geochemical and petrographic characteristics of the section. However, it should be noted that this study will focus primarily on the geochemistry rather than the petrography of the samples.

The Baie Charrier section can be subdivided into 4 stratigraphic units (A, B, C, and D) based on their geochemical and petrographic characteristics (Fig. 4.1). Unit A, the lowermost unit, ranges from the base of the section to an elevation of 150 m and consists primarily of olivine-phyric basalts. It was immediately recognized as a separate unit based on the observed enrichment in incompatible elements. The four samples in this unit possess twice the abundance of P_2O_5, K_2O, Zr, Rb, Ba, Ce, and La than other samples at a given MgO content. This unit is also relatively MgO-rich, with all samples having greater than 8 wt.% MgO. Unit B ranges in elevation from 150 m to 265 m and consists of predominantly plagioclase-phyric basalts. The four samples in this unit have lower MgO contents than the previous unit, with less than 5.5 wt.% MgO. These samples also have relatively high alkalinity indexes (A.I. = +1 to +2.5). Unit C is a narrow unit ranging in elevation from 265 m to 300 m and consists primarily of olivine-phyric basalts. This is the most geochemically distinct unit of the section. The three samples that make up this unit have MgO contents slightly higher than Unit A, at over 9 wt.% MgO. They have low alkalinity indexes (~0), with two samples plotting in the tholeiitic field (negative values). Unit C samples have anomalous incompatible element ratios such as Zr/Nb, $(La/Sm)_N$, and Th/Ta. This unit is also isotopically distinct, having the highest $^{143}Nd/^{144}Nd$, low $^{87}Sr/^{86}Sr$ ratios, and the lowest Pb isotopic ratios of the section.

Unit D, the uppermost unit, consists of four samples and ranges in elevation from 300 m to the top of the section at 410 m. Three of the samples have relatively low MgO contents, with less than 6.5 wt.% MgO and are predominantly plagioclase-phyric. The uppermost sample is a picrite with over 17 wt.% MgO and is olivine and clinopyroxene-phyric. These four samples become progressively less alkaline with increasing elevation (A.I. = +2.5 to -1) and have the highest Pb isotopic ratios of the section.

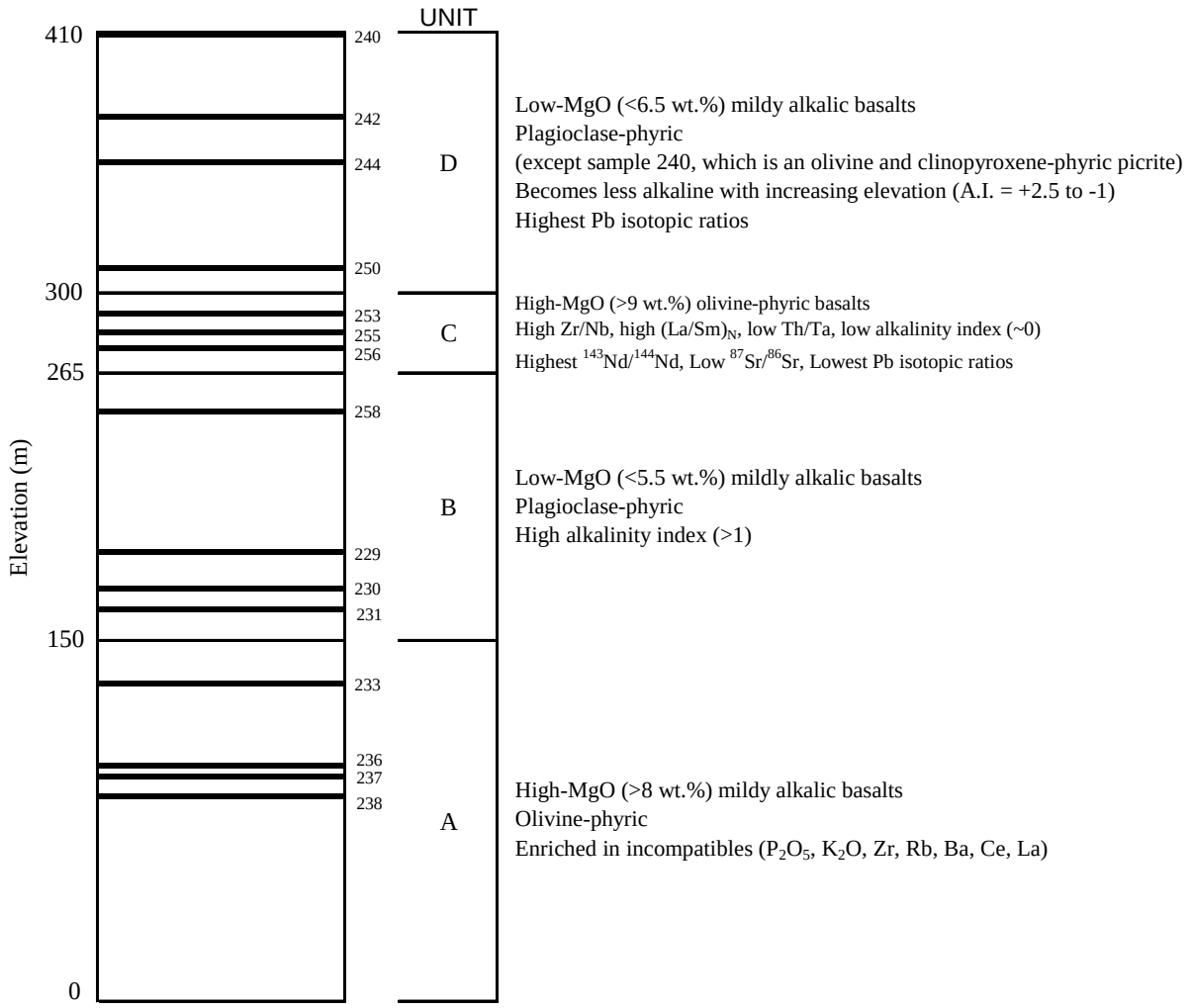

Fig. 4.1. Stratigraphic subdivisions of the Baie Charrier section. The defining petrographic, geochemical and isotopic characteristics of each unit are listed. The thick horizontal black lines indicate the elevations of flows involved in this study. Corresponding sample numbers are written adjacent to these flows.

4.2 Petrography

The Baie Charrier basalts are variably porphyritic; all samples contain phenocrysts of olivine, including several samples that also contain phenocrysts of plagioclase and clinopyroxene (Fig. 4.2). Olivine is the dominant phenocryst in the high MgO basalts of Units A and C, with a modal abundance of ~5%. Crystal habit ranges from euhedral six-sided prisms to rounded, anhedral crystals. Crystal size ranges from 0.25 mm to 5 mm. Most of the olivine phenocrysts are partially to completely replaced by iddingsite, with alteration typically occurring around the edges of the crystal and along fractures. Rarely, the olivines are broken, exhibit undulatory extinction, or are glomerocrystic. Plagioclase is the dominant phenocryst in the low MgO basalts of Units B and D, with a modal abundance of ~10% to ~15%. They are typically euhedral, lath-shaped prisms 1 mm to 6 mm in length. They commonly exhibit simple and polysynthetic twinning and oscillatory zoning. Occasionally, they exhibit undulatory extinction or are glomerocrystic. Phenocrysts of clinopyroxene can be found in the two stratigraphically highest samples (240 and 242) from Unit D, with a modal abundance of ~5%. They range in size from 1 mm to 6 mm. Some of the clinopyroxene phenocrysts are euhedral 8-sided prisms, while others are anhedral and resorbed. Most exhibit simple twinning and have very distinct twin planes. The groundmass in all samples is generally composed of plagioclase microlites, small euhedral opaques, and occasionally small crystals of olivine and clinopyroxene. The groundmass also commonly contains greenish-brown botryoidal or radiating zeolite minerals filling interstices and vesicles.

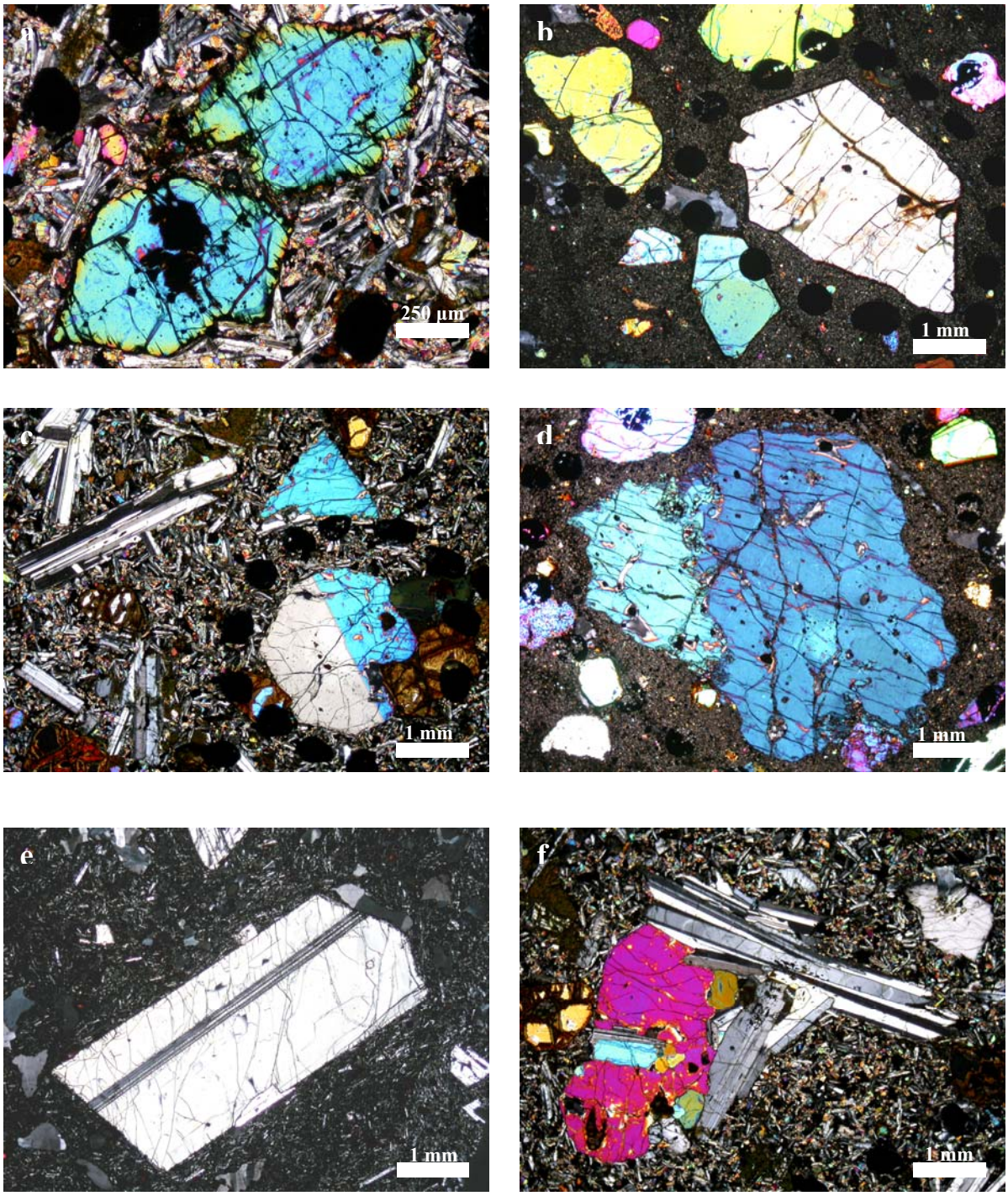

Fig. 4.2. Photomicrographs of phenocrysts from the Baie Charrier basalts. (a) Euhedral olivine from sample 256, a high-MgO basalt. (b) Large olivine phenocrysts from sample 240, the picrite. (c) Euhedral clinopyroxene from sample 242. Note the distinct twin plane. (d) Large resorbed clinopyroxene from sample 240, the picrite. (e) Large euhedral plagioclase lath from sample 230, a low-MgO mildly alkalic basalt. (f) Plagioclase and olivine glomerocrysts from sample 242. All photomicrographs in cross-polars. Black dots are probe traverses.

4.3 Mineral Chemistry

4.3.1 Olivine

The compositional data from the electron microprobe (Appendix A) was converted to forsterite content and plotted versus relative spot position (i.e. core, middle, or rim) on the phenocryst (Fig. 4.3). The olivine phenocrysts are normally zoned, with the rim having a lower forsterite content than either the middle or the core. The middle and core of a crystal typically have very similar forsterite contents. Core compositions are relatively limited, ranging from Fo_{86-70}, while rim compositions vary considerably, ranging from Fo_{81-52}.

4.3.2 Clinopyroxene

The compositional data from the electron microprobe (Appendix B) was converted to $Mg\#_{cpx}$ and plotted versus spot position (Fig. 4.4). The clinopyroxene phenocrysts are normally zoned, with the rims having a lower $Mg\#_{cpx}$ than either the middles or the cores. However, the $Mg\#_{cpx}$ continues to increase from rim to core. Core values of $Mg\#_{cpx}$ range from 0.88 to 0.79, while rim values range from 0.86 to 0.72. The clinopyroxene phenocrysts in the Baie Charrier section are augitic in composition and show relatively little variation when projected onto a pyroxene quadrilateral (Fig. 4.5). This is typical of clinopyroxene phenocrysts from mildly alkalic basalts on the Kerguelen Archipelago (Damasceno *et al*., 2002). Greater variability in the chemistry of the clinopyroxene phenocrysts is observed when considering non-quadrilateral components such as Al (Fig. 4.6). The Al_2O_3 content of the Baie Charrier samples is relatively high and ranges from ~2 wt.% to ~6.5 wt.%.

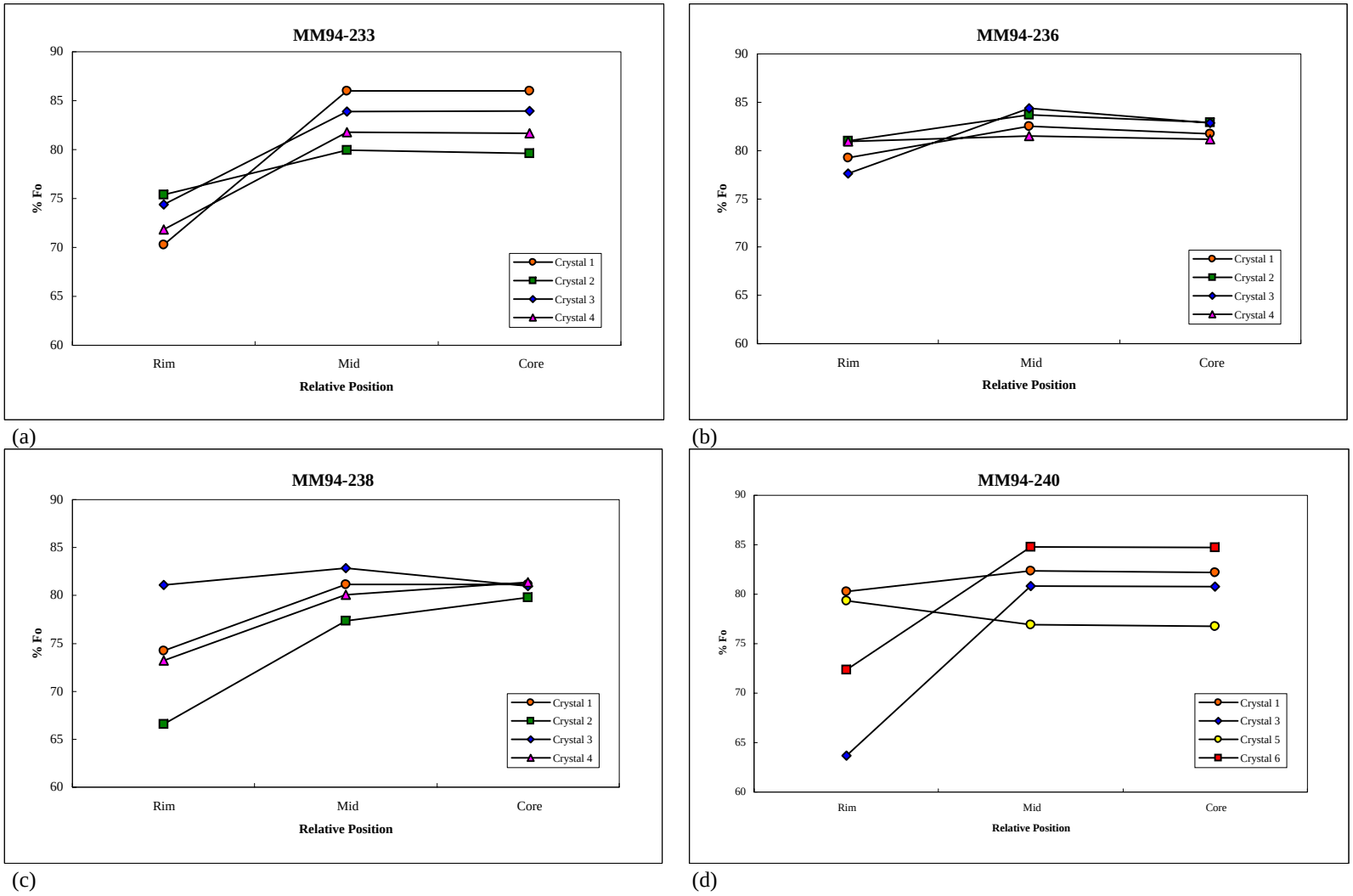

Fig. 4.3. Olivine forsterite content zoning profiles. Sample (a) MM94-233, (b) MM94-236, (c) MM94-238, and (d) MM94-240.

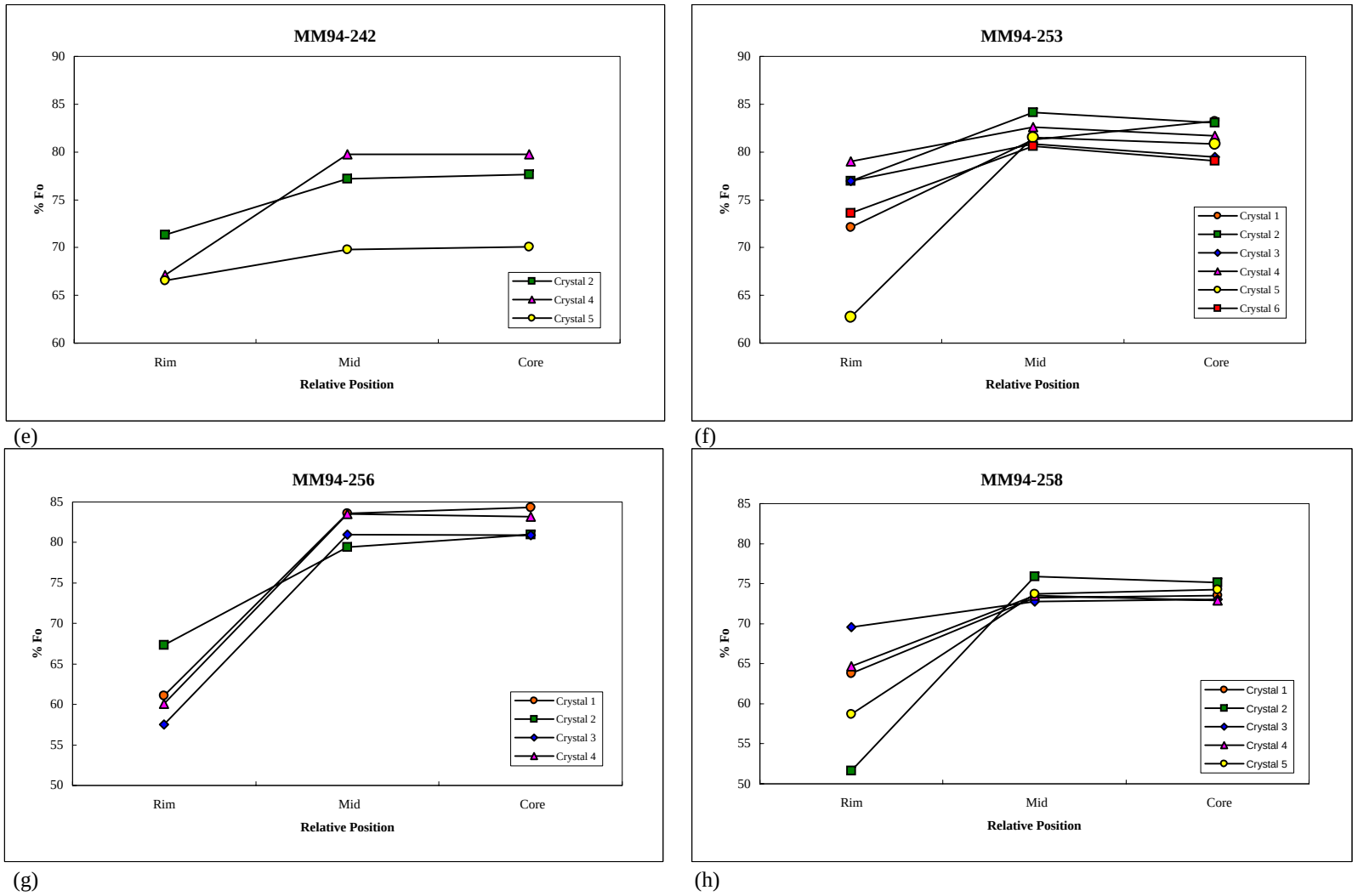

Fig. 4.3. Continued. Olivine forsterite content zoning profiles for samples (e) MM94-242, (f) MM94-253, (g) MM94-256, and (h) MM94-258. Note the change of scale in (g) and (h).

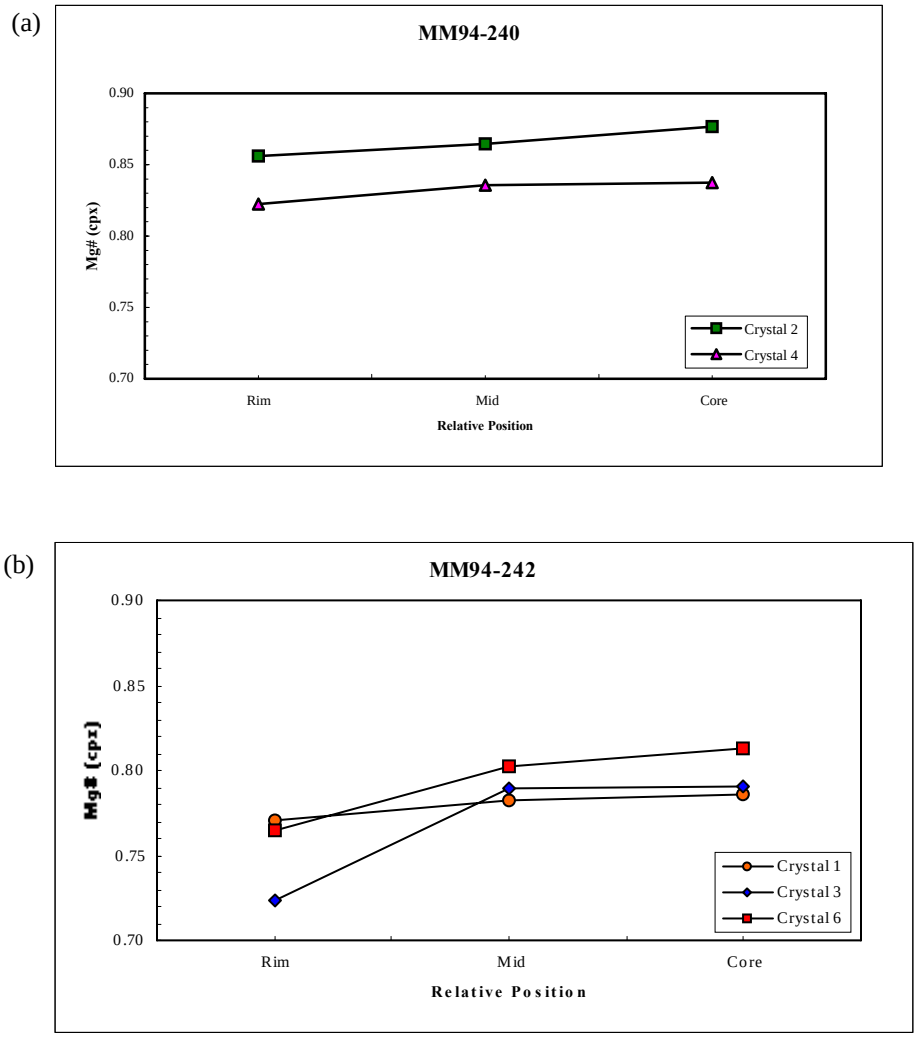

Fig. 4.4. Clinopyroxene Mg# zoning profiles. Samples (a) MM94-240 and (b) MM94-242.

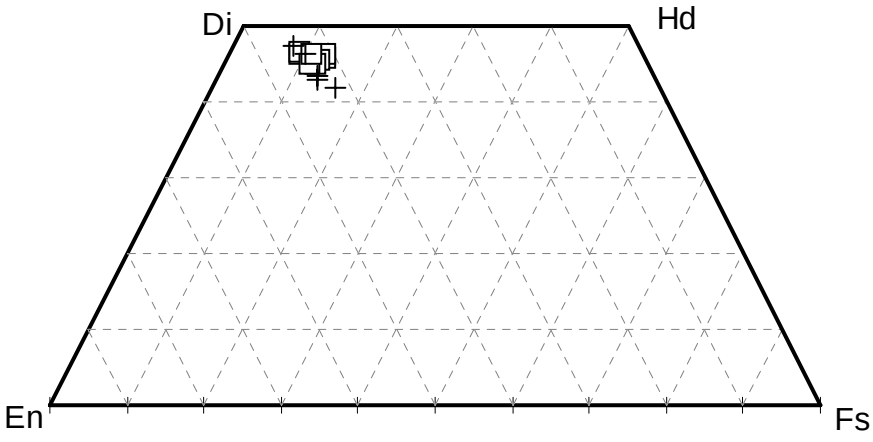

Fig. 4.5. Clinopyroxene phenocryst compositions projected onto a pyroxene quadrilateral. Middle and core compositions are plotted as open squares, rim compositions are plotted as crosses.

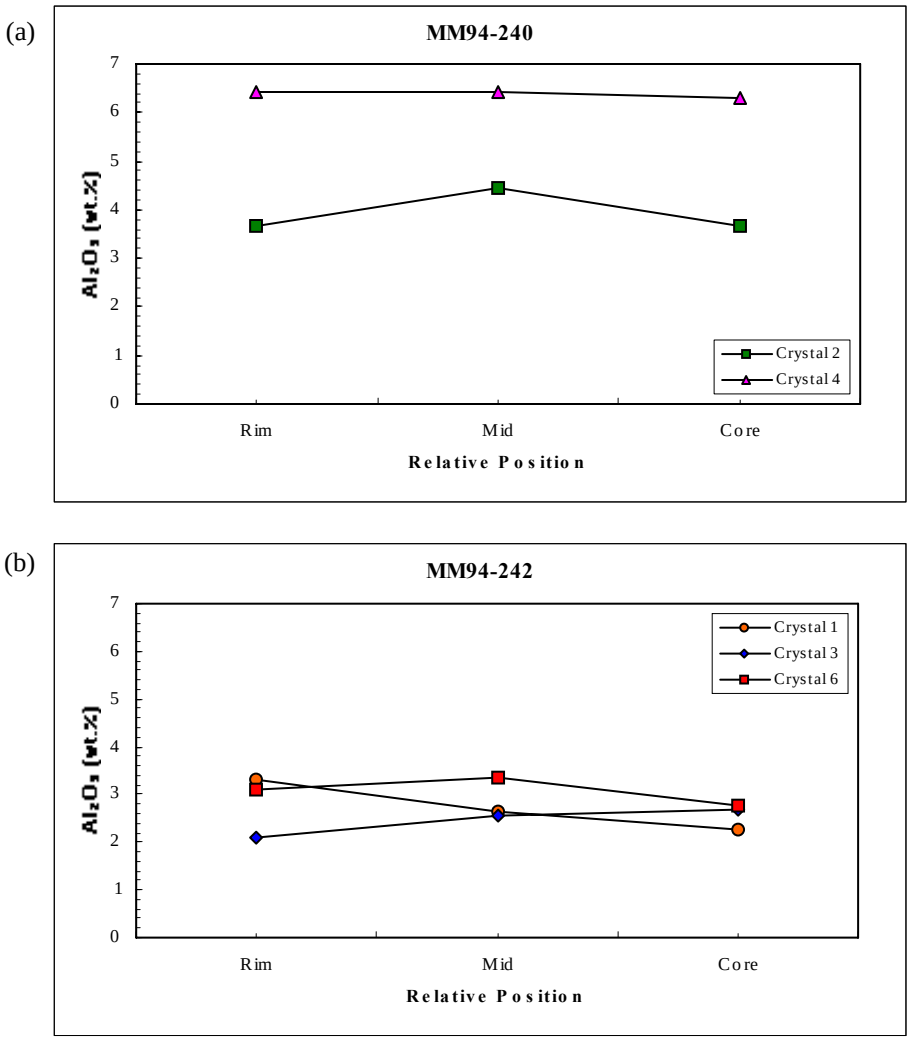

Fig. 4.6. Clinopyroxene Al_2O_3 zoning profiles. Samples (a) MM94-240 and (b) MM94-242.

4.4 Major Elements

To define the basic geochemical characteristics of the Baie Charrier lavas, a total alkali ($Na_2O + K_2O$) versus SiO_2 classification plot was used (Fig. 4.7). The Macdonald and Katsura (1964) tholeiitic-alkalic division is shown for reference; samples plotting above this line are alkalic, while those that fall below are tholeiitic. The majority of the Baie Charrier samples plot slightly above this line, and thus may be characterized as mildly alkalic basalts. This is consistent with other lavas from the Courbet Peninsula

(Damasceno *et al*., 2002). The three samples from Unit C and the uppermost sample from Unit D fall either on or below this line. These samples have the highest MgO contents (>9.73 wt.%) and the highest modal abundances of olivine phenocrysts in the section. The possibility that these samples may have accumulated olivine phenocrysts will be addressed in the following chapter.

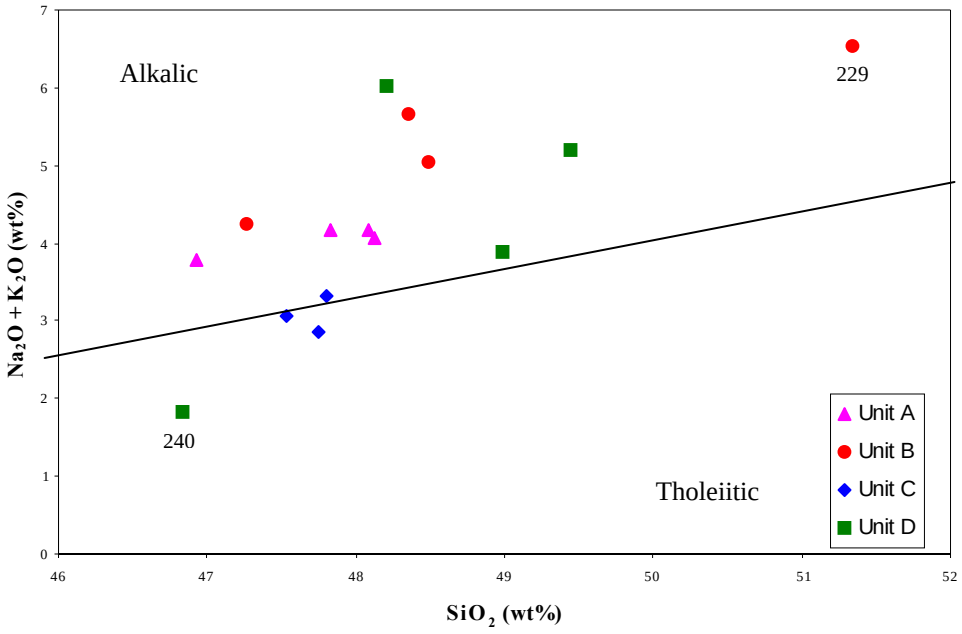

Fig. 4.7. $Na_2O + K_2O$ vs. SiO_2 classification plot. Alkalic samples plot above the Macdonald & Katsura (1964) line, while tholeiitic samples plot below. The Baie Charrier samples are mildly alkalic basalts with the highest MgO samples appearing more tholeiitic.

Elevation plots of alkalinity index and MgO illustrate the stratigraphic variation in the Baie Charrier section (Fig. 4.8) and clearly delineate the major subdivisions of the section. The alkalinity index [$Na_2O + K_2O - 0.37(SiO_2 - 39)$] is a measure of the deviation in $Na_2O + K_2O$ from the Macdonald & Katsura (1964) line; samples with positive values are alkalic, while those with negative values are tholeiitic. Samples in the lower two-thirds of the section are consistently alkalic, followed by a significant

excursion towards less alkalic lavas in Unit C. Unit D then defines a trend of progressively decreasing alkalinity with increasing elevation, ranging from the highest values of the section (+2.6) to the lowest (-1). The elevation plots of alkalinity index and MgO appear to mirror each other, with high MgO corresponding to low alkalinity, and vice versa. The high MgO (~8-11 wt.%) Units A and C are separated by Unit B lavas, which have the lowest MgO (~3-6 wt.%) of the section. Unit D has similarly low MgO, with the exception of the stratigraphically highest sample, which has the highest MgO (>16 wt.%) of the section. Thus, Units A and C may be classified as high MgO basalts (8-12 wt.% MgO) and sample 240 of Unit D is a picrite (>12 wt.% MgO).

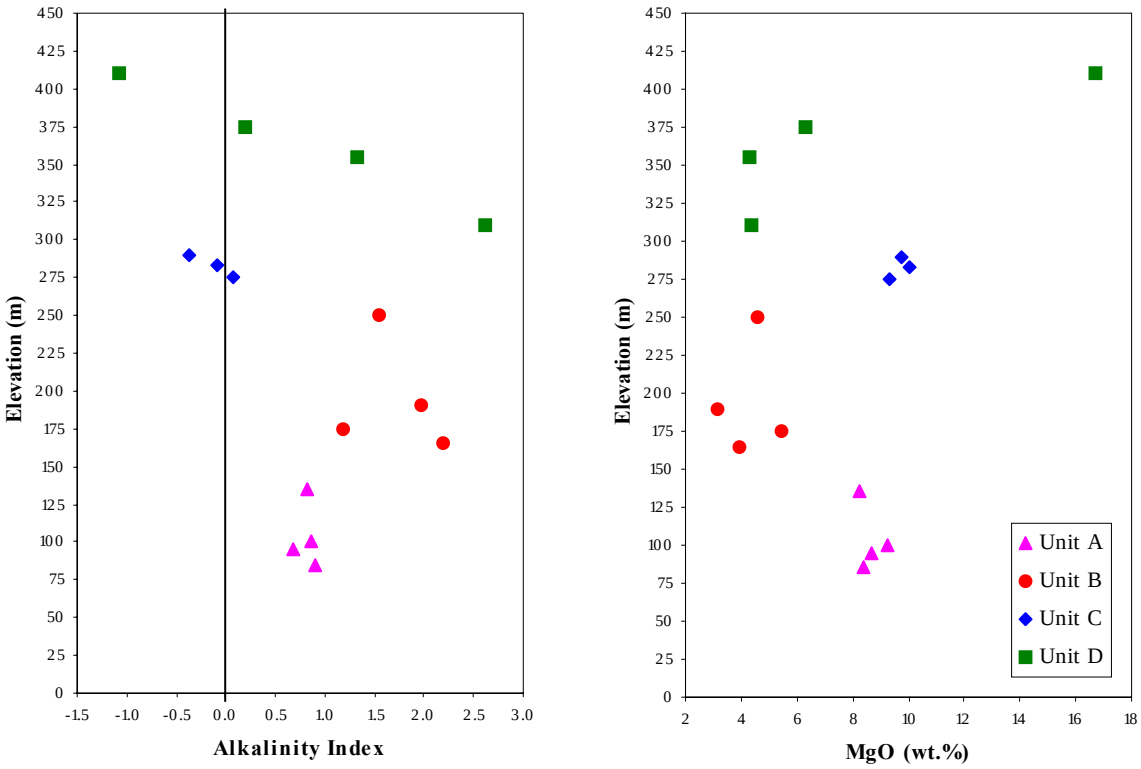

Fig. 4.8. Alkalinity index and MgO abundance vs. stratigraphic height. Alkalinity index [Na2O + K2O - 0.37(SiO2 - 39)] is a measure of the deviation in Na2O + K2O from the Macdonald and Katsura (1964) line in Fig. 4.7. Positive values indicate alkalic samples, while negative values indicate tholeiitic samples.

A selection of major element oxides is plotted vs. MgO in Fig. 4.9. MgO can be used as a differentiation index, ranging from the least to the most differentiated with decreasing MgO. Negative trends are observed in TiO_2 and K_2O, which reflects the residual melt becoming enriched in these incompatible elements as crystallization progresses. Note the distinctive K-rich character of Unit A. The four samples belonging to Unit A can be seen plotting above the regular fractionation trend. A positive trend is observed in CaO below ~6 wt.% MgO and clearly suggests significant clinopyroxene crystallization. Unit A samples have relatively low CaO at a given MgO compared to the other samples. A negative trend in Al_2O_3 is observed, with continuously increasing Al_2O_3 with decreasing MgO, which supports fractionation driven by the crystallization of clinopyroxene and not plagioclase. This is consistent with mildly alkalic 24-25 Ma basalts from the Courbet Peninsula (Damasceno *et al*., 2002) and in contrast to transitional-tholeiitic 26-29 Ma basalts found elsewhere on the archipelago (Yang *et al*., 1998; Doucet *et al*., 2002; Frey *et al*., 2002). SiO_2 exhibits a negative relationship with MgO, with all units appearing to follow the general trend. Fe_2O_3 appears to decrease with decreasing MgO for Units A, C, and most of D, with the exception of the most MgO-rich sample (240) and Unit B.

4.5 Trace Elements

Abundances of Ni, Cr, and Sc are plotted vs. MgO to illustrate the relative compatibility of these elements in the phenocrystic phases (Fig. 4.10). Ni and Cr define positive linear trends; the abundance of these elements decreases with decreasing MgO, reflecting the incorporation of these elements into olivine phenocrysts. Note that Unit C appears to be slightly enriched in Cr relative to the other units. A positive trend is

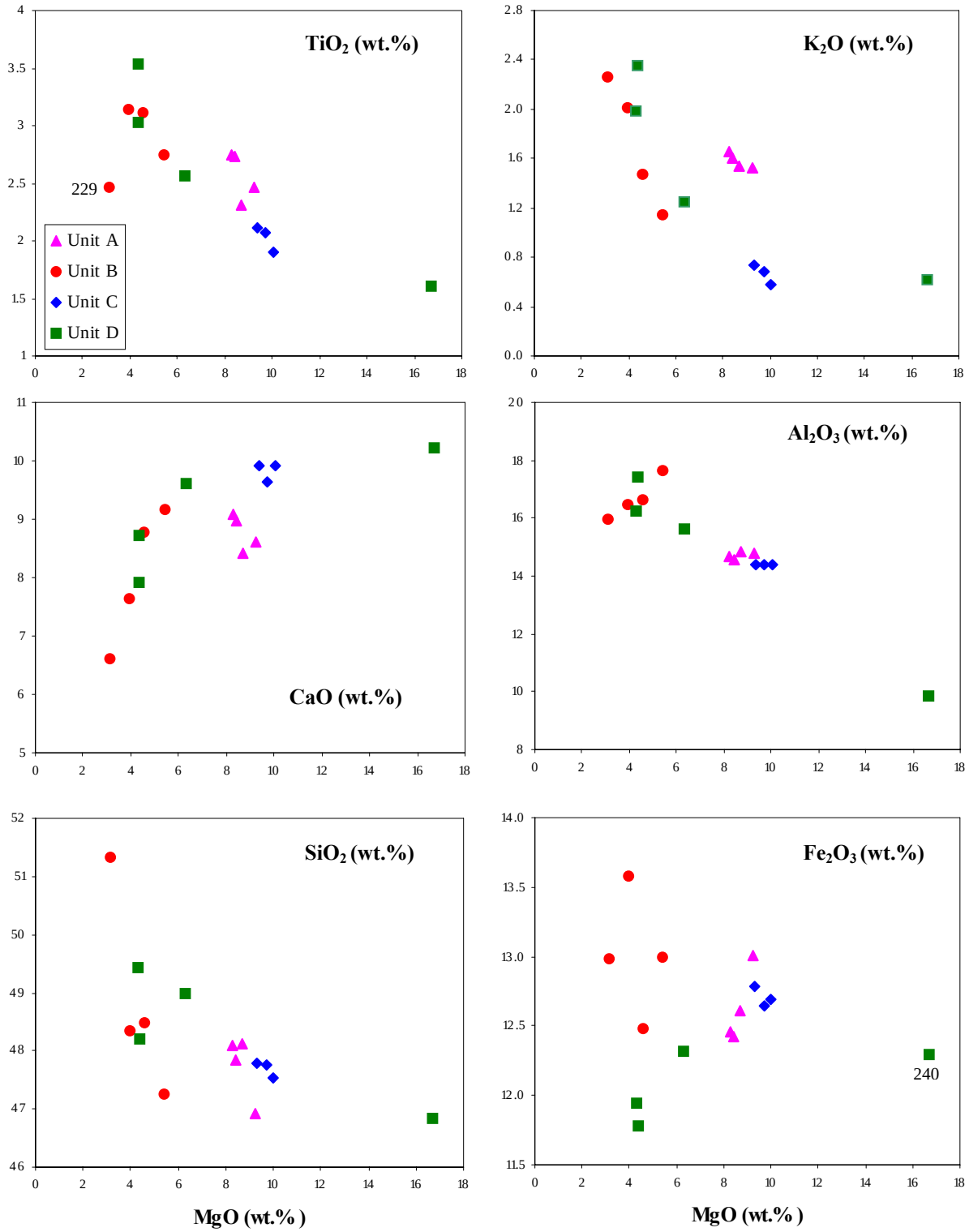

Fig. 4.9. Selected major element oxides vs. MgO. Abundances of TiO_2, K_2O, CaO, Al_2O_3, SiO_2, and Fe_2O_3 (all in wt.%).

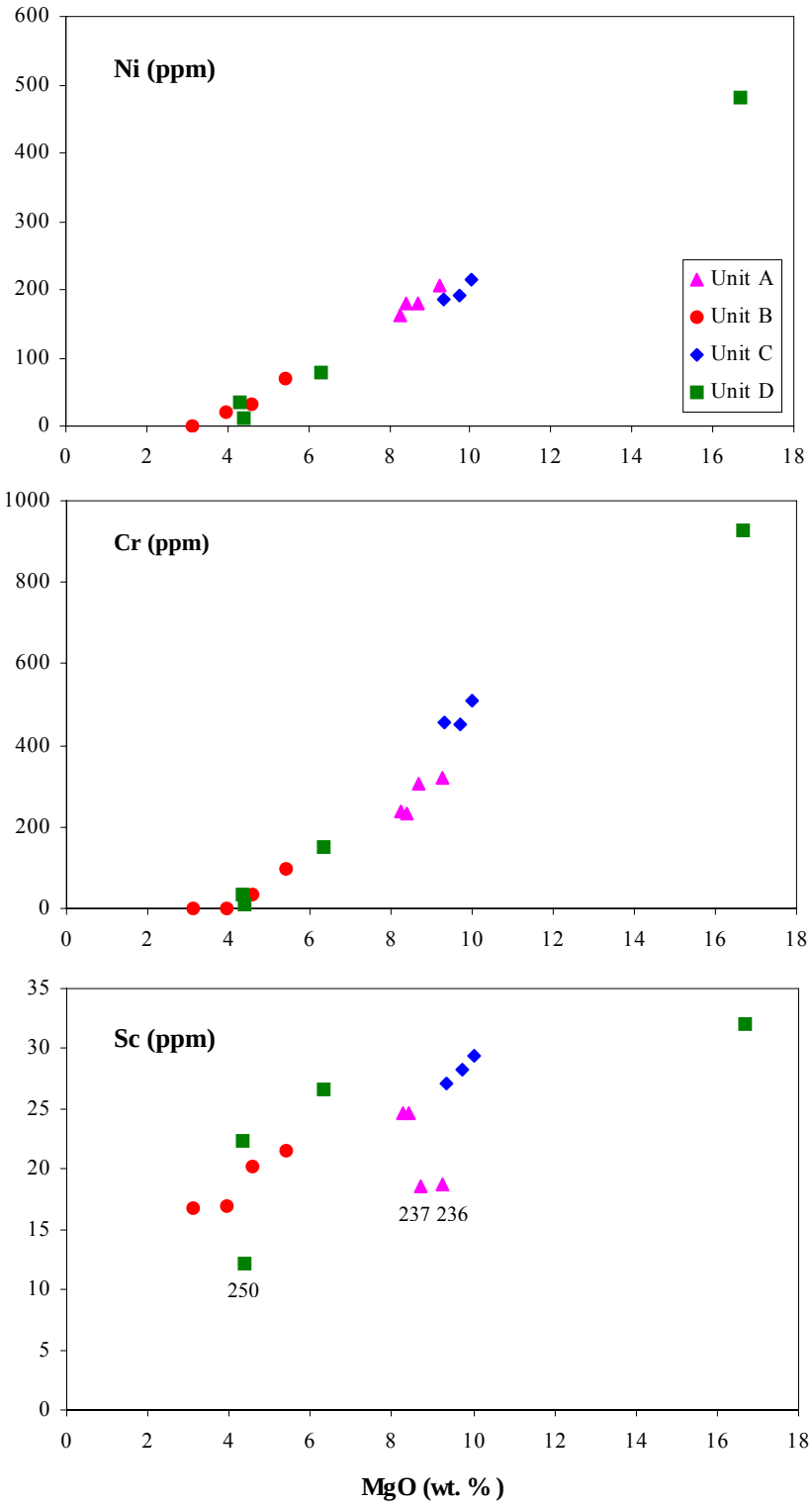

Fig. 4.10. Selection of compatible elements vs. MgO. Abundances of Ni, Cr, and Sc (in ppm) vs. MgO (in wt.%), illustrating the relative compatibility of these elements in olivine and cllinopyroxene phenocrysts.

observed in Sc below ~6 wt.% MgO, reflecting clinopyroxene crystallization and the incorporation of Sc into these phenocrysts. Two samples (236 and 237) from Unit A as well as sample 250 from Unit D have relatively low Sc at a given MgO compared to the other samples.

Abundances of Rb, Ba, Sr, Ce, Zr and Th are plotted vs. Nb to illustrate the relative incompatibility of these elements in the phenocrystic phases (Fig. 4.11). Sr, however, is an exception as it is compatible once plagioclase starts to crystallize. Sample 250 of Unit D likely contains accumulated plagioclase, as it has 870 ppm Sr. Samples 236 and 237 of Unit A also appear to be enriched in Sr as well as Ba. Note that Unit C has the lowest abundances of each of these elements. Strong positive trends are observed between these elements, reflecting the enrichment of these incompatible elements in the residual melt as crystallization proceeds, and dilution through the addition of olivine and clinopyroxene phenocrysts.

As Nb is a significant incompatible element, these plots can be used to derive an incompatibility index for the Baie Charrier basalts. A linear fit to the Rb and Ce data would pass through, or very near to, the origin, indicating that these elements have similar incompatibilities to Nb. This also indicates that the samples were not affected by significant alteration. Trendlines through the Zr and Ba data would intersect the Zr and Ba axes, repectively, indicating that Zr and Ba are more compatible than Nb. Similarly, a trendline through the Th data would intersect the Nb axis, indicating that Nb is more compatible than Th. This results in the following order of increasing compatibility: Th < Ce, Nb, Rb < Ba < Zr < Sr.

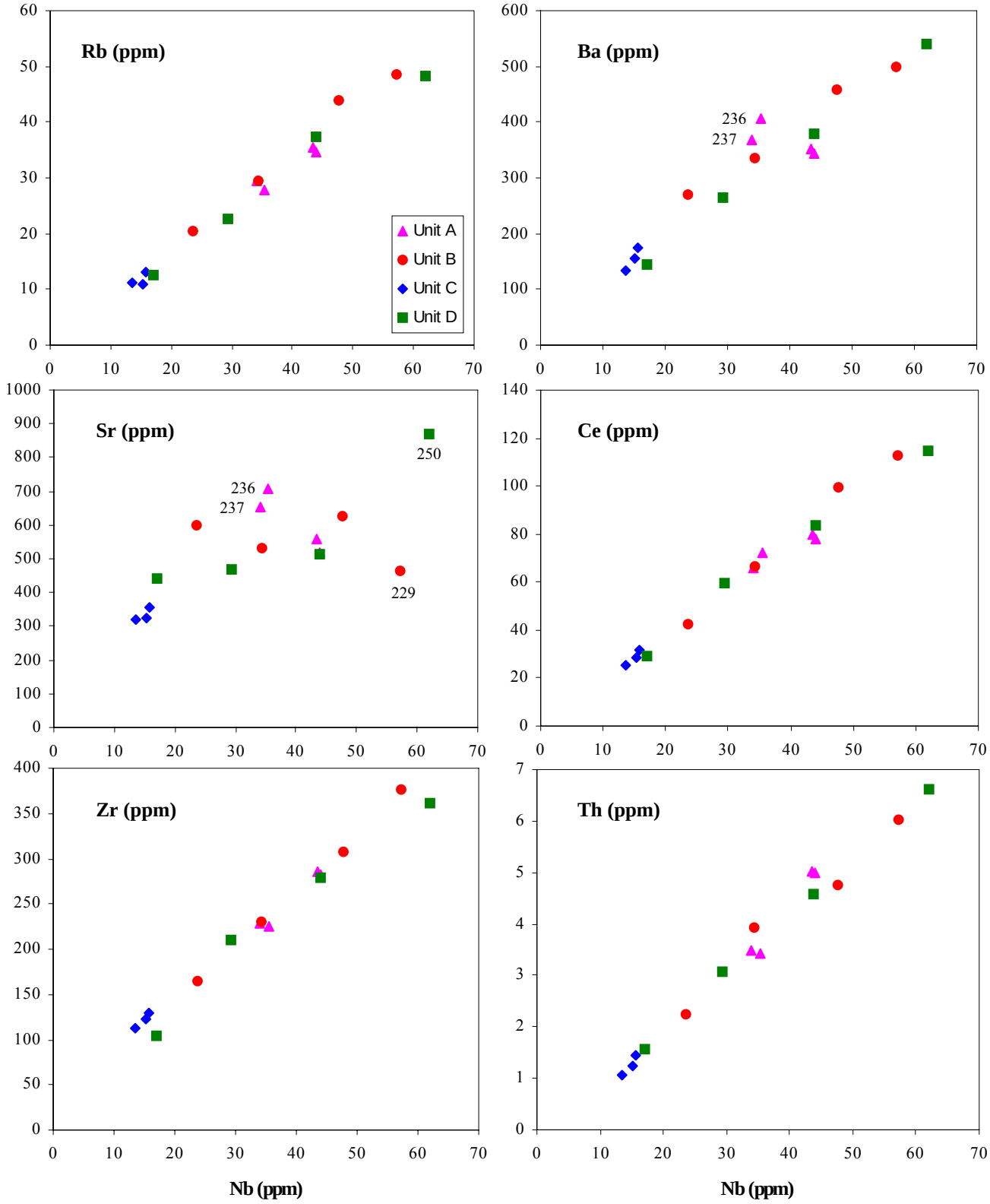

Fig. 4.11. Selection of incompatible elements vs. Nb. Abundances of Rb, Ba, Sr, Ce, Zr, and Th vs. Nb (all in ppm), illustrating the relative incompatibility of these elements in the phenocrystic phases (except Sr).

Elevation plots of Zr/Nb, La/Nb, Th/Ta and $(La/Sm)_N$ vs. MgO illustrate the stratigraphic and temporal variation in incompatible element ratios in the Baie Charrier section (Fig. 4.12). Unit C can be immediately distinguished from the other units, characterized by significantly higher Zr/Nb and La/Sm ratios and lower Th/Ta ratios. Sample 250 of Unit D, identified previously as being plagioclase-rich, is also distinctive, having the lowest Zr/Nb and La/Sm ratios of the section. Note that two of the samples (236 and 237) from Unit A continue to have slightly different chemistry from the other samples in the unit.

Incompatible element abundances were normalized to the primitive mantle estimates of McDonough & Sun (1995) and are plotted in Fig. 4.13a. The rare earth elements (REE) were normalized to the C1 Chondrite values from McDonough & Sun (1995) and are plotted in Fig 4.13b. All of the Baie Charrier samples are enriched in the light rare earth elements. However, the extent to which they concentrate the different incompatible elements varies with each unit. The samples with the highest MgO contents of the section, including the high-MgO basalts of Unit C and the picrite from Unit D, have the lowest abundances of incompatible elements, reflecting a dilution effect from accumulated olivine, which does not incorporate incompatible elements. Units B and D encompass a wide range of incompatible element abundances, with the plagioclase-rich sample (250, Unit D) having the highest abundances of the section. Unit A has moderate abundances; note that samples 236 and 237 are shifted to slightly lower abundances relative to the other two samples in this unit.

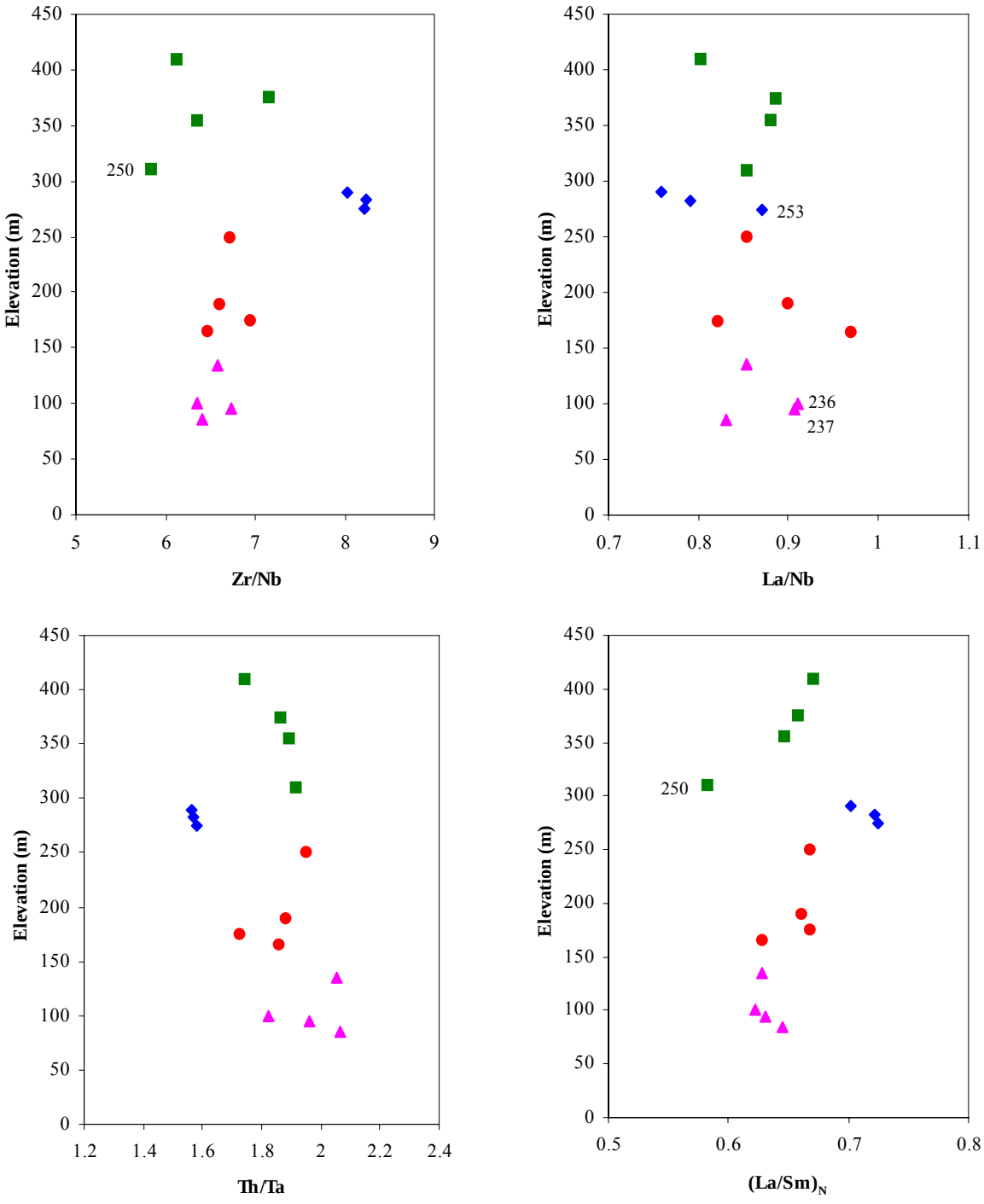

Fig. 4.12. Stratigraphic and temporal variation in incompatible element ratios. Zr/Nb, La/Nb, Th/Ta, and $(La/Sm)_N$ vs. elevation (in metres), where $(La/Sm)_N$ is the chondrite-normalized ratio using the C1 chondrite normalizing values of McDonough & Sun (1995).

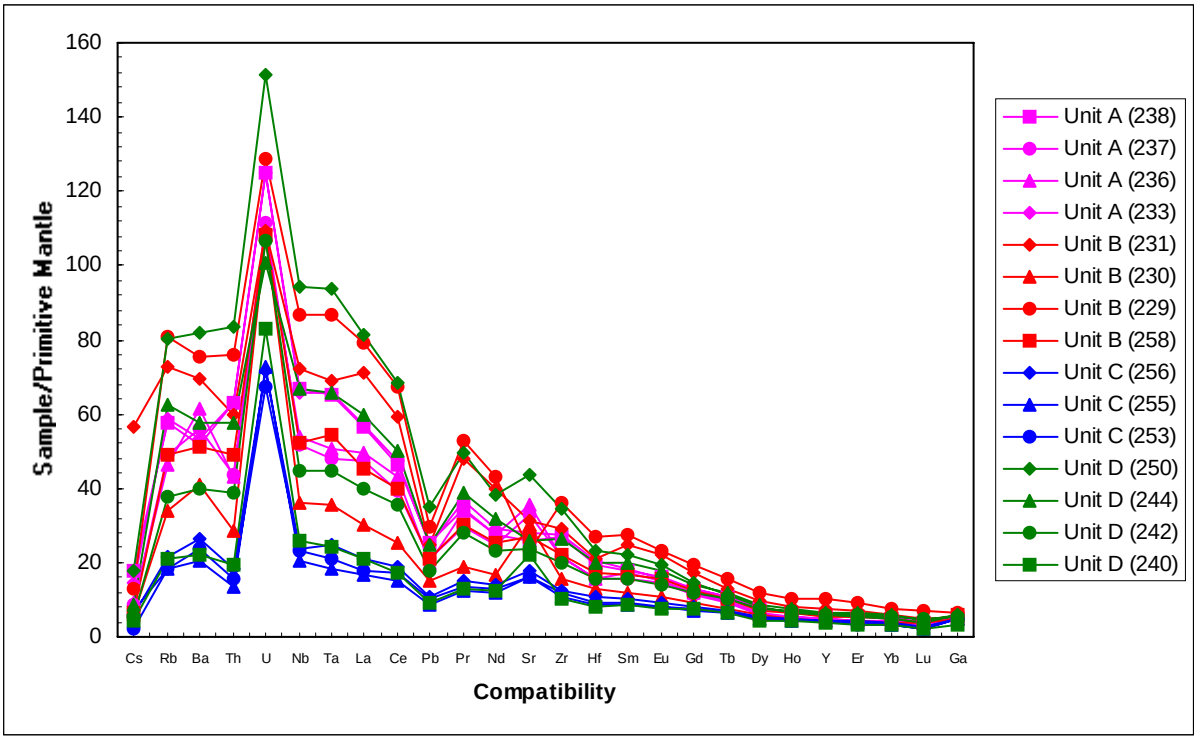

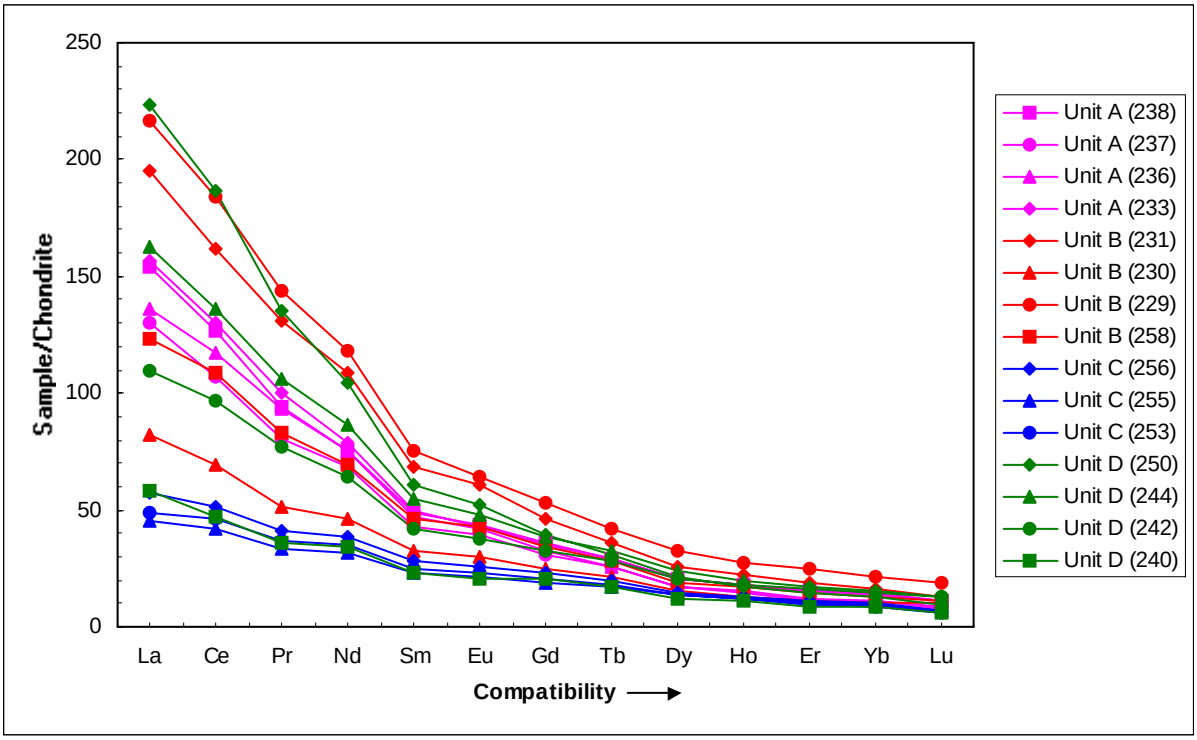

Fig. 4.13. Incompatible element abundances of the Baie Charrier samples. Normalized to (a) the primitive mantle estimates of McDonough & Sun (1995) and (b) the C1 Chondrite values of McDonough & Sun (1995). Note that the y-axis scale is linear, not logarithmic, to emphasize the differences between individual samples.

4.6 Sr-Nd-Pb Isotopes

Elevation plots of measured $^{143}Nd/^{144}Nd$ and $^{87}Sr/^{86}Sr$ demonstrate the isotopic variability of the Baie Charrier section (Fig. 4.14). Units A, B, and D have relatively similar $^{143}Nd/^{144}Nd$. Sample 250 of Unit D, however, has a significantly lower ratio than the rest of the unit. The three Unit C samples are characterized by the highest $^{143}Nd/^{144}Nd$ values of the section. The two Unit A samples have $^{87}Sr/^{86}Sr$ values that are within error of each other. Unit B has lower values of $^{87}Sr/^{86}Sr$ than Unit A, with the exception of sample 229, which has a higher value. The three Unit C samples have the lowest $^{87}Sr/^{86}Sr$ values of the section, with the exception of sample 253, which has a significantly higher $^{87}Sr/^{86}Sr$ value. The Unit D samples have relatively similar $^{87}Sr/^{86}Sr$.

Plots of measured Pb isotopic compositions vs. elevation show considerable variability within the Baie Charrier section (Fig. 4.15). Unit C is characterized by significantly lower Pb isotopic compositions, except for sample 255, which has a higher $^{206}Pb/^{204}Pb$ ratio. Unit D consistently has the highest Pb isotopic ratios of the section.

On Pb-Pb isotopic diagrams (Fig. 4.16) the Baie Charrier samples fall along positive linear trends. Sample 255 from Unit C, however, does not fall along either of the trendlines. On a Sr-Nd isotopic diagram (Fig. 4.17), the majority of the Baie Charrier samples define a relatively small field. Note that the two samples from Unit A and sample 229 from Unit B all plot at the same point. There are three samples that appear to be slightly unusual; two from Unit C (255 and 256) have higher $^{143}Nd/^{144}Nd$ and lower $^{87}Sr/^{86}Sr$, while sample 250 from Unit D has lower $^{143}Nd/^{144}Nd$. On a Pb-Sr isotopic diagram (Fig. 4.18), the Baie Charrier samples define a linear array range of $^{206}Pb/^{204}Pb$ between ~18.35 and ~18.65. However, samples 253 and 256 from Unit C are significantly less radiogenic, with $^{206}Pb/^{204}Pb$ = ~18.2.

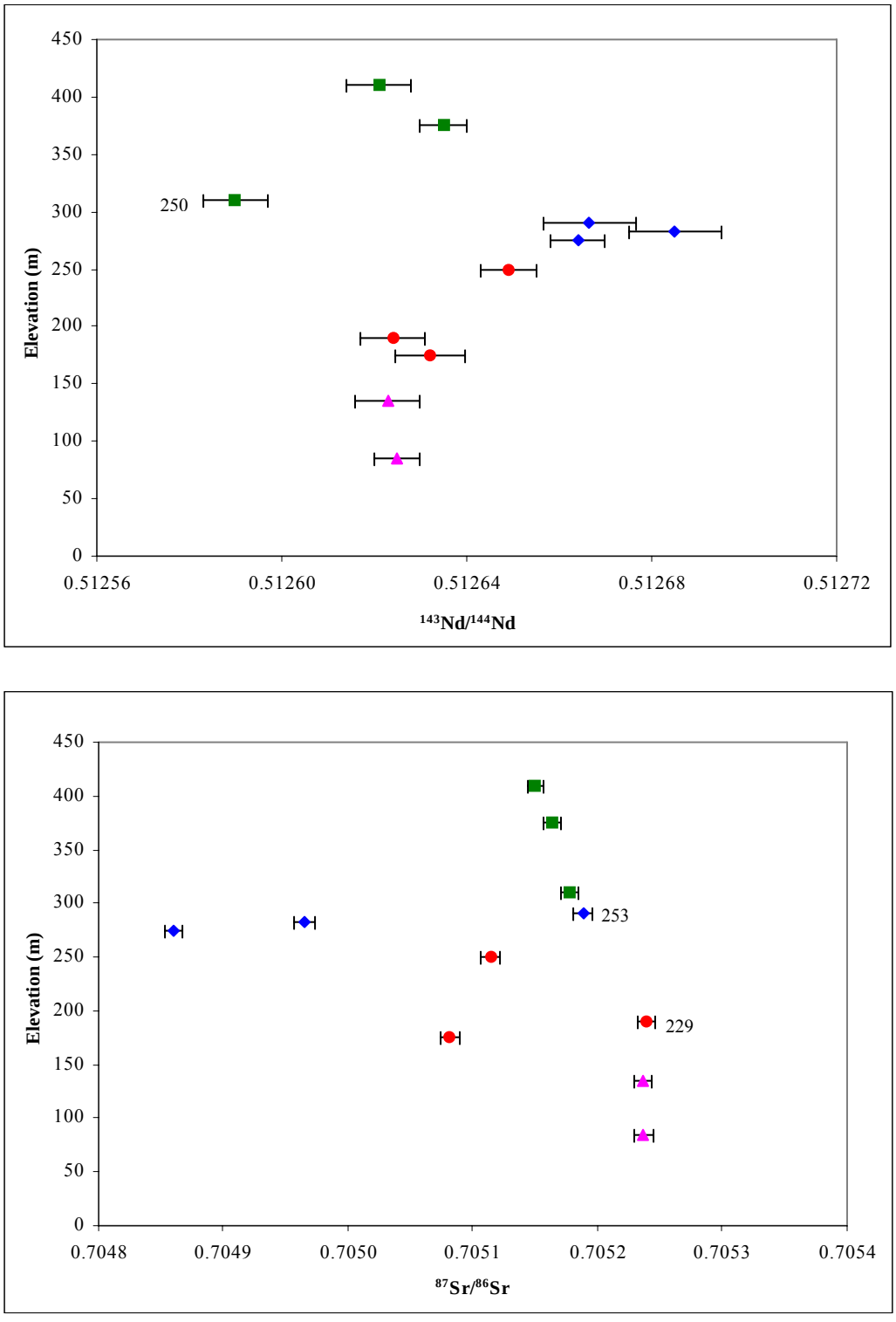

Fig. 4.14. Stratigraphic variation in Nd and Sr isotopic ratios. (a) $^{143}Nd/^{144}Nd$ vs. elevation (in metres) and (b) $^{87}Sr/^{86}Sr$ vs. elevation (in metres). The error bars correspond to $2s_m$ of the individual samples.

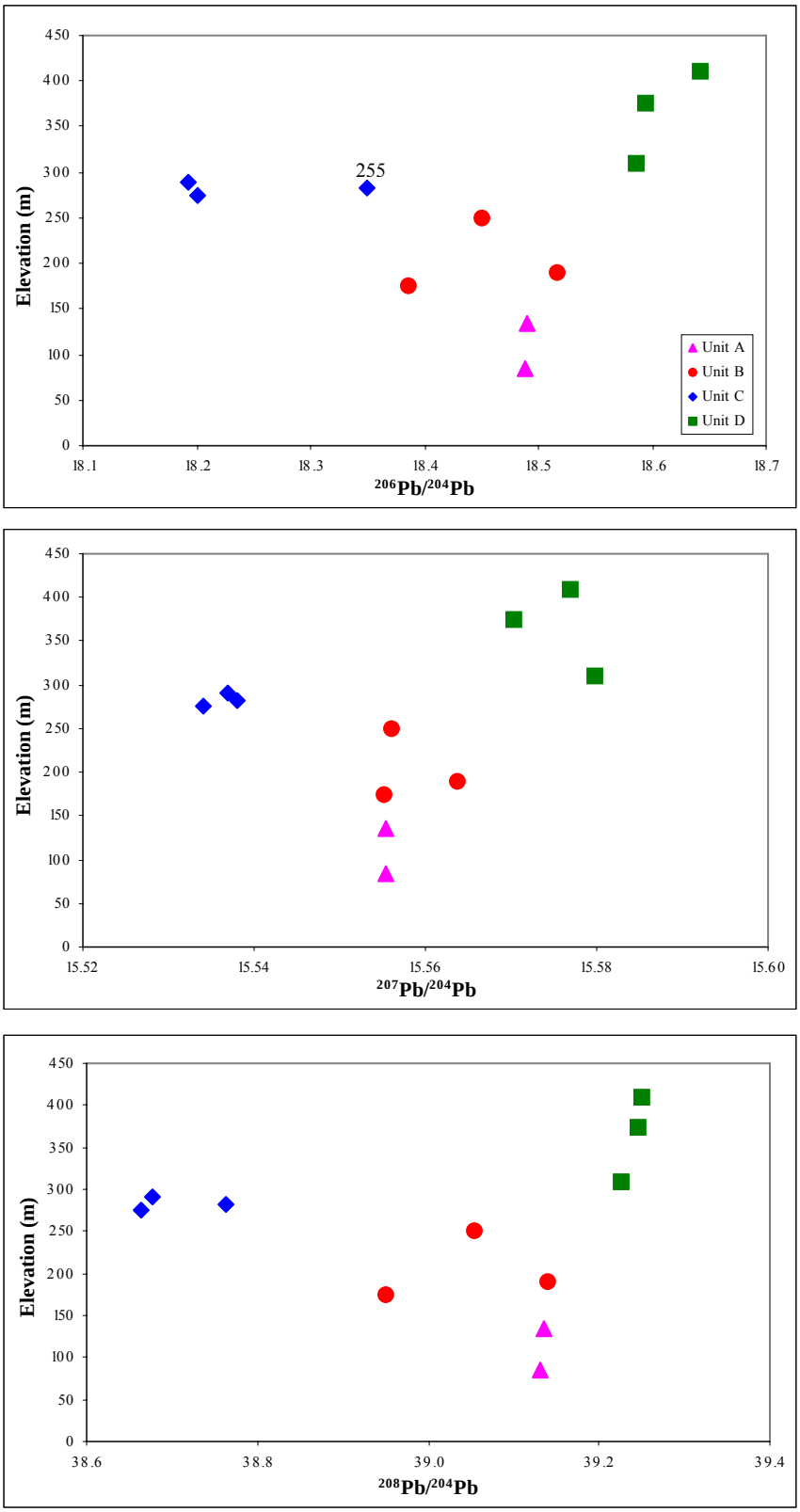

Fig. 4.15. *Stratigraphic variation in Pb isotopic ratios. (a) $^{206}Pb/^{204}Pb$, (b) $^{207}Pb/^{204}Pb$, and (c) $^{208}Pb/^{204}Pb$ vs. elevation (in metres). Note the distinctive Pb isotopic compositions of Unit C, and the higher $^{206}Pb/^{204}Pb$ of sample 255. The 2s $_m$ is smaller than the symbol size.*

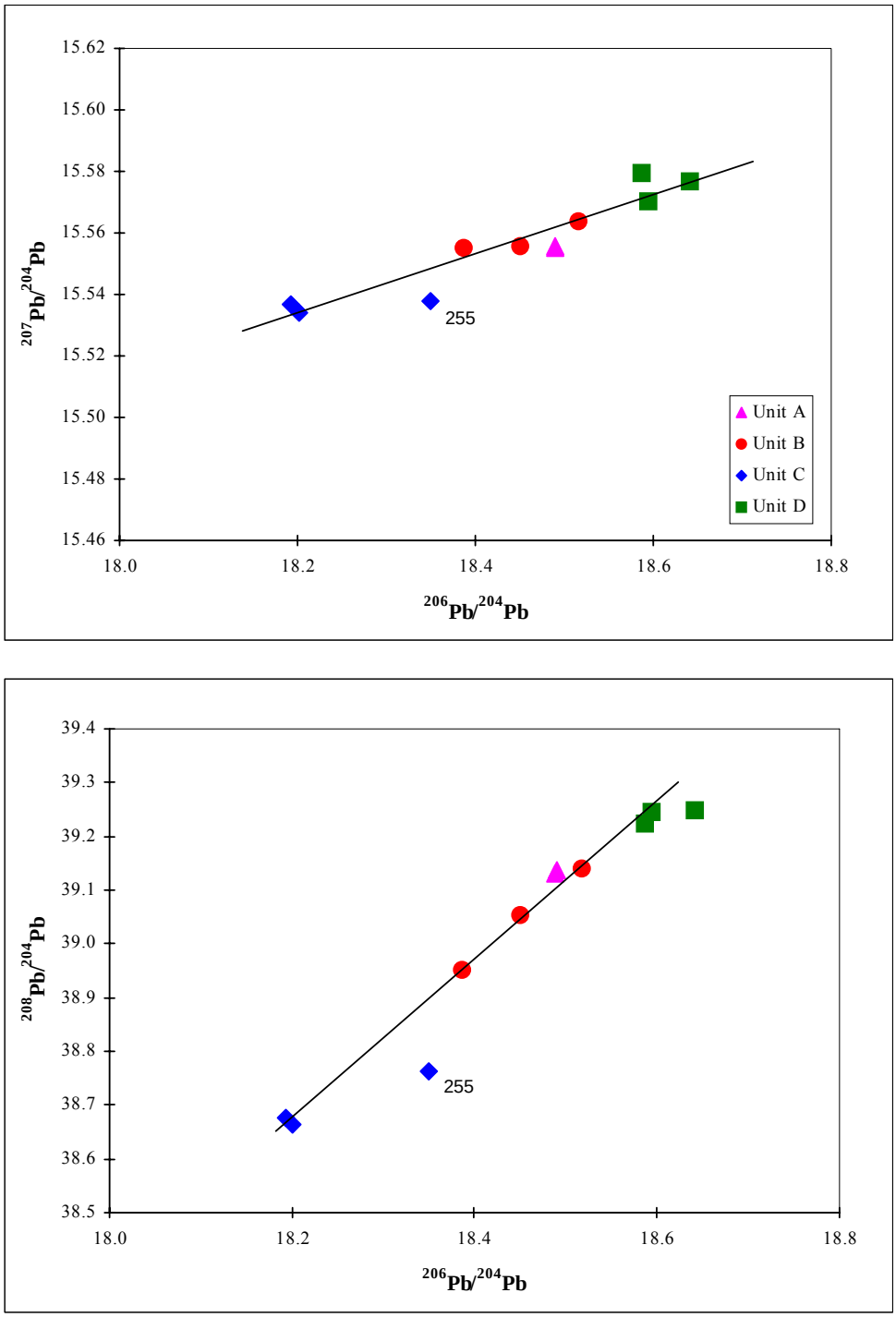

Fig. 4.16. Pb-Pb isotopic diagrams. (a) Measured $^{207}Pb/^{204}Pb$ vs. $^{206}Pb/^{204}Pb$. (b) Measured $^{208}Pb/^{204}Pb$ vs. $^{206}Pb/^{204}Pb$. Note sample 255, which does not fall along either of the trendlines. The $2\sigma_m$ is smaller than the symbol size.

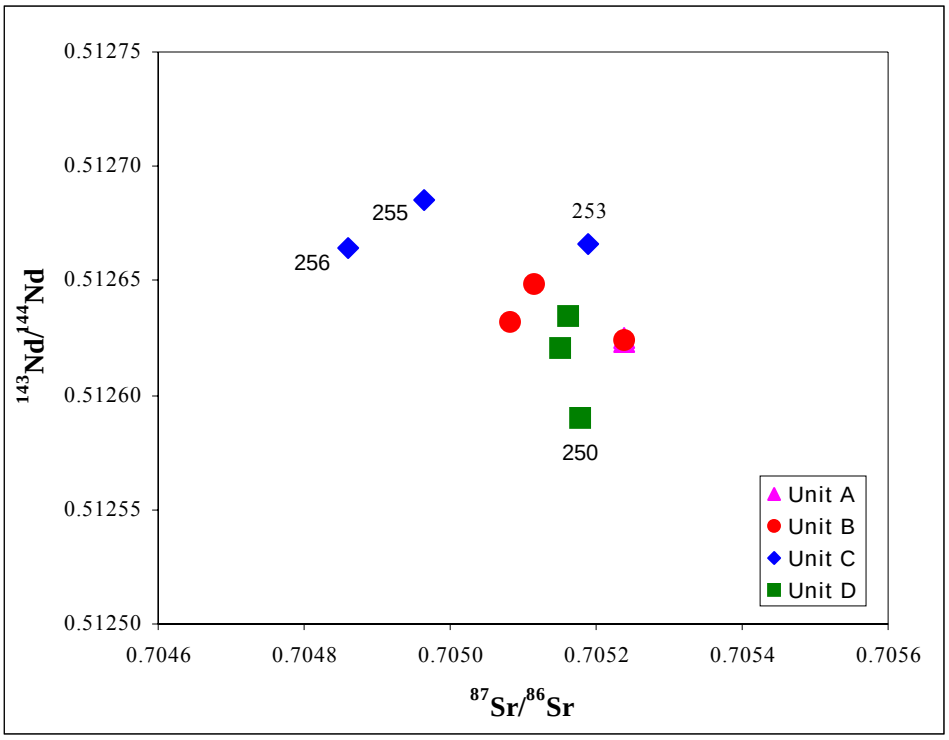

Fig. 4.17. Nd-Sr isotopic diagram. Measured $^{143}Nd/^{144}Nd$ vs. $^{87}Sr/^{86}Sr$. Note the distinctive Unit C samples and sample 250. The $2\sigma_m$ is smaller than the symbol size.

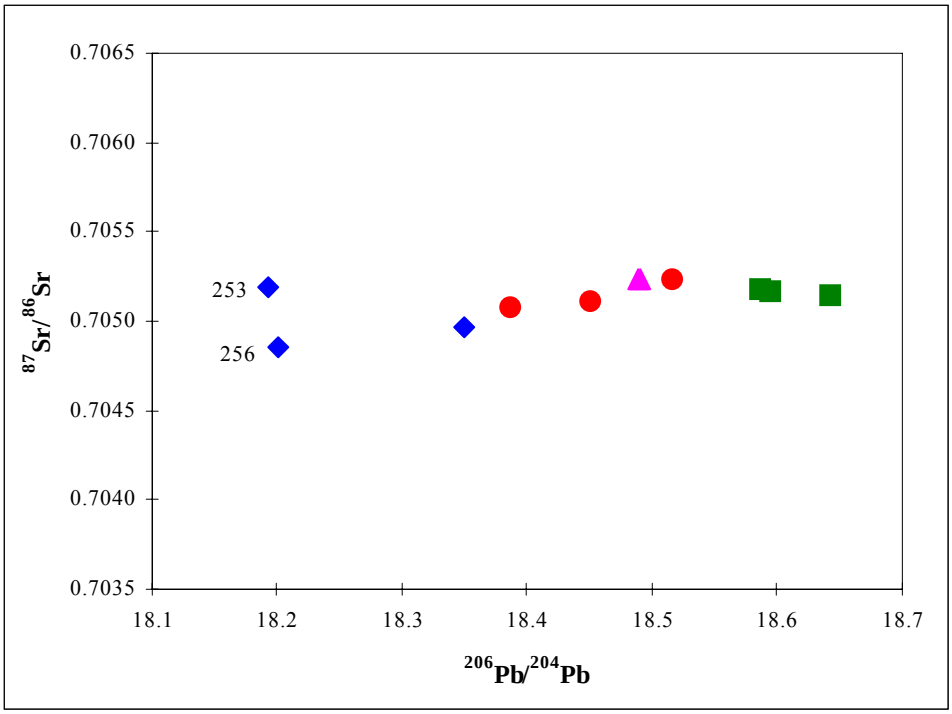

Fig. 4.18. Sr-Pb isotopic diagram. Measured $^{87}Sr/^{86}Sr$ vs. $^{206}Pb/^{204}Pb$. Note the two samples from Unit C, which are significantly less radiogenic. The $2\sigma_m$ is smaller than the symbol size.

5.1 Temporal Variation in the Baie Charrier Section

The Baie Charrier section preserves a 325 m series of basaltic flows, which represent a temporal record of volcanism from the Kerguelen mantle plume. With increasing elevation, these flows may be used to define geochemical variations with time. Ar-Ar dating of whole rocks from the tops and bottoms of 24-29 Ma basaltic sections across the Kerguelen Archipelago, with stratigraphic thicknesses from 400-1000 m, shows them to be the same within error (Nicolaysen *et al*., 2000). Estimated lava accumulation rates are ~1.6 $\pm$ 0.9 km/my (Nicolaysen *et al*., 2000) suggesting that a 300 m section of basalts such as at Baie Charrier would be formed in approximately 200,000 years.

The Baie Charrier section can be subdivided into four stratigraphic units that possess distinctive petrographic, geochemical, and isotopic characteristics (Fig. 4.1). The units alternate between the high-MgO olivine-phyric basalts of Units A and C, and the low-MgO plagioclase-phyric mildly alkalic basalts of Units B and D. The basal Unit A can also be defined by a significant enrichment in incompatible elements. The intermediate Unit C is characterised by unusually high ratios of Zr/Nb, and $(La/Sm)_N$ (chondrite-normalized) and low ratios of Th/Ta. As well, Unit C generally exhibits high $^{143}Nd/^{144}Nd$, low $^{87}Sr/^{86}Sr$, and less radiogenic Pb isotopic compositions. The observed differences in ratios of incompatible elements and isotopic compositions are of particular significance. In an intra-oceanic setting (i.e. no continental crust), the only way to alter these geochemical characteristics is to change a variable in the source region. These differences therefore may reflect either a change in the extent of partial melting (trace element differences) or in the composition of the source region (isotopic differences). What is of particular significance is the scale over which these differences are observed.

Unit C, for example, is only 35 m thick, suggesting very small-scale variability and heterogeneity in the source region of these lavas.

5.2 Mineral-Melt Equilibria

An important objective of this study, as well as for other studies of Kerguelen Archipelago basalts, was to determine if the phenocrysts are in equilibrium with their host rock. In other words, do the bulk compositions of these basaltic rocks represent liquids? To answer this question, the whole rock Mg# was plotted against the forsterite content for olivine (Fig. 5.1) and the Mg# for clinopyroxene (Fig. 5.2). The Fe/Mg exchange partition coefficients between olivine and basaltic liquid and between clinopyroxene and basaltic liquid have been constrained experimentally. Values of 0.30 $\pm$ 0.03 (Roeder & Emslie, 1970) for olivine and 0.23 $\pm$ 0.05 (Grove & Bryan, 1983; Toplis & Carroll, 1995) for clinopyroxene appear to be consistent. The equilibrium fields for Fe/Mg exchange between these minerals and basaltic melt are shown on Figures 5.1 and 5.2. Compositions that fall above this field are interpreted to have inherited 'exotic' crystals, or xenocrysts. Compositions that are shifted to higher whole-rock Mg#'s, and therefore fall below the equilibrium field, are interpreted to have experienced olivine or clinopyroxene accumulation. Rim compositions that are pulled towards lower forsterite content or $Mg\#_{cpx}$ reflect diffusion of Mg and Fe as the crystal grew and interacted with the remaining melt in the groundmass.

The majority of the olivine phenocrysts in the Baie Charrier basalts fall within the equilibrium field, and are thus interpreted to be in equilibrium with their host rock. However, the forsterite-rich cores of samples 258 (Unit B) and 233 (Unit A) plot slightly above the equilibrium field, perhaps reflecting the addition of small amounts of

(a)

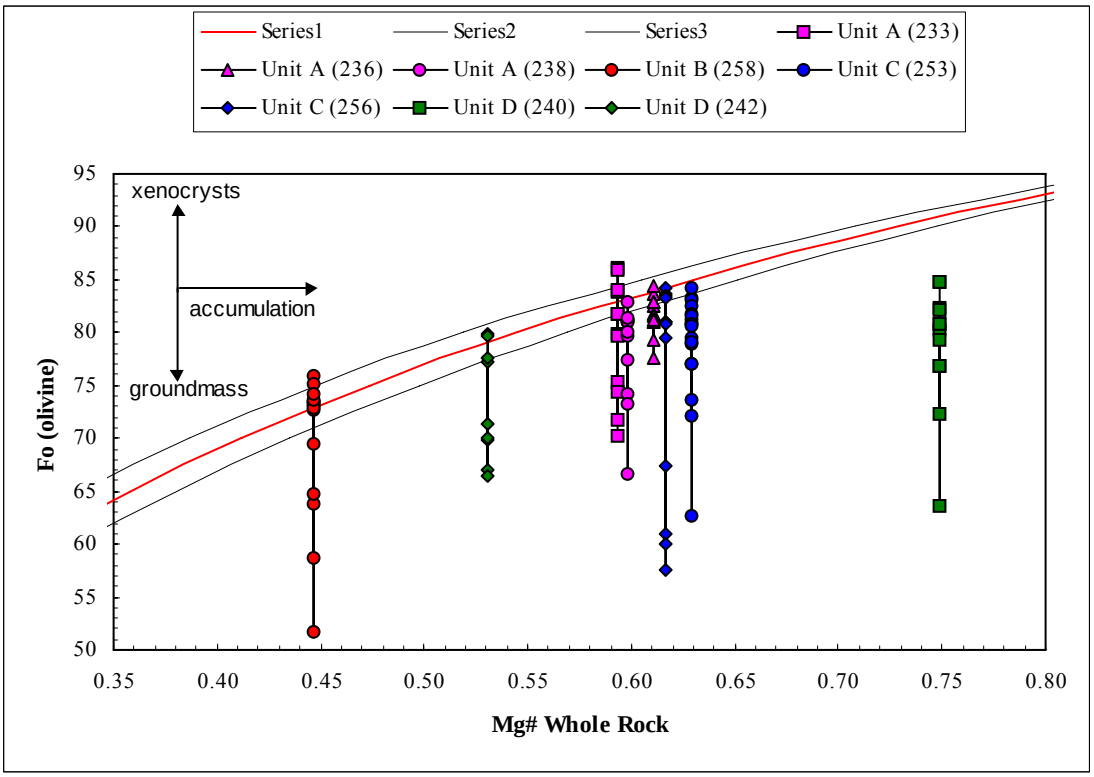

(b)

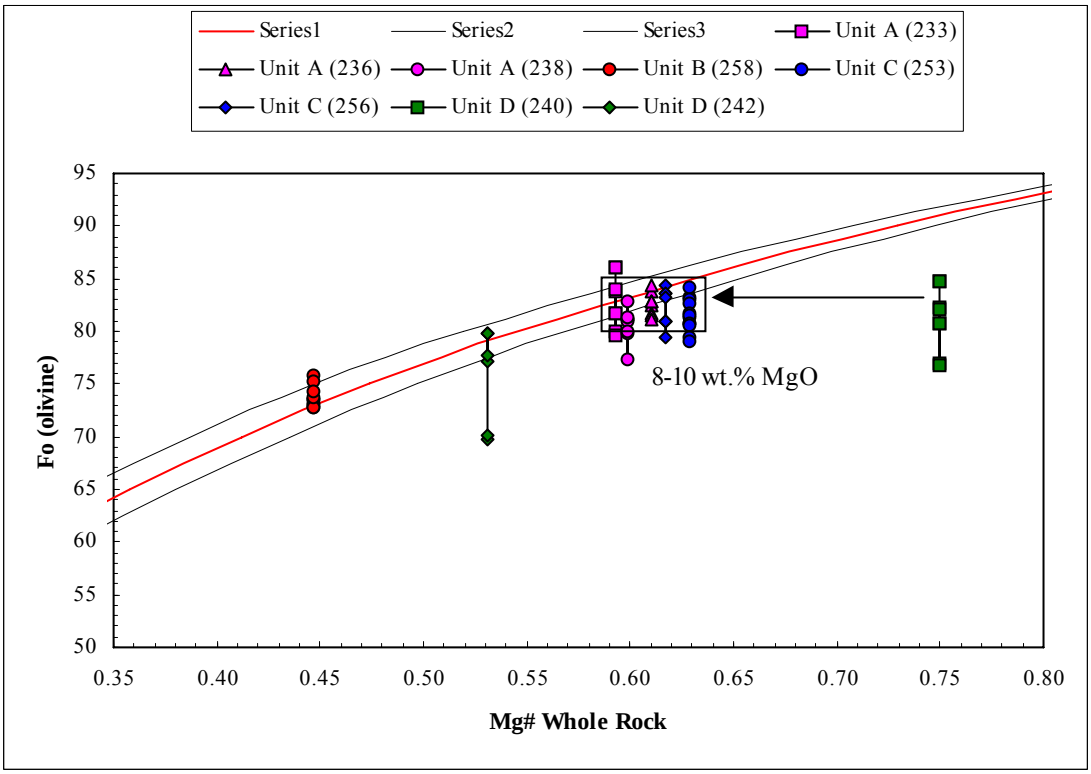

Fig. 5.1. Mineral-melt equilibrium diagrams for olivine. Whole rock Mg-number vs. forsterite content of olivine. (a) Rim and core compositions. (b) Core compositions only. Curves represent the equilibrium fields for Fe/Mg exchange between olivine and basaltic melt (Roeder & Emslie, 1970). (See text for details).

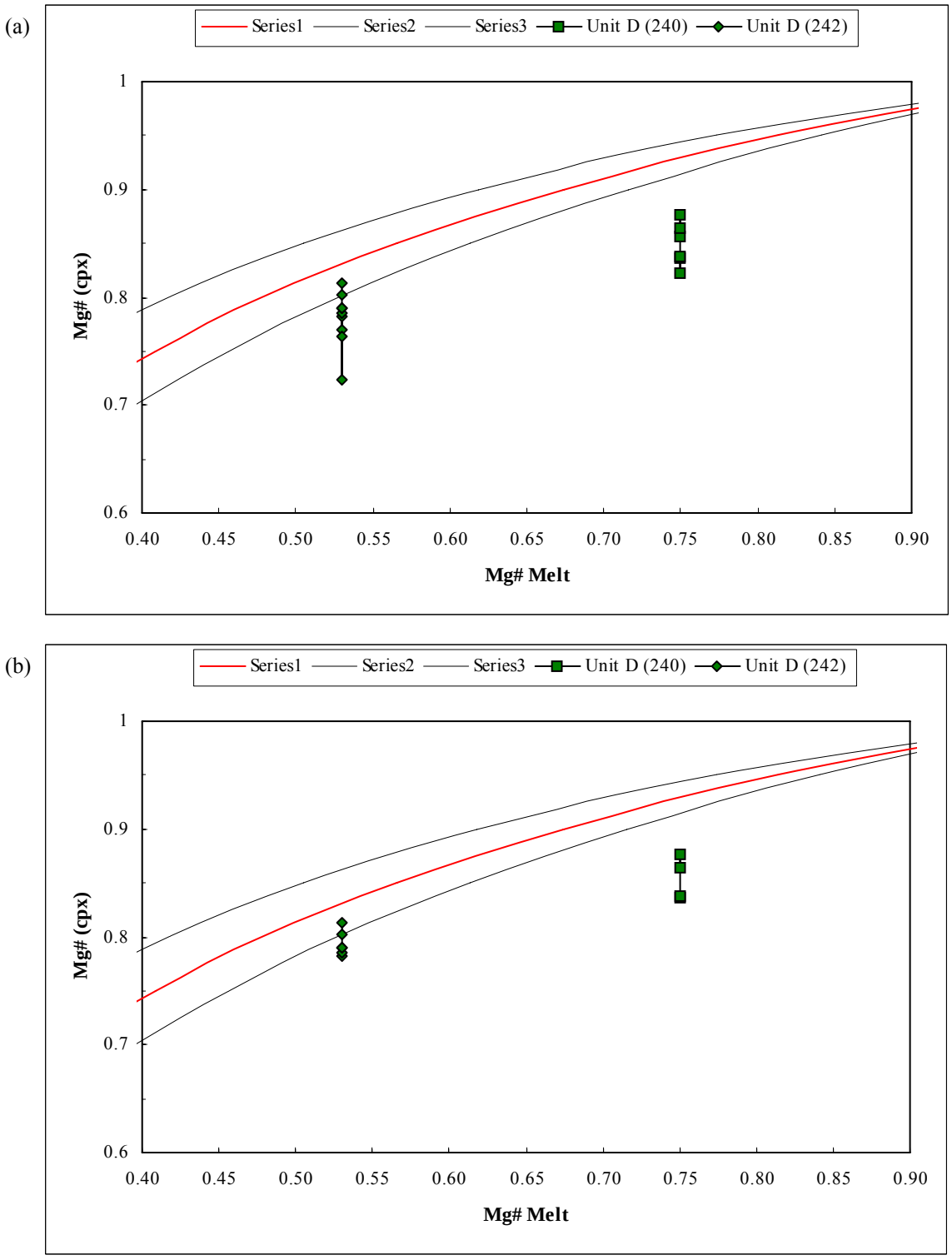

Fig. 5.2. Mineral-melt equilibrium diagrams for clinopyroxene. Whole rock Mg-number vs. clinopyroxene Mg-number. (a) Rim and core compositions. (b) Core compositions only. Curves represent the equilibrium fields for Fe/Mg exchange between clinopyroxene and basaltic melt (Grove & Bryan, 1983; Toplis & Carroll, 1995). (See text for details).

xenocrystic olivine. Sample 240 (Unit D) plots well below the equilibrium field at high whole rock Mg#, suggesting that this sample has accumulated significant amounts of olivine. If olivine were to be removed from this rock, the composition would track back to the cluster of samples that have Mg#'s ranging from 0.59 to 0.63, corresponding to MgO content between 8-10 wt.%. Interestingly, Doucet *et al*. (2002) also determined that the most MgO-rich lava from the Ruches and Fontaine sections of the Kerguelen Archipelago were also between 8-10 wt.% MgO. This suggests that 10 wt.% MgO may be the maximum MgO content for magmas without accumulated phenocrysts on the Kerguelen Archipelago.

The two Baie Charrier samples analysed for clinopyroxene phenocryst compositions are both from Unit D. Sample 242 plots just within the equilibrium field, indicating that the clinopyroxene phenocrysts are in equilibrium with the whole rock, along with the olivines. Sample 240 plots below the equilibrium field, again at high whole rock Mg#, consistent with the accumulation of both clinopyroxene and olivine.

5.3 Comparison Between the Baie Charrier and Mt. Crozier Sections on the Courbet Peninsula

The Baie Charrier section can be compared to the Mt. Crozier section, on the Courbet Peninsula, and sections from the Southeast Province, which are composed of mildly alkalic 24-25 Ma basalts (Fig. 2.2). The motivation for comparing Baie Charrier with Mt. Crozier is to determine if the Courbet Peninsula is a single volcanic unit, as proposed by Nougier (1970). The petrography of the lavas in the two sections is markedly different. The Crozier lavas, in the center of the Courbet Peninsula, are characterized by the absence of olivine-phyric basalts (Damasceno *et al.*, 2002), while all

of the Baie Charrier basalts are olivine-phyric to some degree. Correspondingly, the MgO contents between the two sections are very different (Fig 5.3). The average value for the Crozier section is ~4 wt.% MgO, whereas the average for the Baie Charrier section is significantly higher at ~7.5 wt.% MgO. All of the Crozier lavas have <8 wt.% MgO, while many of the Baie Charrier basalts have MgO >8 wt.% and can reach over 16 wt.% (in the picrite, sample 240, Unit D). This relationship is important, since a greater eruptive flux is typically required for lavas rich in olivine phenocrysts due to their greater density (Murata & Richter, 1966). The lack of olivine-phyric basalts in the Mt. Crozier section relative to the Baie Charrier section suggests that the eruptive center of the higher magma flux lavas from the Courbet Peninsula may not correspond to the geographic center of the glacially eroded peninsula.

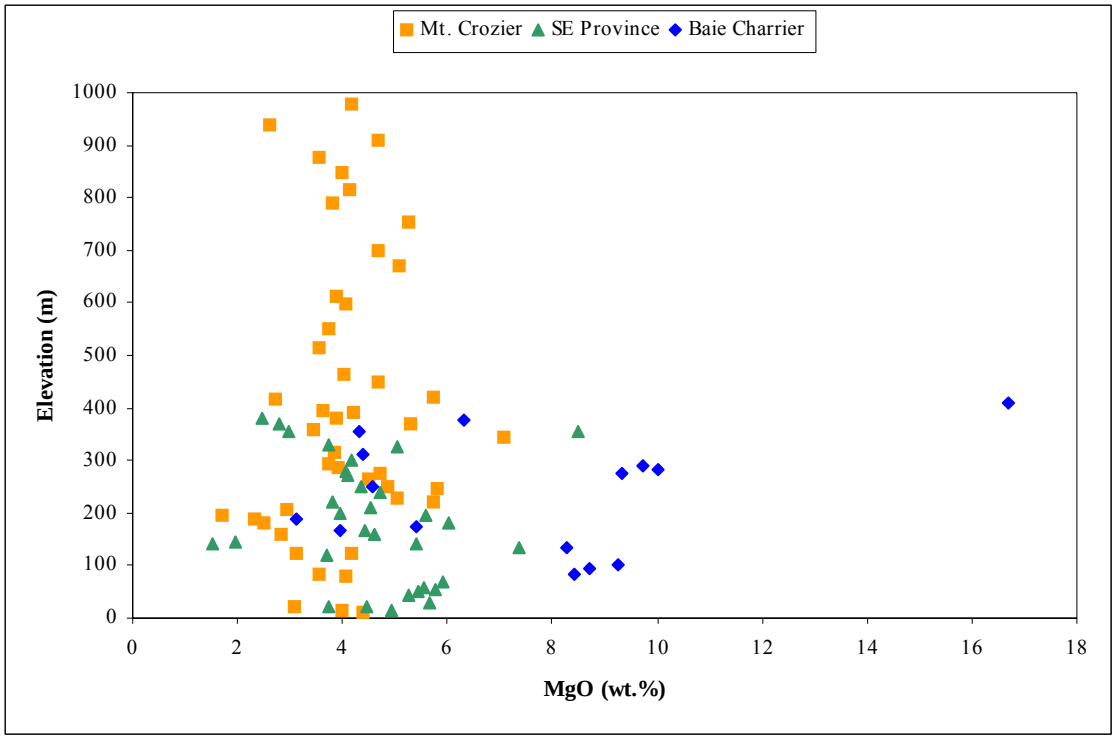

Fig. 5.3. MgO content comparison between Baie Charrier, Mt. Crozier, and the Southeast Province. MgO (wt.%) vs. elevation (m). Note that the Baie Charrier basalts are significantly more MgO-rich.

Trace element and isotopic compositions are similar between the Baie Charrier and Mt. Crozier sections. The Zr/Nb ratios are comparable between the two sections (Fig. 5.4). The majority of the samples in both sections plot in a limited range between 6-7.5, while the anomalous samples have higher values of between ~7.5 and ~9. Values in each of the sections are consistent with the temporal variation in Zr/Nb observed in lavas associated with the Kerguelen mantle plume, where lavas <30 Ma typically have Zr/Nb <10 (Weis *et al.*, 2002).

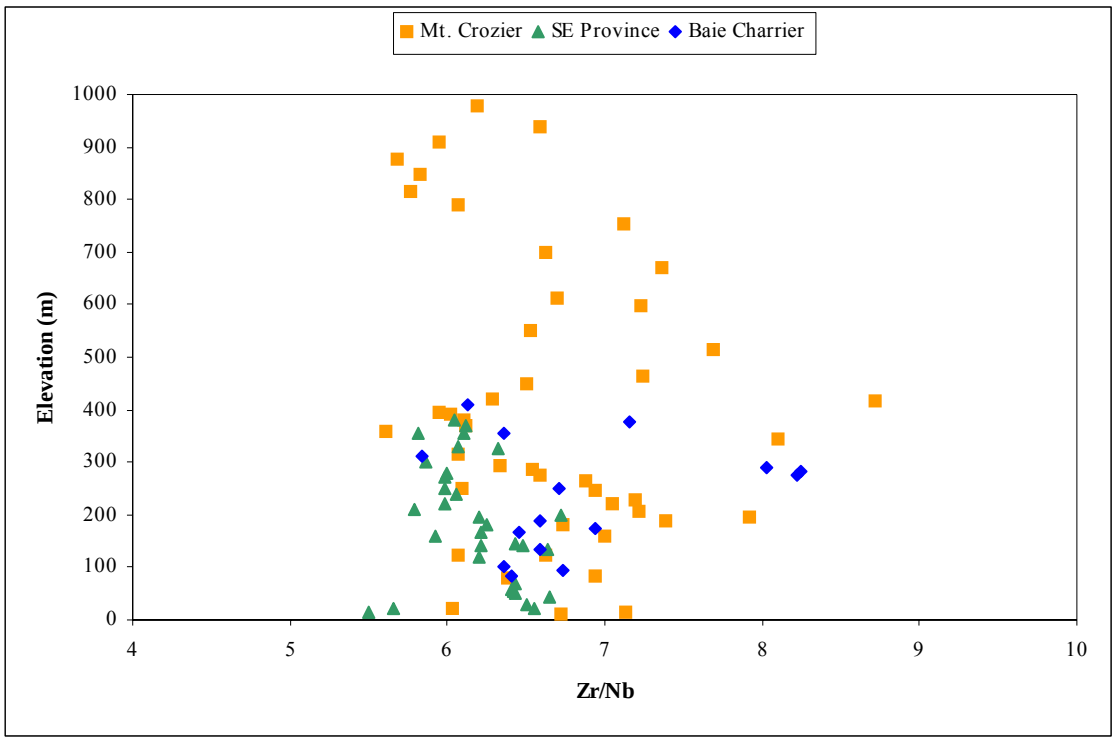

Fig. 5.4. Zr/Nb comparison between Baie Charrier, Mt. Crozier, and the Southeast Province. The majority of the samples in all sections plot between 6-7.5.

When comparing the primitive mantle-normalized incompatible element abundances of the two sections, the general trend is similar, with relatively large abundances of the most incompatible elements, and a relative enrichment in the light rare earth elements (Fig. 5.5).

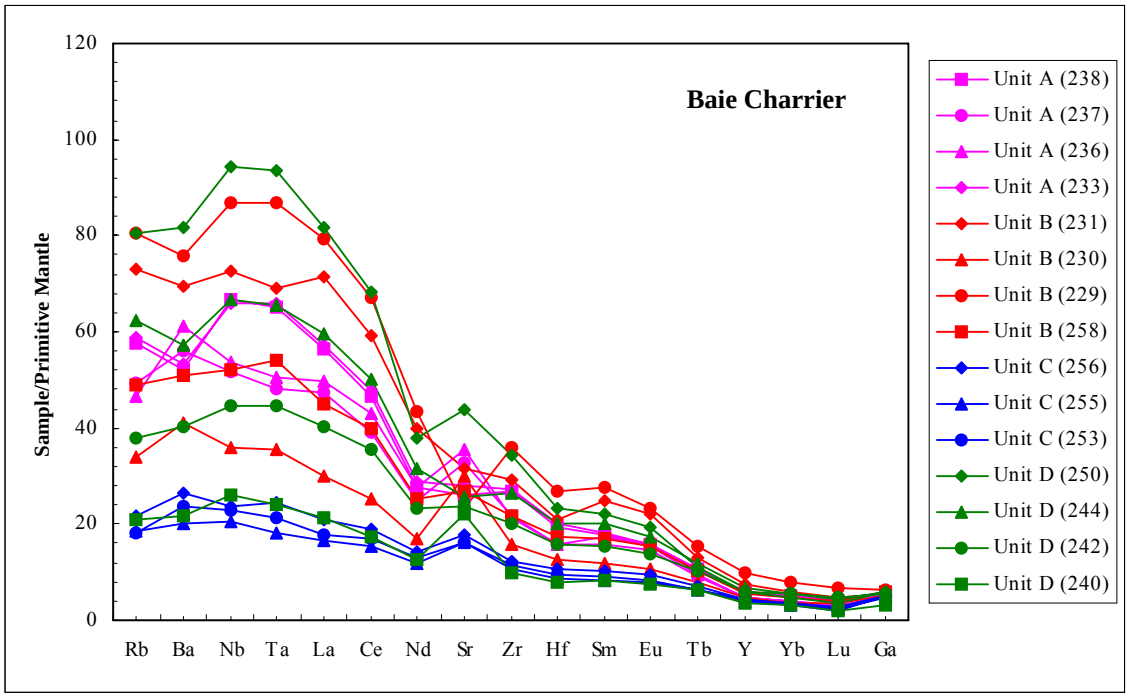

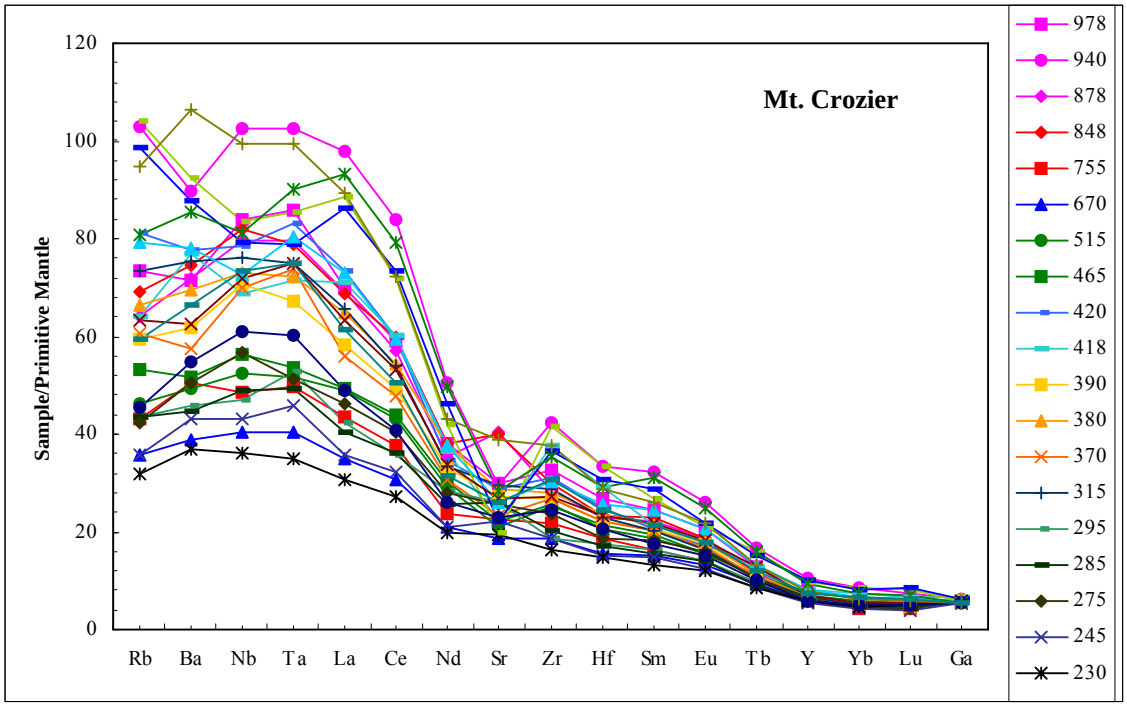

Fig. 5.5. Comparison of incompatible element abundances between the Baie Charrier and Mt. Crozier sections. Normalized to the primitive mantle estimates of McDonough & Sun (1995). Note that data for some elements was not available for the Mt. Crozier section, and have been removed from the Baie Charrier plot to allow for easier comparison.

When comparing the isotopic systematics of Baie Charrier and Mt. Crozier, the two sections are also quite similar. On a Nd-Sr isotope diagram (Fig. 5.6), there is considerable overlap between the samples of both sections. Two of the high-MgO samples from Unit C in the Baie Charrier section are drawn up to higher $^{143}Nd/^{144}Nd$ and lower $^{87}Sr/^{86}Sr$, as is one of the Mt. Crozier samples. Sample 250 (Unit D) has a lower $^{143}Nd/^{144}Nd$ for a given $^{87}Sr/^{86}Sr$ compared to the other samples. This same trend is observed in the Mt. Crozier samples. On a Sr-Pb isotope diagram (Fig. 5.7), the Baie Charrier samples overlap with the Mt. Crozier samples, which have the most radiogenic Pb isotopic compositions of basalts on the Kerguelen Archipelago. Two high-MgO samples from Baie Charrier (253 and 256) have relatively low $^{206}Pb/^{204}Pb$, which is not observed at Mt. Crozier. On Pb-Pb isotope diagrams (Fig 5.8), the Baie Charrier samples again overlap the Mt. Crozier samples. Linear trendlines to both data sets are very similar. The consistent trace element and isotopic data is compelling evidence that both Baie Charrier and Mt. Crozier are derived from the same source. By inference, this also supports the theory proposed by Nougier (1970), that the Courbet Peninsula represents a single volcanic unit.

5.4 Constraints on the Source Composition of the Kerguelen Mantle Plume

On a Sr-Nd isotope diagram, volcanism associated with the Kerguelen mantle plume plots on a negative linear trend (Fig. 5.9). The Southeast Indian Ridge (SEIR) represents a depleted mid-ocean ridge basalt (MORB) component, and originates from a source depleted in incompatible elements due to repeated melting of the mantle. Site 1140 basalts on the Northern Kerguelen Plateau present an strong mixing relationship between depleted material from the SEIR and the Kerguelen plume, which is coherent

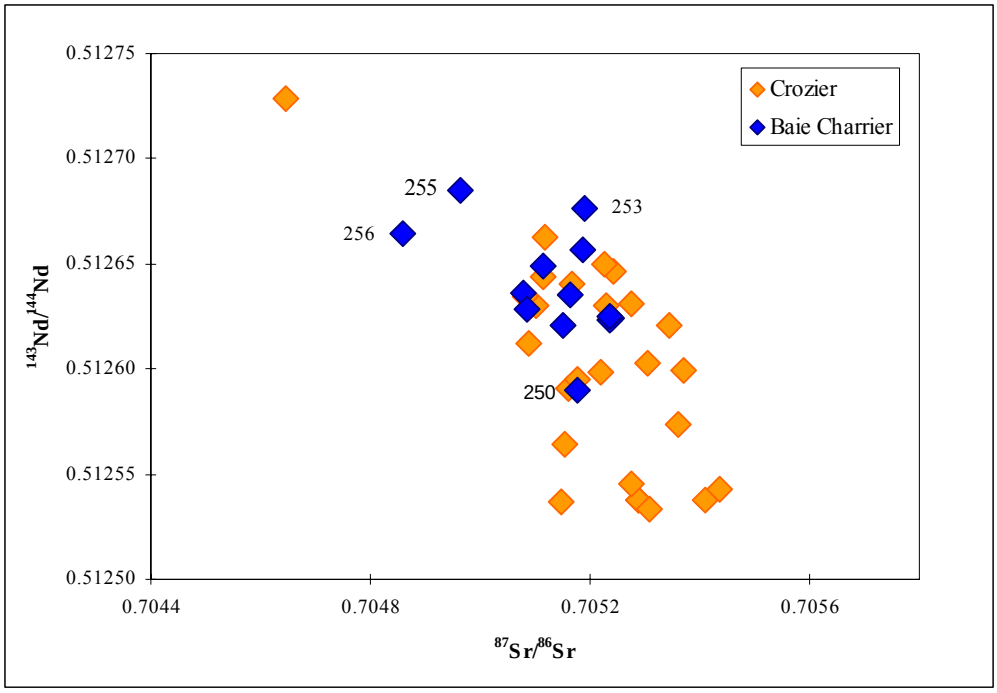

Fig. 5.6. Nd-Sr isotopic diagram showing comparison between the Baie Charrier and Mt. Crozier sections. Baie Charrier samples overlap with the Mt. Crozier samples, except for the three high-MgO samples (253, 255, 253) from Unit C. The $2\sigma_m$ is smaller than the symbol size.

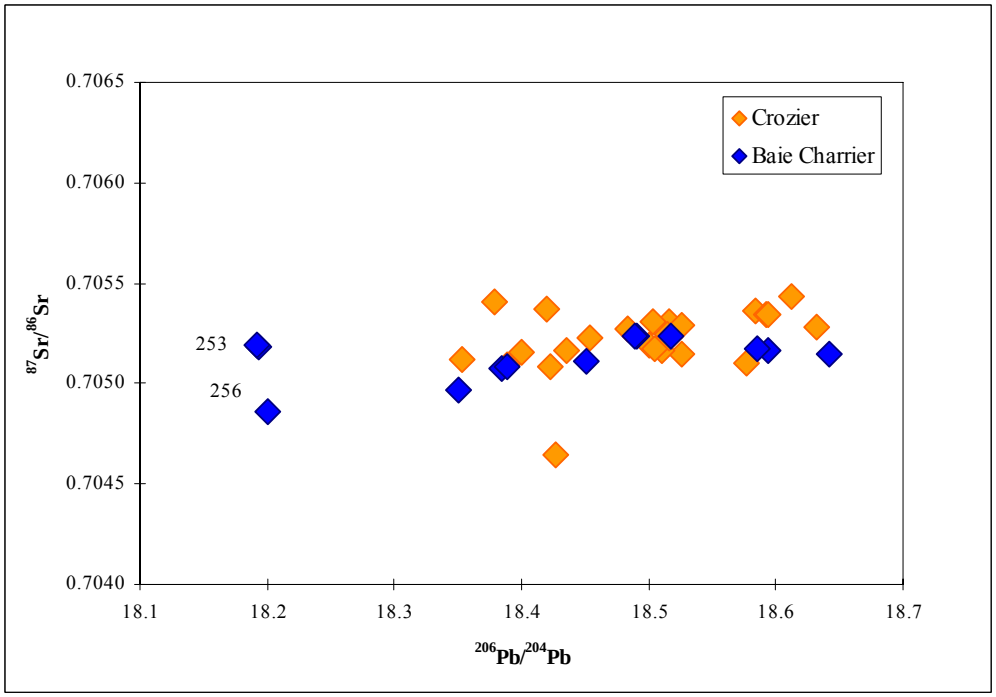

Fig. 5.7. Sr-Pb isotopic diagram showingcomparison between the Baie Charrier and Mt. Crozier sections. Baie Charrier samples overlap with the Mt. Crozier samples, except for two of the high-MgO samples (253 and 256) from Unit C. The $2\sigma_m$ is smaller than the symbol size.

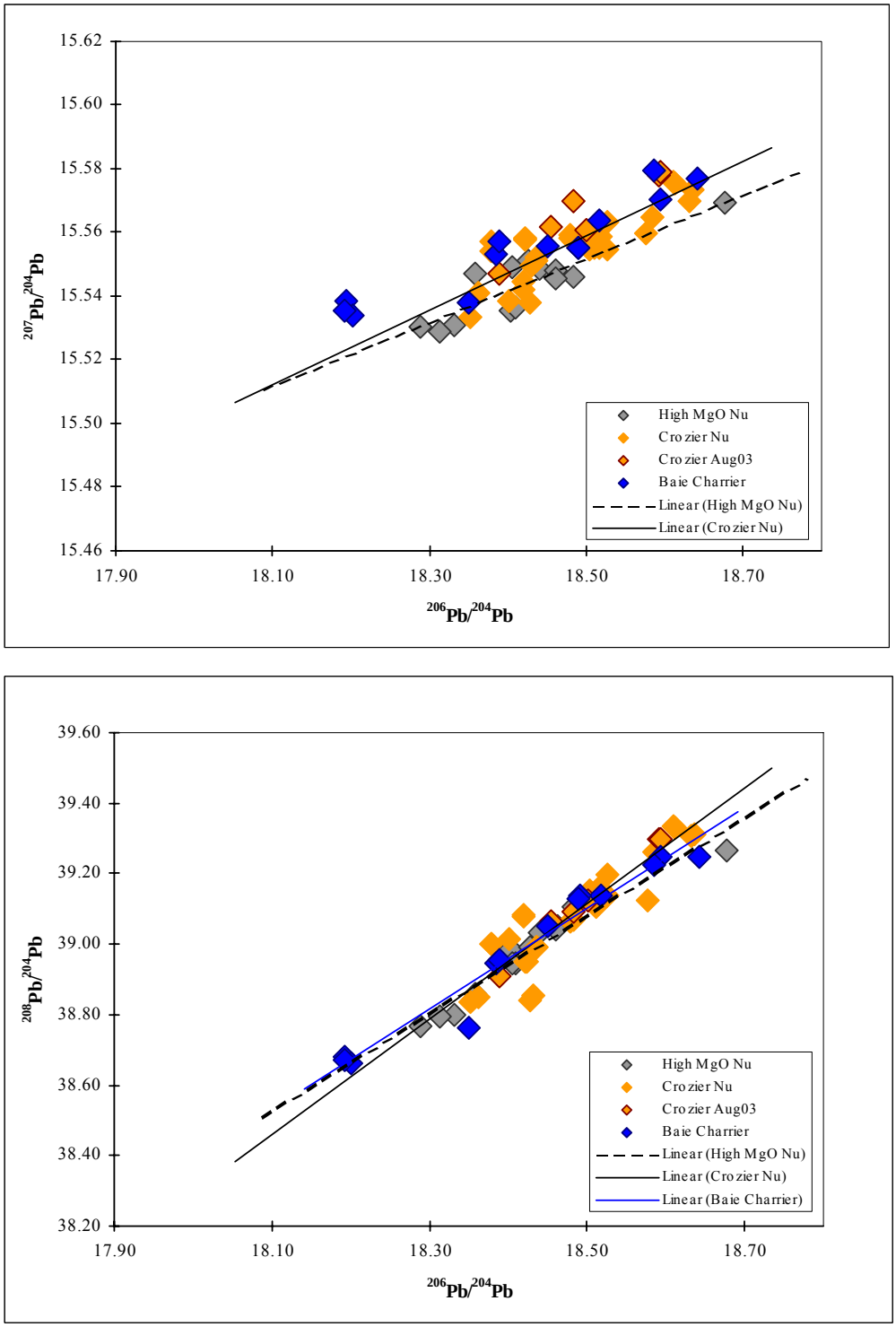

Fig. 5.8. Pb-Pb isotopic diagrams showing comparison between the Baie Charrier and Mt. Crozier sections. (a) $^{207}Pb/^{204}Pb$ vs. $^{206}Pb/^{204}Pb$. (b) $^{208}Pb/^{204}Pb$ vs. $^{206}Pb/^{204}Pb$. The $2\sigma_m$ is smaller than the symbol size.

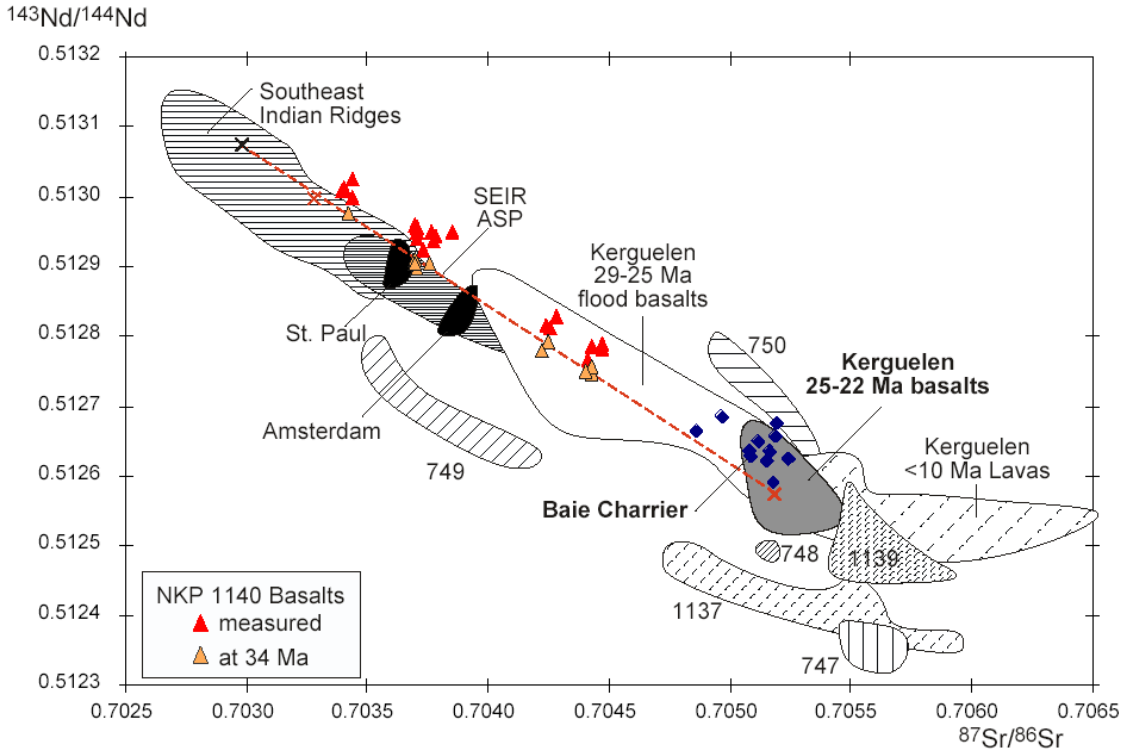

Fig. 5.9. Sr-Nd isotopic variations. This illustrates binary mixing between a depleted SEIR-type source and the Kerguelen plume. Baie Charrier falls within the enriched plume endmember, except for the three Unit C samples. (Weis and Frey, 2002)

with their eruption at 34 Ma, only 50 km away from the ridge axis (Weis & Frey, 2002). Mildly alkalic lavas from the Kerguelen Archipelago contain a strong signature of an enriched plume-derived component that originates from a deep mantle source (Weis *et al*., 2002). Basaltic lavas from the Kerguelen Archipelago also show an enrichment in radiogenic Pb relative to the SEIR. Since Baie Charrier has one of the most radiogenic Pb compositions of the Kerguelen Archipelago, the isotopic composition of the enriched Kerguelen mantle plume is well represented by the basaltic lava flows of the Baie Charrier section. The geochemical characteristics of the Baie Charrier basalts are entirely oceanic and present no evidence for any role of continental material in their genesis. This is consistent with what is observed in other basaltic sections on the archipelago (e.g.

Doucet *et al*., 2002; Frey *et al*., 2002; Weis *et al*., 2002) and in the Northern Kerguelen Plateau (Weis & Frey, 2002) and contrasts sharply with the Cenozoic history of the Kerguelen plume, where basalts were emplaced in a young ocean not too far from away from the old Gondwana continent (e.g. Ingle *et al*., 2003).

6.1 Conclusions

This study has presented new petrographic and geochemical data from the Baie Charrier basaltic section on the Courbet Peninsula of the Kerguelen Archipelago. Mineral chemistry, major and trace element concentrations, and Sr-Nd-Pb isotopic compositions of basalts from the section were integrated to provide a detailed geochemical analysis of the section. The major findings of this study are as follows:

1. Based on petrographic and geochemical characteristics, the Baie Charrier section can be subdivided into 4 distinct stratigraphic units. The variation observed between these units reflects temporal changes in volcanism related to the Kerguelen mantle plume. The small scale over which this variation occurs suggests considerable heterogeneity and relatively rapid temporal fluctuations in the source region.
2. Mineral-melt equilibria between olivine and clinopyroxene phenocrysts and basaltic melt reveal that a majority of the phenocrysts are in equilibrium with their host rocks. However, two samples (233 and 258) were interpreted to have inherited small amounts of xenocrystic olivines, and the highest MgO sample (240) was found to have accumulated both olivine and clinopyroxene. Therefore, the highest MgO lavas from the Baie Charrier section are constrained to between 8-10 wt.% MgO, consistent with findings from the Loranchet Peninsula basalts (Doucet *et al*., 2002). This suggests that 10 wt.% may be the maximum MgO content for Kerguelen Archipelago magmas without accumulated phenocrysts.
3. A comparison of the Baie Charrier and Mt. Crozier sections yields strikingly similar trace element and isotopic compositions, which is compelling evidence that both sections are derived from the same source region. Thus, this study provides evidence

to support the interpretation that the Courbet Peninsula is a single volcanic unit (Nougier, 1970). However, the petrography and MgO contents of the two sections are markedly different, with Baie Charrier possessing significantly higher MgO olivine-phyric basalts. The absence of olivine-phyric basalts at Mt. Crozier suggests that the eruptive center for these high flux magmas may not correspond to the present geographic center of the Courbet Peninsula.

4. The Baie Charrier basalts, consistent with other mildly alkalic lavas from the Kerguelen Archipelago, contain a strong signature of an enriched plume-derived component that likely originates deep in the mantle. The Baie Charrier basalts were found to have some of the most radiogenic Pb isotopic compositions on the Kerguelen Archipelago, together with Mt. Crozier. Therefore, the basaltic lava flows of the Baie Charrier section provide additional constraints on the source composition of the Kerguelen mantle plume.

REFERENCES

Albarede, F. & van der Hilst, R.D. (1999). New mantle convection model may reconcile conflicting evidence. *EOS Transactions, American Geophysical Union* **80**, 535-539.

Antretter, M., Steinberger, B., Heider, F. & Soffel, H. (2002). Paleolatitudes of the Kerguelen hotspot: new paleomagnetic results and dynamic modelling. *Earth and Planetary Science Letters* **203**, 635-650.

Baker, M.B., Alves, S. & Stolper, E.M. (1996). Petrography and petrology of the Hawaii Scientific Drilling Project lavas: inferences from olivine phenocryst abundances and compositions. *Journal of Geophysical Research* **101**, 11715-11727.

Charvis, P., Recq, M., Operto, S. & Brefort, D. (1995). Deep structure of the northern Kerguelen Plateau and hotspot-related activity. *Geophysical Journal International* **122**, 899-924.

Cheatham, M.M. (1996, January 21). *Sample purification for Sr and Nd isotopes.* Retrieved March 10, 2004, from http://www.geochemistry.syr.edu/cheatham/Techniques/TIMSsepSr%26Nd.html

Coffin, M.F., & Eldholm, O. (1994). Large igneous provinces: crustal structure, dimensions, and external consequences. *Reviews of Geophysics* **32**, 1-36.

Coffin, M.F., Pringle, M.S., Duncan, R.A., Gladczenko, T.P., Storey, M., Muller, R.D. & Gahagan, L.A. (2002). Kerguelen hotspot magma output since 130 Ma. *Journal of Petrology* **43**, 1121-1139.

Damasceno, D., Scoates, J.S., Weis, D., Frey, F.A. & Giret, A. (2002). Mineral chemistry of mildly alkalic basalts from the 25 Ma Mont Crozier Section, Kerguelen Archipelago: constraints on phenocryst crystallization environments. *Journal of Petrology* **43**, 1389-1413.

DePaolo, D.J., Bryce, J.G., Dodson, A., Shuster, D.L. & Kennedy, B.M. (2001). Isotopic evolution of Mauna Loa and the chemical structure of the Hawaiian plume. *Geochemistry, Geophysics, Geosystems* **2**, 2000GC000139.

Doucet, S., Weis, D., Scoates, J.S., Nicolayson, K., Frey, F.A. & Giret, A. (2002). The depleted mantle component in Kerguelen Archipelago basalts: petrogenesis of tholeiitic-transitional basalts from the Loranchet Peninsula. *Journal of Petrology* **43**, 1341-1366.

Duncan, R.A. (1991). Age distribution of volcanism along aseismic ridges in the eastern Indian Ocean. In: Weissel, J., Peirce, J., Taylor, E., Alt, J., *et al*. (eds) *Proceedings of the Ocean Drilling Program, Scientific Results, 121*. College Station, TX: Ocean Drilling Program, pp. 507-517.

Duncan, R.A. (2002). A time frame for construction of the Kerguelen Plateau and Broken Ridge. *Journal of Petrology* **43**, 1109-1119.

Duncan, R.A. & Storey, M. (1992). The life cycle of Indian Ocean hot spots. In: Duncan, R.A., Rea, R.A., Kidd, R.B., von Rad, U. & Weissel, J.K. (eds) *Synthesis of Results from Scientific Drilling in the Indian Ocean. Geophysical Monograph, America Geophysical Union* **70**, 91-103.

Frey, F.A., Coffin, M.F., Wallace, P.J., Weis, D., Zhao, X., Wise, S.W. Jr., Wahnert, V., Teagle, D.A.H., Saccocia. P.J., Reusch, D.N., Pringle, M.S., Nicolaysen, K.E., Neal, C.R., Müller, R.D., Moore, C.L., Mahoney, J.J., Keszthelyi, L., Inokuchi, H., Duncan, R.A., Delius, H., Damuth, J.E., Damasceno, D., Coxall, H.K., Borre, M.K., Boehm, F., Barling, J., Arndt, N.T. & Antretter, M. (2000). Origin and evolution of a submarine large igneous province: the Kerguelen Plateau and Broken Ridge, southern Indian Ocean. *Earth and Planetary Science Letters* **176**, 73-89.

Frey, F.A., Nicolayson, K., Kubit, B.K., Weis, D. & Giret, A. (2002). Flood basalt from Mont Tourmente in the Central Kerguelen Archipelago: the change from transitional to alkalic basalt at ~25 Ma. *Journal of Petrology* **43**, 1367-1387.

Frey, F.A., Weis, D., Yang, H.-J., Leyrit, H. & Giret, A. (2000). Temporal geochemical trends in Kerguelen Archipelago basalts: evidence for decreasing magma supply from the Kerguelen plume. *Chemical Geology* **164**, 61-80.

Fitton, J.G., Saunders, A.D., Norry, M.J., Hardarson, B.S. & Taylor, R.N. (1997). Thermal and chemical structure of the Iceland plume. *Earth and Planetary Science Letters* **153**, 197-208.

Galer, S.J.G. & Abouchami, W. (1998). Practical application of lead triple spiking for correction of instrumental mass discrimination. *Mineralogical Magazine* **62a**, 491-492.

Garcia, M.O. (1996). Petrography and olivine and glass chemistry of lavas from the Hawaii Scientific Drilling Project. *Journal of Geophysical Research* **101**, 11701-11713.

Griffiths, R.W., & Campbell, I.H. (1990). Stirring and structure in mantle starting plumes. *Earth and Planetary Science Letters* **99**, 66-78.

Grove, T.L. & Bryan, W.B. (1983). Fractionation of pyroxene-phyric MORB at low pressure: an experimental study. *Contributions to Mineralogy and Petrology* **84**, 293-309.

Helmberger, D.V., Wen, L. & Ding, X. (1998). Seismic evidence that the source of the Iceland hotspot lies at the core + mantle boundary. *Nature* **396**, 251-255.

Hofmann, A.W. (1997). Mantle geochemistry: the message from oceanic volcanism. *Nature* **385**, 219-229.

Ingle S., Weis, D., Doucet, S. & Mattielli, N. (2003). Hf isotope constraints on mantle sources and shallow-level contaminants during Kerguelen hot spot activity since 120 Ma. *Geochemistry Geophysics Geosystems* **4**, 1068.

Kurz, M.D., W. J. Jenkins, *et al*. (1982). Helium isotopic systematics of oceanic islands and mantle heterogeneity. *Nature* **297**, 43-46.

McDonough, W.F. & Sun, S.-s. (1995). The composition of the Earth. *Chemical Geology* **120**, 223-253.

Murata, K.J. & Richter, D.H. (1966). The settling of olivine in Kilauean magma as shown by lavas of the 1959 eruption. *American Journal of Science* **264**, 194-203.

Mutter, J. & Cande, S. (1983). The early opening between Broken Ridge and Kerguelen Plateau. *Earth and Planetary Science Letters* **65**, 369-376.

Nicolayson, K., Frey, F.A., Hodges, K.V., Weis, D. & Giret, A. (2000). $^{40}Ar/^{39}Ar$ geochronology of flood basalts from the Kerguelen Archipelago, southern Indian Ocean: implications for Cenozoic eruption rates of the Kerguelen plume. *Earth and Planetary science Letters* **174**, 313-328.

Nougier, J. (1970). Carte géologique au 1/200 000 de l'archipel des Kerguelen. Paris: Institut Géographique National.

Recq, M., Le Roy, I., Charvis, P., Goslin, J. & Brefort, D. (1994). Structure profonde du mont Ross d'après la réfraction sismique (îles Kerguelen, océan Indien austral). *Canadian Journal of Earth Sciences* **31**, 1806-1821.

Rhodes, J.M. (1996). Geochemical stratigraphy of lava flow samples by the Hawaii Scientific Drilling Project. *Journal of Geophysical Research* **101**, 11729-11746.

Ritsema, J., van Heijst, H.J. & Woodhouse, J.H. (1999). Complex shear wave velocity structure imaged beneath Africa and Iceland. *Science* **286**, 1925-1928.

Roeder, P.L. & Emslie, R.F. (1970). Olivine-liquid equilibrium. *Contributions to Mineralogy and Petrology* **29**, 275-289.

Shen, Y., Solomon, S.C., Bjarnason, I.T. & Wolfe, C.J. (1998). Seismic evidence for a lower-mantle origin of the Iceland plume. *Nature* **395**, 62-65.

Smith, W.H.F. & Sandwell, D.T. (1997). Global seafloor topography from satellite altimetry and ship depth soundings. *Science* **277,** 1956-1962.

Steinberger, B. (2000). Plumes in a convecting mantle: models and observations for individual hotspots. *Journal of Geophysical Research* **105**, 11127-11152.

Toplis, M.J. & Carroll, M.R. (1995). An experimental study of the influence of oxygen fugacity on Fe-Ti oxide stability, phase relations, and mineral-melt equilibria in ferro-basaltic systems. *Journal of Petrology* **36**, 1137-1170.

Weis, D., Doucet, S., Giret, A., Scoates, J. & Frey, F. (2002). Géochimie des îles et du plateau de Kerguelen. *Geologues* **137**, 40-51.

Weis, D. & Frey, F.A. (1991). Isotope geochemistry of Ninetyeast Ridge basalts: Sr, Nd, and Pb evidence for the involvement of the Kerguelen hot spot. In: Weissel, J., Peirce, J., Taylor, E., Alt, J., *et al*. (eds) *Proceedings of the Ocean Drilling Program, Scientific Results*, 121. College Station, TX: Ocean Drilling Program, pp. 591-610.

Weis, D. & Frey, F.A. (2002). Submarine basalts of the Northern Kerguelen Plateau: interaction between the Kerguelen Plume and the Southeast Indian Ridge revealed at ODP site 1140. *Journal of Petrology* **43**, 1287-1309.

Weis, D., Frey, F.A., Giret, A. & Cantagrel, J.M. (1998). Geochemical characteristics of the youngest volcano (Mount Ross) in the Kerguelen Archipelago: inferences for magma flux and composition of the Kerguelen plume. *Journal of Petrology* **39**, 973-994.

Weis, D., Frey, F.A., Leyrit, H. & Gautier, I. (1993). Kerguelen Archipelago revisited: geochemical and isotopic study of the SE Province lavas. *Earth and Planetary Science Letters* **118**, 101-119.

Weis, D., Frey, F.A., Saunders, A.D., Gibson, I. & Leg 121 Shipboard Scientific Party (1991). Ninetyeast Ridge (Indian Ocean): a 5000 km record of a Dupal mantle plume. *Geology* **19**, 99-102.

Weis, D., Frey, F.A., Schlich, R., Schaming, M., Montigny, R., Damasceno, D., Mattielli, N., Nicolayson, K.E. & Scoates, J.S. (2002). Trace of the Kerguelen mantle plume: evidence from seamounts between the Kerguelen Archipelago and Heard Island, Indian Ocean. *Geochemistry, Geophysics, Geosystems* **3**, 2001GC000251.

Weis, D. & Giret, A. (1994). Kerguelen plutonic complexes: Sr, Nd, Pb isotopic study and inferences about their sources, ages and geodynamic setting. *Bulletin de la Société Géologique de France* **166**, 47-59.

Weis, D., White, W.M., Frey, F.A., Duncan, R.A., Dehn, J., Fisk, M., Ludden, J., Saunders, A. & Storey, M. (1992). The influence of mantle plumes in generation of Indian Ocean crust. *Synthesis of Results from Scientific Drilling in the Indian Ocean. Geophysical Monograph, American Geophysical Union* **70**, 57-89.

Yang, Y.J., Frey, F.A., Weis, D., Giret, A., Pyle, D. & Michon, G. (1998). Petrogenesis of flood basalts forming the Northern Kerguelen Archipelago: implications for the Kerguelen plume. *Journal of Petrology* **39**, 711-748.

Appendix A: Microprobe analyses of olivine grains from the Baie Charrier section

Elevation (m):	85	85	85	85	85	85	85	85	85	85	85
Sample:	MM94-238	MM94-238	MM94-238	MM94-238	MM94-238	MM94-238	MM94-238	MM94-238	MM94-238	MM94-238	MM94-238
Crystal:	1	1	1	2	2	2	3	3	3	4	4
Zone:	Rim	Mid	Core	Rim	Mid	Core	Rim	Mid	Core	Rim	Mid
Oxides (wt.%)											
SiO_2	38.10	38.98	39.30	36.79	38.17	39.25	38.81	39.39	39.18	37.82	39.14
Cr_2O_3	0.01	0.02	0.03	0.04	0.01	0.02	0.02	0.07	0.04	0.02	0.04
FeO	23.47	17.61	17.67	29.27	20.94	18.99	18.03	16.07	17.80	24.15	18.43
MnO	0.34	0.20	0.22	0.48	0.15	0.20	0.21	0.14	0.22	0.44	0.23
NiO	0.18	0.21	0.33	0.16	0.08	0.22	0.24	0.37	0.26	0.19	0.24
MgO	37.96	42.51	42.61	32.68	40.18	42.03	43.41	43.53	42.49	36.99	41.54
CaO	0.24	0.20	0.20	0.37	0.20	0.23	0.19	0.21	0.20	0.31	0.23
Total	100.28	99.73	100.36	99.80	99.73	100.93	100.91	99.78	100.18	99.92	99.85
Cations (p.f.u.)											
Si	0.995	0.995	0.997	0.995	0.990	0.996	0.982	0.998	0.996	0.996	1.002
Cr	0.000	0.000	0.001	0.001	0.000	0.000	0.000	0.001	0.001	0.000	0.001
Fe^{2+}	0.513	0.376	0.375	0.662	0.454	0.403	0.382	0.340	0.379	0.532	0.394
Mn	0.008	0.004	0.005	0.011	0.003	0.004	0.004	0.003	0.005	0.010	0.005
Ni	0.004	0.004	0.007	0.003	0.002	0.004	0.005	0.008	0.005	0.004	0.005
Mg	1.478	1.618	1.612	1.318	1.554	1.589	1.638	1.644	1.611	1.452	1.585
Ca	0.007	0.006	0.005	0.011	0.005	0.006	0.005	0.006	0.005	0.009	0.006
Total	3.004	3.003	3.002	3.001	3.009	3.003	3.017	3.000	3.001	3.002	2.998
End members (%)											
Fo	74.2	81.1	81.1	66.6	77.4	79.8	81.1	82.8	81.0	73.2	80.1
Fa	25.8	18.9	18.9	33.4	22.6	20.2	18.9	17.2	19.0	26.8	19.9

Appendix A: continued

Elevation (m):	85	100	100	100	100	100	100	100	100	100	100
Sample:	MM94-238	MM94-236	MM94-236	MM94-236	MM94-236	MM94-236	MM94-236	MM94-236	MM94-236	MM94-236	MM94-236
Crystal:	4	1	1	1	2	2	2	3	3	3	4
Zone:	Core	Rim	Mid	Core	Rim	Mid	Core	Rim	Mid	Core	Rim
Oxides (wt.%)											
SiO_2	39.25	38.85	39.22	39.57	38.96	39.64	39.34	38.62	39.60	39.11	39.14
Cr_2O_3	0.06	0.03	0.05	0.03	0.05	0.07	0.10	0.00	0.07	0.04	0.04
FeO	17.49	19.38	16.56	17.16	17.79	15.38	16.02	20.58	14.75	16.18	17.75
MnO	0.23	0.27	0.18	0.12	0.21	0.19	0.26	0.28	0.16	0.18	0.22
NiO	0.28	0.24	0.26	0.26	0.27	0.27	0.35	0.23	0.36	0.32	0.28
MgO	42.82	41.46	43.84	43.09	42.51	44.35	43.55	40.03	44.70	43.81	42.31
CaO	0.20	0.23	0.20	0.21	0.22	0.21	0.19	0.29	0.21	0.23	0.25
Total	100.33	100.47	100.29	100.46	100.01	100.10	99.80	100.03	99.84	99.88	99.98
Cations (p.f.u.)											
Si	0.995	0.993	0.991	1.000	0.993	0.997	0.997	0.997	0.997	0.992	0.997
Cr	0.001	0.001	0.001	0.001	0.001	0.001	0.002	0.000	0.001	0.001	0.001
Fe^{2+}	0.371	0.414	0.350	0.363	0.379	0.324	0.339	0.444	0.310	0.343	0.378
Mn	0.005	0.006	0.004	0.003	0.004	0.004	0.006	0.006	0.003	0.004	0.005
Ni	0.006	0.005	0.005	0.005	0.005	0.006	0.007	0.005	0.007	0.006	0.006
Mg	1.619	1.580	1.651	1.623	1.616	1.663	1.645	1.540	1.677	1.655	1.607
Ca	0.005	0.006	0.005	0.006	0.006	0.006	0.005	0.008	0.006	0.006	0.007
Total	3.002	3.006	3.008	3.000	3.005	3.001	3.000	3.001	3.002	3.008	3.001
End members (%)											
Fo	81.4	79.2	82.5	81.7	81.0	83.7	82.9	77.6	84.4	82.8	80.9
Fa	18.6	20.8	17.5	18.3	19.0	16.3	17.1	22.4	15.6	17.2	19.1

Appendix A: continued

Elevation (m):	100	100	135	135	135	135	135	135	135	135	135
Sample:	MM94-236	MM94-236	MM94-233	MM94-233	MM94-233	MM94-233	MM94-233	MM94-233	MM94-233	MM94-233	MM94-233
Crystal:	4	4	1	1	1	2	2	2	3	3	3
Zone:	Mid	Core	Rim	Mid	Core	Rim	Mid	Core	Rim	Mid	Core
Oxides (wt.%)											
SiO_2	39.32	38.77	37.12	39.47	39.53	38.27	39.30	39.02	38.19	39.46	39.68
Cr_2O_3	0.07	0.05	0.03	0.06	0.04	0.02	0.07	0.04	0.04	0.08	0.06
FeO	17.28	17.56	26.33	13.18	13.25	22.29	18.53	18.54	23.13	15.10	15.10
MnO	0.16	0.15	0.42	0.14	0.14	0.29	0.17	0.24	0.28	0.16	0.19
NiO	0.25	0.34	0.10	0.38	0.45	0.12	0.27	0.26	0.26	0.32	0.30
MgO	42.74	42.38	34.95	45.51	45.60	38.34	41.48	40.65	37.69	44.03	44.29
CaO	0.21	0.19	0.22	0.20	0.18	0.27	0.21	0.24	0.19	0.21	0.20
Total	100.03	99.44	99.18	98.95	99.19	99.59	100.02	98.98	99.77	99.36	99.82
Cations (p.f.u.)											
Si	0.999	0.994	0.996	0.996	0.995	1.001	1.003	1.008	1.001	0.999	1.000
Cr	0.001	0.001	0.001	0.001	0.001	0.000	0.001	0.001	0.001	0.002	0.001
Fe^{2+}	0.367	0.376	0.590	0.278	0.279	0.487	0.396	0.400	0.507	0.320	0.318
Mn	0.003	0.003	0.010	0.003	0.003	0.006	0.004	0.005	0.006	0.003	0.004
Ni	0.005	0.007	0.002	0.008	0.009	0.002	0.006	0.005	0.005	0.006	0.006
Mg	1.618	1.619	1.397	1.711	1.712	1.494	1.579	1.565	1.472	1.662	1.664
Ca	0.006	0.005	0.006	0.005	0.005	0.008	0.006	0.007	0.005	0.006	0.005
Total	3.000	3.005	3.002	3.002	3.003	2.999	2.994	2.991	2.997	2.998	2.999
End members (%)											
Fo	81.5	81.1	70.3	86.0	86.0	75.4	80.0	79.6	74.4	83.9	83.9
Fa	18.5	18.9	29.7	14.0	14.0	24.6	20.0	20.4	25.6	16.1	16.1

Appendix A: continued

Elevation (m):	135	135	135	250	250	250	250	250	250	250	250
Sample:	MM94-233	MM94-233	MM94-233	MM94-258	MM94-258	MM94-258	MM94-258	MM94-258	MM94-258	MM94-258	MM94-258
Crystal:	4	4	4	1	1	1	2	2	2	3	3
Zone:	Rim	Mid	Core	Rim	Mid	Core	Rim	Mid	Core	Rim	Mid
Oxides (wt.%)											
SiO_2	38.05	39.61	39.08	35.90	37.36	37.14	32.58	38.03	37.92	37.00	37.04
Cr_2O_3	0.02	0.03	0.06	0.01	0.00	0.03	0.02	0.00	0.01	0.01	0.00
FeO	25.26	17.05	17.05	31.19	24.24	23.83	34.50	21.98	22.56	27.15	24.66
MnO	0.34	0.18	0.16	0.53	0.32	0.24	0.47	0.27	0.26	0.38	0.33
NiO	0.15	0.33	0.31	0.02	0.07	0.09	0.04	0.13	0.17	0.15	0.06
MgO	36.15	42.92	42.63	30.80	37.26	37.06	20.66	38.86	38.32	34.79	36.90
CaO	0.26	0.18	0.21	0.33	0.27	0.28	1.43	0.25	0.22	0.26	0.24
Total	100.22	100.30	99.49	98.78	99.52	98.67	89.70	99.51	99.46	99.74	99.22
Cations (p.f.u.)											
Si	1.002	1.002	0.998	0.993	0.988	0.989	1.027	0.994	0.994	0.991	0.986
Cr	0.000	0.001	0.001	0.000	0.000	0.001	0.001	0.000	0.000	0.000	0.000
Fe^{2+}	0.557	0.361	0.364	0.721	0.536	0.531	0.909	0.481	0.495	0.608	0.549
Mn	0.008	0.004	0.003	0.013	0.007	0.005	0.013	0.006	0.006	0.009	0.007
Ni	0.003	0.007	0.006	0.000	0.002	0.002	0.001	0.003	0.003	0.003	0.001
Mg	1.420	1.619	1.622	1.270	1.470	1.472	0.971	1.515	1.498	1.389	1.464
Ca	0.007	0.005	0.006	0.010	0.008	0.008	0.048	0.007	0.006	0.008	0.007
Total	2.997	2.997	3.000	3.006	3.011	3.008	2.969	3.005	3.002	3.007	3.014
End members (%)											
Fo	71.8	81.8	81.7	63.8	73.3	73.5	51.6	75.9	75.2	69.6	72.7
Fa	28.2	18.2	18.3	36.2	26.7	26.5	48.4	24.1	24.8	30.4	27.3

Appendix A: continued

Elevation (m):	250	250	250	250	250	250	250	275	275	275	275
Sample:	MM94-258	MM94-258	MM94-258	MM94-258	MM94-258	MM94-258	MM94-258	MM94-256	MM94-256	MM94-256	MM94-256
Crystal:	3	4	4	4	5	5	5	1	1	1	2
Zone:	Core	Rim	Mid	Core	Rim	Mid	Core	Rim	Mid	Core	Rim
Oxides (wt.%)											
SiO_2	37.56	36.33	37.50	37.41	34.73	37.55	37.66	35.99	39.01	39.84	36.74
Cr_2O_3	0.02	0.00	0.01	0.04	0.02	0.02	0.06	0.01	0.00	0.03	0.02
FeO	24.22	30.67	23.67	24.51	34.16	23.72	23.09	33.68	15.42	14.78	28.56
MnO	0.34	0.61	0.30	0.32	0.56	0.32	0.29	0.41	0.19	0.20	0.38
NiO	0.12	0.06	0.10	0.13	0.03	0.14	0.15	0.11	0.24	0.22	0.17
MgO	36.76	31.54	36.85	36.95	27.24	37.32	37.38	29.62	44.00	44.52	33.06
CaO	0.24	0.32	0.23	0.26	0.51	0.22	0.25	0.37	0.25	0.25	0.35
Total	99.26	99.51	98.66	99.63	97.25	99.31	98.88	100.19	99.11	99.83	99.28
Cations (p.f.u.)											
Si	0.996	0.993	0.997	0.990	0.994	0.993	0.997	0.992	0.993	1.002	0.996
Cr	0.001	0.000	0.000	0.001	0.001	0.000	0.001	0.000	0.000	0.001	0.001
Fe^{2+}	0.537	0.701	0.526	0.542	0.818	0.525	0.511	0.776	0.328	0.311	0.647
Mn	0.008	0.014	0.007	0.007	0.014	0.007	0.006	0.010	0.004	0.004	0.009
Ni	0.003	0.001	0.002	0.003	0.001	0.003	0.003	0.003	0.005	0.004	0.004
Mg	1.452	1.285	1.461	1.457	1.162	1.471	1.475	1.216	1.670	1.668	1.336
Ca	0.007	0.009	0.007	0.007	0.016	0.006	0.007	0.011	0.007	0.007	0.010
Total	3.002	3.004	3.000	3.007	3.004	3.006	3.002	3.008	3.007	2.997	3.002
End members (%)											
Fo	73.0	64.7	73.5	72.9	58.7	73.7	74.3	61.1	83.6	84.3	67.4
Fa	27.0	35.3	26.5	27.1	41.3	26.3	25.7	38.9	16.4	15.7	32.6

Appendix A: continued

Elevation (m):	275	275	275	275	275	275	275	275	290	290	290
Sample:	MM94-256	MM94-256	MM94-256	MM94-256	MM94-256	MM94-256	MM94-256	MM94-256	MM94-253	MM94-253	MM94-253
Crystal:	2	2	3	3	3	4	4	4	1	1	1
Zone:	Mid	Core	Rim	Mid	Core	Rim	Mid	Core	Rim	Mid	Core
Oxides (wt.%)											
SiO_2	38.54	38.59	35.59	38.69	38.70	35.35	39.25	38.96	37.86	38.81	39.34
Cr_2O_3	0.00	0.04	0.03	0.06	0.02	0.02	0.00	0.08	0.02	0.00	0.06
FeO	19.22	17.67	35.86	17.68	17.81	34.04	15.54	15.79	24.87	17.51	15.68
MnO	0.20	0.28	0.47	0.20	0.25	0.49	0.21	0.23	0.34	0.30	0.18
NiO	0.23	0.25	0.03	0.20	0.20	0.15	0.30	0.23	0.11	0.24	0.30
MgO	41.62	42.18	27.24	42.26	42.31	28.71	44.18	43.92	36.10	42.66	43.58
CaO	0.13	0.18	0.37	0.26	0.30	0.42	0.26	0.28	0.34	0.27	0.25
Total	99.94	99.18	99.60	99.34	99.58	99.18	99.74	99.50	99.63	99.79	99.40
Cations (p.f.u.)											
Si	0.990	0.992	0.998	0.993	0.991	0.988	0.993	0.990	1.002	0.991	0.999
Cr	0.000	0.001	0.001	0.001	0.000	0.000	0.000	0.002	0.000	0.000	0.001
Fe^{2+}	0.413	0.380	0.841	0.379	0.381	0.796	0.329	0.335	0.551	0.374	0.333
Mn	0.004	0.006	0.011	0.004	0.005	0.012	0.004	0.005	0.008	0.006	0.004
Ni	0.005	0.005	0.001	0.004	0.004	0.003	0.006	0.005	0.002	0.005	0.006
Mg	1.593	1.617	1.139	1.616	1.615	1.197	1.667	1.663	1.424	1.624	1.650
Ca	0.004	0.005	0.011	0.007	0.008	0.013	0.007	0.008	0.010	0.007	0.007
Total	3.008	3.006	3.001	3.005	3.006	3.009	3.007	3.008	2.997	3.009	3.000
End members (%)											
Fo	79.4	81.0	57.5	81.0	80.9	60.1	83.5	83.2	72.1	81.3	83.2
Fa	20.6	19.0	42.5	19.0	19.1	39.9	16.5	16.8	27.9	18.7	16.8

Appendix A: continued

Elevation (m):	290	290	290	290	290	290	290	290	290	290	290
Sample:	MM94-253	MM94-253	MM94-253	MM94-253	MM94-253	MM94-253	MM94-253	MM94-253	MM94-253	MM94-253	MM94-253
Crystal:	2	2	2	3	3	3	4	4	4	5	5
Zone:	Rim	Mid	Core	Rim	Mid	Core	Rim	Mid	Core	Rim	Mid
Oxides (wt.%)											
SiO_2	37.74	39.39	39.04	38.07	38.57	38.61	38.32	39.03	39.08	36.01	38.77
Cr_2O_3	0.03	0.05	0.06	0.03	0.04	0.02	0.04	0.06	0.01	0.00	0.03
FeO	21.44	14.99	15.89	21.03	17.86	19.01	19.45	16.33	17.15	32.07	17.23
MnO	0.21	0.24	0.17	0.28	0.19	0.27	0.22	0.25	0.20	0.36	0.21
NiO	0.21	0.30	0.27	0.19	0.21	0.22	0.18	0.17	0.22	0.10	0.21
MgO	40.16	44.64	43.78	39.39	42.23	41.28	41.09	43.49	42.92	30.31	42.70
CaO	0.28	0.28	0.29	0.30	0.19	0.16	0.29	0.25	0.27	0.34	0.20
Total	100.06	99.89	99.50	99.29	99.29	99.57	99.59	99.58	99.85	99.19	99.36
Cations (p.f.u.)											
Si	0.980	0.993	0.992	0.994	0.991	0.994	0.990	0.992	0.994	0.995	0.993
Cr	0.001	0.001	0.001	0.001	0.001	0.000	0.001	0.001	0.000	0.000	0.001
Fe^{2+}	0.466	0.316	0.338	0.459	0.384	0.409	0.420	0.347	0.365	0.741	0.369
Mn	0.005	0.005	0.004	0.006	0.004	0.006	0.005	0.005	0.004	0.008	0.004
Ni	0.004	0.006	0.006	0.004	0.004	0.005	0.004	0.004	0.004	0.002	0.004
Mg	1.555	1.677	1.658	1.533	1.618	1.584	1.582	1.649	1.628	1.248	1.630
Ca	0.008	0.008	0.008	0.008	0.005	0.004	0.008	0.007	0.007	0.010	0.006
Total	3.018	3.006	3.007	3.005	3.008	3.003	3.009	3.005	3.004	3.004	3.006
End members (%)											
Fo	76.9	84.1	83.1	77.0	80.8	79.5	79.0	82.6	81.7	62.7	81.5
Fa	23.1	15.9	16.9	23.0	19.2	20.5	21.0	17.4	18.3	37.3	18.5

Appendix A: continued

Elevation (m):	290	290	290	290	375	375	375	375	375	375	375
Sample:	MM94-253	MM94-253	MM94-253	MM94-253	MM94-242	MM94-242	MM94-242	MM94-242	MM94-242	MM94-242	MM94-242
Crystal:	5	6	6	6	2	2	2	4	4	4	5
Zone:	Core	Rim	Mid	Core	Rim	Mid	Core	Rim	Mid	Core	Rim
Oxides (wt.%)											
SiO_2	38.89	37.13	38.51	38.45	37.04	38.09	38.28	36.39	38.42	38.32	36.77
Cr_2O_3	0.00	0.00	0.02	0.00	0.00	0.00	0.02	0.00	0.05	0.03	0.02
FeO	17.84	23.79	18.09	19.37	25.64	20.97	20.56	28.90	18.82	18.71	29.15
MnO	0.28	0.31	0.25	0.23	0.35	0.28	0.26	0.42	0.23	0.24	0.38
NiO	0.19	0.12	0.22	0.18	0.08	0.14	0.15	0.14	0.22	0.17	0.03
MgO	42.17	37.22	42.20	41.10	35.75	39.82	40.04	33.08	41.66	41.32	32.53
CaO	0.20	0.36	0.19	0.19	0.29	0.28	0.24	0.30	0.25	0.25	0.32
Total	99.57	98.93	99.47	99.51	99.15	99.58	99.55	99.22	99.64	99.02	99.22
Cations (p.f.u.)											
Si	0.996	0.987	0.989	0.992	0.991	0.990	0.994	0.990	0.989	0.992	0.999
Cr	0.000	0.000	0.000	0.000	0.000	0.000	0.000	0.000	0.001	0.001	0.000
Fe^{2+}	0.382	0.529	0.389	0.418	0.574	0.456	0.446	0.657	0.405	0.405	0.663
Mn	0.006	0.007	0.005	0.005	0.008	0.006	0.006	0.010	0.005	0.005	0.009
Ni	0.004	0.002	0.004	0.004	0.002	0.003	0.003	0.003	0.005	0.004	0.001
Mg	1.610	1.475	1.616	1.581	1.426	1.544	1.549	1.341	1.599	1.594	1.318
Ca	0.005	0.010	0.005	0.005	0.008	0.008	0.007	0.009	0.007	0.007	0.009
Total	3.003	3.011	3.010	3.006	3.008	3.007	3.005	3.009	3.010	3.007	2.999
End members (%)											
Fo	80.8	73.6	80.6	79.1	71.3	77.2	77.6	67.1	79.8	79.7	66.5
Fa	19.2	26.4	19.4	20.9	28.7	22.8	22.4	32.9	20.2	20.3	33.5

Appendix A: continued

Elevation (m):	375	375	410	410	410	410	410	410	410	410	410
Sample:	MM94-242	MM94-242	MM94-240	MM94-240	MM94-240	MM94-240	MM94-240	MM94-240	MM94-240	MM94-240	MM94-240
Crystal:	5	5	1	1	1	3	3	3	5	5	5
Zone:	Mid	Core	Rim	Mid	Core	Rim	Mid	Core	Rim	Mid	Core
Oxides (wt.%)											
SiO_2	36.84	37.04	38.72	39.27	39.29	35.29	39.04	38.60	38.80	38.54	38.02
Cr_2O_3	0.01	0.02	0.04	0.00	0.01	0.07	0.00	0.02	0.02	0.01	0.00
FeO	26.86	26.64	18.32	16.50	16.72	28.23	17.81	17.84	19.16	21.33	21.34
MnO	0.37	0.29	0.23	0.20	0.21	0.54	0.22	0.24	0.31	0.26	0.31
NiO	0.09	0.09	0.28	0.21	0.21	0.09	0.18	0.16	0.19	0.14	0.16
MgO	34.81	34.97	41.82	43.15	43.26	27.77	42.09	42.11	41.22	39.90	39.58
CaO	0.34	0.34	0.27	0.27	0.27	0.50	0.22	0.23	0.29	0.21	0.25
Total	99.32	99.40	99.67	99.60	99.97	92.49	99.56	99.19	100.00	100.40	99.65
Cations (p.f.u.)											
Si	0.990	0.993	0.994	0.999	0.996	1.032	0.999	0.993	0.996	0.994	0.990
Cr	0.000	0.001	0.001	0.000	0.000	0.002	0.000	0.000	0.000	0.000	0.000
Fe^{2+}	0.604	0.597	0.393	0.351	0.355	0.690	0.381	0.384	0.411	0.460	0.465
Mn	0.008	0.007	0.005	0.004	0.005	0.013	0.005	0.005	0.007	0.006	0.007
Ni	0.002	0.002	0.006	0.004	0.004	0.002	0.004	0.003	0.004	0.003	0.003
Mg	1.394	1.397	1.600	1.636	1.635	1.210	1.606	1.614	1.577	1.535	1.537
Ca	0.010	0.010	0.007	0.007	0.007	0.016	0.006	0.006	0.008	0.006	0.007
Total	3.008	3.006	3.005	3.001	3.002	2.964	3.001	3.006	3.003	3.004	3.009
End members (%)											
Fo	69.8	70.1	80.3	82.3	82.2	63.7	80.8	80.8	79.3	76.9	76.8
Fa	30.2	29.9	19.7	17.7	17.8	36.3	19.2	19.2	20.7	23.1	23.2

Appendix A: continued

Elevation (m):	410	410	410
Sample:	MM94-240	MM94-240	MM94-240
Crystal:	6	6	6
Zone:	Rim	Mid	Core
Oxides (wt.%)			
SiO_2	37.67	39.77	39.79
Cr_2O_3	0.05	0.01	0.04
FeO	24.53	14.39	14.48
MnO	0.34	0.23	0.23
NiO	0.16	0.21	0.26
MgO	35.99	45.05	45.06
CaO	0.38	0.29	0.27
Total	99.13	99.94	100.13
Cations (p.f.u.)			
Si	1.002	0.998	0.997
Cr	0.001	0.000	0.001
Fe^{2+}	0.545	0.302	0.303
Mn	0.008	0.005	0.005
Ni	0.003	0.004	0.005
Mg	1.426	1.685	1.683
Ca	0.011	0.008	0.007
Total	2.997	3.001	3.002
End members (%)			
Fo	72.3	84.8	84.7
Fa	27.7	15.2	15.3

Appendix B: Microprobe analyses of clinopyroxene grains from the Baie Charrier section

Elevation (m):	375	375	375	375	375	375	375	375	375	410	410
Sample:	MM94-242	MM94-242	MM94-242	MM94-242	MM94-242	MM94-242	MM94-242	MM94-242	MM94-242	MM94-240	MM94-240
Crystal:	1	1	1	3	3	3	6	6	6	2	2
Zone:	Rim	Mid	Core	Rim	Mid	Core	Rim	Mid	Core	Rim	Mid
Oxides (wt.%)											
SiO_2	50.02	50.46	51.00	49.65	50.40	50.89	49.55	49.85	50.18	50.12	50.52
TiO_2	1.47	1.21	1.03	1.44	1.13	1.16	1.56	1.42	1.06	0.96	0.64
Al_2O_3	3.32	2.66	2.27	2.11	2.54	2.69	3.10	3.33	2.77	3.68	4.43
Cr_2O_3	0.31	0.32	0.28	0.04	0.25	0.27	0.19	0.40	0.41	0.37	0.64
FeO	8.44	8.70	8.62	10.97	8.53	8.06	9.36	8.02	7.80	6.29	5.81
MnO	0.19	0.16	0.18	0.24	0.21	0.15	0.15	0.21	0.21	0.17	0.17
MgO	14.55	15.53	15.83	14.13	15.40	15.30	14.40	15.14	15.63	15.97	16.98
CaO	20.38	19.50	19.43	19.67	19.88	20.39	20.45	20.45	20.16	21.02	19.07
Na_2O	0.33	0.30	0.30	0.31	0.31	0.33	0.31	0.33	0.29	0.25	0.41
Total	99.00	98.84	98.94	98.55	98.65	99.25	99.08	99.16	98.50	98.83	98.67
Cations (p.f.u.)											
Si	1.881	1.897	1.913	1.897	1.900	1.903	1.872	1.870	1.891	1.872	1.874
Ti	0.042	0.034	0.029	0.041	0.032	0.033	0.044	0.040	0.030	0.027	0.018
Al	0.147	0.118	0.100	0.095	0.113	0.118	0.138	0.147	0.123	0.162	0.194
Cr	0.009	0.010	0.008	0.001	0.007	0.008	0.006	0.012	0.012	0.011	0.019
Fe^{2+}	0.243	0.242	0.241	0.308	0.230	0.226	0.250	0.208	0.202	0.150	0.147
Fe^{3+}	0.022	0.032	0.029	0.043	0.038	0.026	0.046	0.044	0.044	0.047	0.033
Mn	0.006	0.005	0.006	0.008	0.007	0.005	0.005	0.007	0.007	0.005	0.005
Mg	0.816	0.871	0.886	0.805	0.865	0.853	0.811	0.847	0.878	0.890	0.939
Ca	0.821	0.786	0.781	0.805	0.803	0.817	0.828	0.822	0.814	0.841	0.758
Na	0.024	0.022	0.022	0.023	0.023	0.024	0.023	0.024	0.021	0.018	0.029
Total	4.011	4.016	4.015	4.025	4.019	4.013	4.023	4.022	4.022	4.023	4.017
AlIV	0.119	0.103	0.087	0.103	0.100	0.097	0.128	0.130	0.109	0.128	0.126
AlVI	0.028	0.015	0.013	0.000	0.013	0.021	0.010	0.018	0.014	0.034	0.068
Mg#	0.77	0.78	0.79	0.72	0.79	0.79	0.76	0.80	0.81	0.86	0.86
$Fe^{2+}/(Fe^{2+}+Fe^{3+})$	0.92	0.88	0.89	0.88	0.86	0.90	0.85	0.83	0.82	0.76	0.82
End members (%)											
Wo	43.7	41.4	40.9	42.0	42.3	43.1	43.8	43.8	43.0	44.7	41.1
En	43.4	45.9	46.4	42.0	45.6	45.0	42.9	45.1	46.4	47.3	50.9
Fs	12.9	12.7	12.6	16.1	12.1	11.9	13.2	11.1	10.7	8.0	8.0

Appendix B: continued

Elevation (m):	410	410	410	410
Sample:	MM94-240	MM94-240	MM94-240	MM94-240
Crystal:	2	4	4	4
Zone:	Core	Rim	Mid	Core
Oxides (wt.%)				
SiO_2	51.25	48.72	48.01	48.40
TiO_2	0.53	1.05	1.14	1.13
Al_2O_3	3.65	6.42	6.42	6.30
Cr_2O_3	0.63	0.53	0.58	0.55
FeO	5.28	6.83	6.96	6.92
MnO	0.09	0.10	0.17	0.17
MgO	17.47	14.87	14.85	14.99
CaO	19.37	19.62	19.83	19.85
Na_2O	0.38	0.49	0.45	0.48
Total	98.66	98.63	98.41	98.78
Cations (p.f.u.)				
Si	1.896	1.822	1.805	1.812
Ti	0.015	0.030	0.032	0.032
Al	0.159	0.283	0.285	0.278
Cr	0.018	0.016	0.017	0.016
Fe^{2+}	0.136	0.179	0.164	0.162
Fe^{3+}	0.028	0.034	0.055	0.054
Mn	0.003	0.003	0.005	0.005
Mg	0.964	0.829	0.832	0.837
Ca	0.768	0.786	0.799	0.796
Na	0.027	0.035	0.033	0.035
Total	4.014	4.017	4.028	4.027
AlIV	0.104	0.178	0.195	0.188
AlVI	0.056	0.105	0.090	0.090
Mg#	0.88	0.82	0.84	0.84
$Fe^{2+}/(Fe^{2+}+Fe^{3+})$	0.83	0.84	0.75	0.75
End members (%)				
En	41.1	43.8	44.5	44.3
Fs	51.6	46.2	46.4	46.6
Wo	7.3	10.0	9.1	9.1

DH-230

DH-233

DH-236

DH-238

DH-240

DH-242

DH-244

DH-253

DH-256

DH-258